Optimization and analysis of UAV fuselage for medical deliveries

Dilki Dias Somanatha Arachchige

Master Dissertation

Supervisors:
Prof. Volnei Tita
Prof. Carolina Silva
Prof. A. Pedro Aguiar

Masters in mechanical engineering

Faculty of Engineering, University of Porto

Porto, June 2023

Abstract

This thesis focuses on the development of a fixed-wing UAV for medical item delivery, accompanied by the creation of a custom computational tool for optimizing composite structures. The objective was to develop a fixed-wing UAV with the specific requirements of medical deliveries while implementing the developed optimization tool for the further efficiency. This thesis presents the successful development of the first aircraft prototype, encompassing various stages such as sizing, design, aerodynamics, structural analysis, and manufacturing. Flight tests were conducted, providing valuable data to validate the methodologies used in sizing and manufacturing. After a first prototype, a second UAV tailored specifically for medical item delivery was developed, considering the design requirements and optimization constraints. This phase involved refining the design based on the insights gained from the initial prototype, resulting in the successful creation of a UAV that meets the specific requirements. Recognizing the significance of optimizing the structure of the medical UAV, a custom computational tool was developed. This tool employed the Genetic Algorithm (GA) and a surrogate model, incorporating Abaqus finite element software to obtain the failure index. Design of Experiments (DoE) with the Latin Hyper Cubic method was employed to sample data, generating a surrogate model through simulations in Abaqus. The Gaussian regression method was selected as the most suitable choice for generating the surrogate model. The algorithm was validated through set of load case analysis. The developed optimization algorithm facilitates the selection of the optimal combination of layers and ply orientations for the UAV's composite structure with custom defined design and manufacturing constraints.

Acknowledgements

First and foremost, I extend my sincere thanks to Prof. Dr. Volnei Tita for his invaluable guidance, support, and expert knowledge throughout this and the UAV projects. His mentorship and encouragement not only in the thesis work but also in the academic classes have been extremely assisting.

I am deeply grateful to Prof. Carolina Silva and Federico Danzi for their valuable contributions and insights. Their expertise and willingness to share their knowledge have greatly enriched this thesis. I am fortunate to have had the opportunity to learn from them and incorporate their perspectives into this work. Especially grateful for always been there available whenever assistance is needed.

Special thanks to Prof. Pedro Aguiar and the SYSTEC Lab, where the whole Medical UAV was designed and manufactured, among many other UAV projects. Especial thanks for all the positive feedback and encouragement throughout the work.

I would like to extend my appreciation to Anuj Regmi for letting me partake in the UAV project, where I acquire invaluable knowledge and experience. Additionally, the medical drone project in the SYSTEC Lab which was extended in this thesis.

I extend my heartfelt gratitude to my colleague and partner in the UAV project, Douglas Rodriguez. His hard work, dedication, and remarkable ideas have been invaluable to the success of this project. Without his collaboration and contribution in all aspects, completing this project successfully would have been impossible. I am truly grateful for his support and partnership throughout the journey.

Special acknowledgment for Prof. Pedro Gamboa and colleagues from University of Beira Interior for assisting with expert knowledge, manufacturing process and the flight testing.

Finally, I am grateful to my mother and father for all the unwavering support throughout every aspect of my life. I am also thankful to my brother and sister for always being there to cheer me on and all the support.

This work was financially supported by: Base (UIDB/00147/2020) and Programmatic (UIDP/00147/2020) funding of the SYSTEC – Center for Systems and Technologies; ARISE - Associate Laboratory Advanced Production and Intelligent Systems (LA/P/0112/2020), both funded by national funds through the FCT/MCTES (PIDDAC); DynamiCITY: Fostering Dynamic Adaptation of Smart Cities to Cope with Crises and Disruptions (NORTE-01-0145-FEDER-000073), supported by Norte Portugal Regional Operational Programme (NORTE 2020), under the PORTUGAL 2020 Partnership Agreement, through the European Regional Development Fund (ERDF) and RELIABLE - Advances in Control Design Methodologies for Safety Critical Systems Applied to Robotics (PTDC/EEI-AUT/3522/2020), funded by national funds (PIDDAC) through FCT/MCTES.

Contents

Figures

Tables

Abbreviations

AoA – Angle of Attack

ACO – Ant Colony Optimization

AFP – Automated Fibre Placement

CAD – Computer Aided Design

CAE – Computer Aided Engineering

CFD – Computational Fluid Dynamics

CG – Centre of Gravity

CLT – Classical Laminate Theory

Deg – Degrees

DoE – Design of Experiments

EASA – European Union Aviation Safety Agency

ESC – Electronic Speed Controller

FEA – Finite Element Analysis

FEM – Finite Element Model

GA – Genetic Algorithm

LHS – Latin Hypercubic sampling

LLT – Lifting Line Theory

NHS – National Health Service

NSGA - Non-dominated Sorting Genetic Algorithm

PPE – Personal Protective Equipment

PR – Power Required

PSO – Particle Swarm Optimization

RBF – Radial Basis Functions

SA – Simulated Annealing

SPEA – Strength Pareto Evolutionary Algorithm

SVR – Support Vector Regression

TSAIH – Tsai Hill failure index

UAV – Unmanned Aerial Vehicle

1 Introduction

1.1 Background

Composite materials in structural applications have gained significant attention in various industries including aerospace due to their distinctive properties such as high stiffness and strength-to-weight ratio, durability, corrosion resistance, fatigue properties and thermal properties [1]–[5]. The optimization of composite structures has become a vital research area to improve their structural performance while reducing manufacturing costs, which allows for harnessing its best efficiency.

The mechanical properties of composite structures are governed by parameters such as reinforcement type and volume fraction; matrix material; interfacial bonding; fibre orientation and alignment; manufacturing process and parameters; fibre length or particle size and distribution; and composite architecture. Hence, composite properties can be adapted as desired for the application. Moreover, the optimization methods for composite structures also should be suitable for the application and objective.

The optimization of composite structures can be achieved through various methods, including analytical, numerical, and metaheuristic techniques. Analytical methods are limited to simple geometries and loading conditions, while numerical methods, such as finite element analysis (FEA), require extensive computational resources and may not be suitable for large design spaces. Metaheuristic optimization algorithms, such as Genetic Algorithm (GA), have become popular due to their ability to handle complex design spaces and non-linear optimization problems.

1.2 Motivation

Unmanned Aerial Vehicles (UAV) or drones have increasingly been used in recent years for various applications. A few vital applications are to facilitate access in remote areas for medical item distribution, surveillance, wildfire detection and so on. While some of these applications are solely cost-effective and/or efficiently targeted, most of the applications such as medical item delivery, wildfire detection and wildlife surveillance are lifesaving situations. For instance, delivering emergency medical items such as blood packages, vaccines, organs and medications in rural areas with dangerous terrain is impossible in some areas of the world. This can be due to the underdeveloped infrastructure, terrain features or harsh climates which limit the fast ground access as well as manned air access. Leaving the UAV being a cost-effective and efficient way to reach those areas safely and faster.

In order to facilitate access to rural areas, autonomous UAVs can be used. SYSTEC Lab of the University of Porto is developing a variety of UAVs and autonomous control systems to use for medical delivery and surveillance. One of the projects was the development of a medical delivery UAV to fly into rural areas of Nepal to deliver blood packages, where, due to the harsh climate and terrain conditions, immediate access to some medical facilities is limited.

In the case of fixed-wing delivery UAVs, it is very important to optimize the structure, which will result in reducing the total weight without losing the structural integrity. With the reduced total weight, it is possible to increase the range and endurance of the aircraft which allows it to deliver for further regions or to increase the payload capacity the UAV.

The existing optimization tools integrated with finite element software provide less control over the optimization parameters such as design constraints and manufacturing preferences.

1.3 Objectives

This thesis focuses on the development of a computational tool to optimize composite structures using a Genetic Algorithm (GA) and a surrogate model. The tool is specifically applied to optimize the design of a carbon composite fuselage structure for a UAV used in medical delivery. The objective is to improve the structural performance, reduce manufacturing costs, and decrease the total weight of the UAV. The study aims to provide insights into the application of GA for optimizing composite structures, including the selection of input parameters and fitness functions. A key aspect of the research is exploring the use of a surrogate model, generated through chosen regression methods, instead of relying solely on a finite element model for optimization. The scope of the study also includes evaluating the structural performance of the optimized designs using finite element analysis (FEA).

Additionally, this thesis encompasses the complete design and manufacture of an electrically powered fixed-wing UAV, specifically designed for medical delivery in Nepal. The majority of the UAV's structure is made of carbon and Kevlar composites. The design process includes sizing the aircraft, selecting the power plant, conducting aerodynamic and stability analyses, detailed design, structural analysis, manufacturing, assembly, and testing. To validate the sizing methods, performance estimations, manufacturing processes, autopilot, and avionics, a lightweight first aircraft prototype is developed prior to the main UAV design. The prototype undergoes development, manufacturing, and testing in accordance with the defined requirements.

Overall, this thesis presents a comprehensive approach involving the development of an optimization tool for composite structures, its application to the design of a medical delivery UAV fuselage, and the validation through the development of a lightweight prototype. The research contributes to the advancement of UAV technology in the field of medical delivery and highlights the potential of using GA and surrogate models for optimizing composite structures.

1.4 Thesis outline

According to the above described objectives, this thesis is divided into 3 main parts as design and manufacturing of the First Aircraft prototype, the design of the medical UAV (Second Aircraft) and the development of the composite optimization algorithm.

The 2nd chapter of this thesis presents a state of art and literature review of the carbon composite materials, optimization of carbon structures, development of surrogate models, Genetic algorithm, UAVs for medical delivery and UAV sizing.

The design, manufacturing and testing of the first aircraft prototype are explained in the 3rd chapter, together with the proposed changes to the next version.

In the 4th chapter, the sizing and design of the medical UAV consider the results from the prototype test flight results.

The 5th chapter presents the methodology for developing the optimization algorithm for composite structures.

The 6th chapter validates the developed algorithm with test cases.

The 7th chapter includes the structural optimization of the composite fuselage using the developed algorithm.

The discussion and conclusion of the work are presented in the 8th chapter.

2 State of art and literature review

2.1 Composites materials

The use of composite materials in the aviation industry has been increasing in recent years due to their high strength-to-weight ratio, corrosion resistance, and durability. The use of composites in aircraft design has resulted in significant improvements in structural performance, reduced weight, and increased fuel efficiency.

In addition to weight reduction, the use of composites in small aircraft has also resulted in improved durability and corrosion resistance. Small aircraft are often exposed to harsh environmental conditions, and composites offer superior resistance to corrosion compared to traditional metal structures. For example, Al-Sammarraie et al. [6] investigated the corrosion behaviour of composite materials in small aircraft and found that the composites showed superior corrosion resistance compared to traditional metal structures.

Several studies have investigated the application of composites in small aircraft structures. For example, Voge et al. [7] investigated the use of composites in the design of a small, two-seat aircraft and found that the use of composites resulted in a weight reduction of 30% compared to a traditional aluminium design. The study also found that the use of composites improved the aircraft's performance, including increased range and improved handling characteristics.

The manufacturing processes of composites have also been investigated in the context of small aircraft. Small aircraft manufacturing typically involves low-volume production, which makes composites an attractive option due to their ability to be moulded into complex shapes. For example, Zhang et al. [8] investigated the application of Automated Fibre Placement (AFP) technology in the manufacturing of composite parts for small aircraft and found that AFP resulted in significant improvements in production efficiency and reduced manufacturing costs.

The use of composites in small aircraft has also resulted in improvements in aerodynamic performance. Composites offer superior stiffness and strength compared to traditional metal structures, which can result in improved aerodynamic performance. For example, Puri et al. [9] investigated the use of composites in the design of a small unmanned aerial vehicle (UAV) and found that the use of composites resulted in improved aerodynamic performance and increased payload capacity.

The application of composites in aircraft design is expected to continue to grow in the future, with the development of new materials and manufacturing processes.

2.2 Optimization of composite structures

The optimization of composite structures in aircraft design is crucial to achieve the desired performance and weight reduction goals. Several optimization techniques have been developed for the design of composite aircraft structures. The composite components can be optimized using topology optimization, material selection, layup sequence, ply orientation and ply thickness mainly among others [10], [11]. Particularly for the aircraft structural field, there are some known optimization techniques implemented in FEM. Such as Altair 3 Phases Method (Figure 1), Zone Based Method (Figure 2) and Zone Based Method with Direct Laminate Implementation (Figure 3) [12]. The first method can be explained as Phase I optimizes the generating ply layout with the orientation and the thickness. Phase II refines the number of plies obtained in phase I. The final design is completed in phase III where the stacking sequence is optimized [13]. As the optimization tool, there are numerous attempts to use various optimization algorithms in literature such as artificial intelligence [14], artificial neural network-differential evolution approach [15], and genetic algorithm [16].

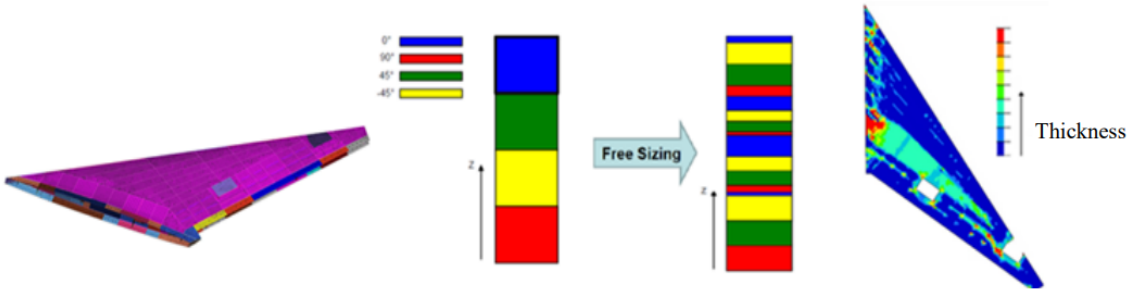

Figure 1: Altair 3 phase method [12].

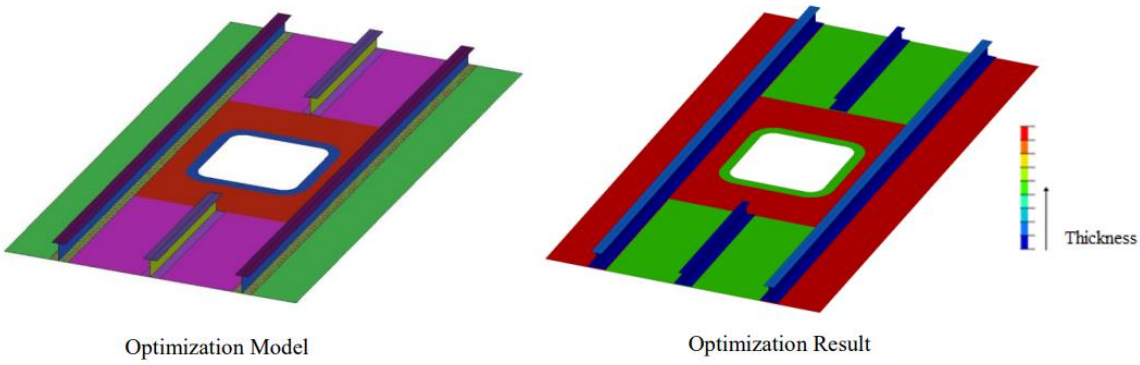

Figure 2: Zone based method, optimization example [12].

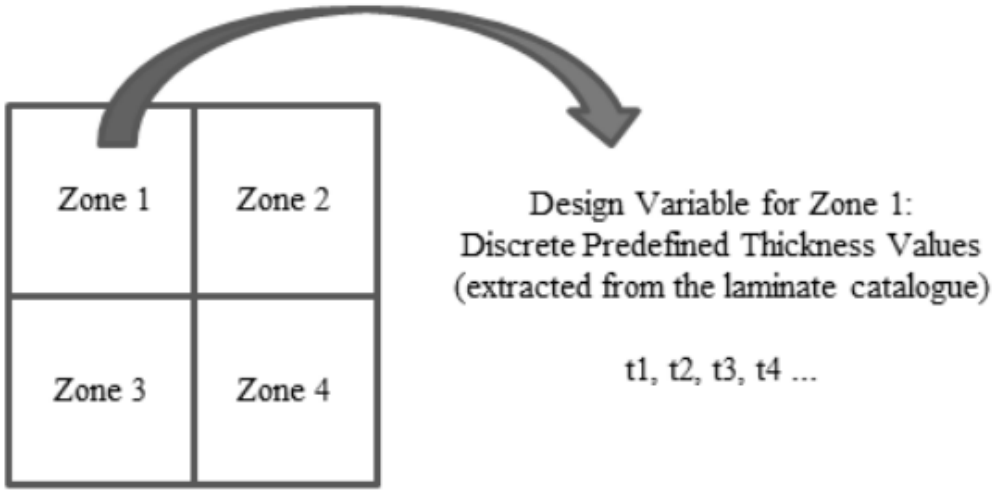

Figure 3: Zone based method with direct laminate implementation optimization scheme [12].

There are some commercial software available for optimizing composite structures such as ANSYS prepPost with optiSLang, Abaqus CAE with Isight plugin and OptiStruct.

ANSYS combined with optiSLang, a process integration and optimization tool, offers a powerful solution for optimizing composite structures. Which uses robust material modelling and advanced failure analysis such as delamination, fibre breakage, and matrix cracking. ANSYS also provides detailed stress, strain, and displacement outputs at the ply level, allowing

for in-depth analysis of local behaviour and identification of potential failure zones. optiSLang offers a range of optimization algorithms, including genetic algorithms and response surface methodologies, to explore and exploit the design space effectively. optiSLang is a commercial software, and obtaining licenses for both ANSYS and optiSLang may involve significant costs, particularly for smaller organizations or individual users. Moreover, performing composite optimization with ANSYS can be computationally demanding, particularly for large and complex models [17]. Extensive computing resources and time may be necessary to achieve optimal results.

Abaqus CAE provides a wide range of material models for composite materials and failure criteria, including Tsai-Hill and Hashin's criteria, enabling the assessment of composite ply failure and prediction of structural performance. Abaqus offers detailed stress and strain outputs at the ply level, facilitating the evaluation of local failure and deformation behaviour. It can also be integrated with optimization tools, such as Isight, to automate the optimization process and explore design spaces. Isight provides a range of optimization algorithms, including genetic algorithms, particle swarm optimization, and gradient-based methods. Moreover, Isight supports the Design of Experiments (DoE) techniques, enabling efficient exploration of the design space and identification of influential design variables through sensitivity analysis. However, the integration of Isight with Abaqus may have limitations in terms of direct control and customization of the underlying simulation parameters and settings. And performing composite optimization using Abaqus can be computationally expensive, especially for large and complex models, requiring substantial computational resources and time [18].

OptiStruct is a popular optimization software developed by Altair. It offers a comprehensive suite of optimization algorithms and capabilities specifically tailored for structural optimization, including composite structures. OptiStruct provides advanced algorithms for topology optimization, sizing optimization, and shape optimization of composite structures, allowing for innovative designs and improved performance. OptiStruct offers specific tools and techniques for composite material optimization, including ply orientation and laminate optimization. This software mainly uses gradient based optimization algorithms. However, OptiStruct is a commercial software, and acquiring licenses may involve significant costs [13].

2.3 Composite material failure analysis

Composite material failure consists of two major elements, lamina failure and laminate failure. Lamina failure can occur in three main modes, namely fibre breakage, transverse matrix cracking and shear matrix cracking. Existing failure criteria such as Maximum Stress/Strength, Maximum Strain/Energy, Hashin, Tsai Hill and Tsai-Wu can be used to predict lamina failure. Methods such as ply by ply discount method, sudden failure method and Hart-Smith criterion are used as laminate failure prediction methods [19]–[21]. This section presents the available failure criterion in Abaqus software.

The Tsai-Hill criterion for composite material made of unidirectional laminates based on an energetic principle assumes that the interaction between the stress tensor components and the failure envelope can be obtained as follows,

$$\left(\frac{\sigma_{11}}{X}\right)^2 + \left(\frac{\sigma_{22}}{Y}\right)^2 - \left(\frac{\sigma_{11}}{X}\right)\left(\frac{\sigma_{22}}{Y}\right) + \left(\frac{\tau_{12}}{S}\right)^2 = 1 \qquad (1)$$

where,

σ_{11} – Applied normal stress

σ_{22} – Applied transverse stress

τ_{12} – Applied shear stress

X – Limit normal stress (Compression or tensile)

Y – Limit transverse stress (Compression or tensile)

S – Limit shear stress (Compression or tensile)

The Tsai-Wu failure criteria for composite material made of unidirectional laminates assume the interaction between the stress tensor components and that represents a plain-stress problem. The failure envelope can be calculated as,

$$F_1\sigma_{11} + F_2\sigma_{22} + F_{11}\sigma_{11}^2 + F_{22}\sigma_{22}^2 + 2F_{12}\sigma_{11}\sigma_{22} + F_{66}\tau_{12}^2 = 1 \qquad (2)$$

where,

$$F_1 = \frac{1}{X_T} + \frac{1}{X_C}, \qquad F2 = \frac{1}{Y_T} + \frac{1}{Y_C}, \qquad F11 = -\frac{1}{X_T X_C},$$

$$F22 = -\frac{1}{Y_T Y_C}, \qquad F66 = \frac{1}{S_{12}^2}, \qquad F12 = -\frac{1}{2}\sqrt{\frac{1}{X_T X_C}\frac{1}{Y_T Y_C}}$$

where,

X_T – Limit tensile normal stress

X_C– Limit compressive normal stress

Y_T – Limit tensile transverse stress

Y_C – Limit compressive transverse stress

S_{12}– Limit shear stress

2.4 Genetic Algorithm

Genetic Algorithm (GA) is a population-based metaheuristic optimization algorithm inspired by the process of natural selection and genetics. It is widely used to solve complex optimization problems where traditional optimization methods may be inefficient or impractical. The GA-based optimization process involves generating a population of candidate solutions, evaluating their fitness using a fitness function, and iteratively applying genetic operators, such as crossover and mutation, to generate new populations. The process continues until a satisfactory solution is obtained.

The main idea behind genetic algorithms is to represent potential solutions to a problem as individuals within a population. Each individual, also known as a chromosome, is encoded as a string of genes, which can be thought of as variables or parameters of the problem. Initially, the population is randomly generated or initialized.

The GA process consists of several steps:

Evaluation - Each individual in the population is evaluated based on a fitness function, which quantifies its performance or suitability as a solution to the problem being optimized.

Selection - Individuals with higher fitness values have a higher chance of being selected for reproduction. This selection process is often biased towards the best individuals, but some diversity is also maintained to explore the search space effectively.

Reproduction - Selected individuals are used to create offspring through genetic operators such as crossover (combination of genetic material from two parents) and mutation

(introduction of random changes to the offspring's genes). These operations simulate the recombination and variation processes in biological evolution.

Replacement: The offspring replace some individuals in the current population, ensuring the population size remains constant. The replacement may be based on fitness values, allowing better individuals to survive and propagate their genes to subsequent generations.

Iteration: The process of selection, reproduction, and replacement is repeated for multiple generations until a stopping criterion is met. This could be a maximum number of iterations, convergence of fitness values, or reaching a desired solution quality.

By iteratively evolving the population through selection, reproduction, and replacement, genetic algorithms explore the search space and converge towards optimal or near-optimal solutions. They are effective in handling large and complex optimization problems with multiple objectives, non-linear relationships, and discrete or continuous variables. While genetic algorithms have proven to be powerful tools, their performance depends on the careful selection of parameters such as population size, selection criteria, genetic operators, and termination conditions. Fine-tuning these parameters and problem-specific considerations is essential for achieving optimal results [22], [23].

2.5 Surrogate models

Many industries where complex numerical analysis such as finite-element method (FEM), computational fluid dynamics (CFD), or structural finite-element analysis (FEA) utilize surrogate models [24]–[26]. Especially for optimization tasks where the computational simulations are very computationally expensive. The main purpose of using a surrogate model is to numerically approximate the expensive high modality models. The surrogate models are generated using a relatively low number of simulations to obtain input to output values [26].

After defining the input parameters of the model, the number of samples and the combinations to simulate must be decided, which has a direct influence on the precision of the model. Design of Experiments (DoE) can be used for this process. Among other sampling techniques such as orthogonal sampling and Box-Behnken design, the Latin Hypercube Sampling (LHS) is the most frequently used and efficient method. LHS provides random sampling points distributed along the design space [27]. In order to generate the numerical model, a regression method can be used.

For multi variable regression cases, the model can be defined for a deterministic function of $f: R^d \rightarrow R$, where the input variables are $X = (x_1, x_2, \ldots, x_d)$, d being the number of dimensions of $X^L \leq X \leq X^U$, where the limits are upper and lower bounds. The surrogate model generates a function $\hat{f}(X)$ that approximates the function *f*.

Many build-in software tools are available with integrated DoE and regression methods, such as MATLAB toolboxes, MATSuMoTo, python toolboxes (PyDoe, ScikitLearn) and SurroOpt. It is important to validate the generated model, which is a process of ensuring the reliability of the surrogate model. Which can be also used to select the most accurate model for the application. In order to validate the models a test sample set should be simulated and obtain the simulated results as well as the predicted results from the surrogate model. The measurements commonly used for validating the results are mean absolute error, mean squared error, median absolute error, the R-squared score and the relative average absolute error. Some of the equations are presented in Equation 3, Equation 4 and Equation 5.

$$Mean\ squared\ error = \frac{1}{n_{samples}} \sum_{i=0}^{n_{samples}-1} (y_i - \hat{y})^2 \quad (3)$$

$$R\ squared\ value = 1 - \frac{\sum_{i=0}^{n_{samples}-1}(y_i - \hat{y_i})^2}{\sum_{i=0}^{n_{samples}-1}(y_i - \bar{y})^2} \quad (4)$$

$$Relative\ average\ absolute\ error = \frac{\sum_{i=0}^{n_{samples}-1}|y_i - \hat{y_i}|}{n_{samples} * STD} \quad (5)$$

where,

$STD - Standard\ deviation$

$n_{samples} - Number\ of\ testing\ samples$

$y - deterministic\ function$

$\bar{y} - Mean\ value$

$\hat{y} - Surrogate\ model\ functoin$

2.6 Regression methods

Regression methods are used to approximate the deterministic function. Frequently used regression methods are Linear regression, Radial basis functions [28]. Some of the regression methods available on ScikitLearn plugin that can be implemented on python are described below [29].

Linear regression (Equation 6) assumes a linear relationship between the input features and the target variable, aiming to find the best-fit line that minimizes the sum of squared residuals (Equation 7). The coefficients learned by the model represent the slopes or weights assigned to each input feature, indicating their impact on the target variable. Linear regression can handle both simple linear regression problems, where there is only one input feature, as well as multiple linear regression problems. Linear regression implementation allows for easy integration with other Scikit-Learn functionality, such as data preprocessing, feature scaling, and cross-validation. This makes it convenient to incorporate linear regression into a broader machine learning pipeline.

$$\hat{y}(w, x) = w_0 + w_1x_1 + w_2x_2 + .. + w_px_p \quad (6)$$

$$\min_w \|Xw - y\|_2^2 \quad (7)$$

where,

$w_i - Coefficients\ of\ the\ surrogate\ model$

$x_i - Variables$

Ridge regression is a linear regression model with L2 regularization. It is a powerful algorithm for handling multicollinearity in data and controlling the magnitude of the coefficient estimates. The Ridge model adds a penalty term to the ordinary least squares objective function, which is proportional to the sum of the squared values of the coefficients multiplied by a regularization parameter (alpha). This penalty term helps to control the complexity of the model by shrinking the coefficients towards zero, reducing their magnitudes and mitigating the effects of multicollinearity (Equation 8).

$$\min_{w} \|Xw - y\|_2^2 + \alpha\|w\|_2^2 \tag{8}$$

Ridge regression is particularly useful when dealing with datasets that exhibit multicollinearity, where predictor variables are highly correlated. By applying L2 regularization, Ridge regression helps to reduce the impact of multicollinearity by shrinking the coefficients towards zero, resulting in more stable and interpretable models. The regularization parameter alpha controls the amount of regularization applied. Larger values of alpha result in more pronounced shrinkage of the coefficients, reducing their magnitudes and preventing overfitting. Smaller values of alpha allow the coefficients to have larger magnitudes, allowing the model to fit the training data more closely.

Lasso (Least Absolute Shrinkage and Selection Operator) is a linear regression model with L1 regularization. It is a powerful algorithm for feature selection and can effectively handle high-dimensional data by encouraging sparsity in the coefficient estimates. The Lasso model adds a penalty term to the ordinary least squares objective function, which is proportional to the sum of the absolute values of the coefficients multiplied by a regularization parameter (alpha). This penalty term promotes sparse solutions, meaning it encourages some coefficients to be exactly zero, effectively performing automatic feature selection (Equation 9).

$$\min_{w} \frac{1}{2n_{samples}} \|Xw - y\|_2^2 + \alpha\|w\|_1 \tag{9}$$

Lasso is particularly useful when dealing with high-dimensional datasets and situations where feature selection is desired. By encouraging sparsity in the coefficient estimates, Lasso can effectively identify and select the most relevant features for prediction, reducing the impact of irrelevant or redundant features. The regularization parameter alpha controls the balance between fitting the training data and the amount of regularization applied. Larger values of alpha lead to more coefficients being set to zero, resulting in sparser models. Smaller values of alpha allow more coefficients to have non-zero values. The lasso estimate solving the minimization of the least-squares penalty with $\alpha\|w\|_1$ added, where α is a constant and $\|w\|_1$ is the l_1-norm of the coefficient vector.

ElasticNet is a linear regression model with combined L1 and L2 regularization. It is a powerful algorithm for handling high-dimensional data and performing feature selection by simultaneously controlling the sparsity and magnitude of the coefficients. The ElasticNet model combines the penalties of L1 regularization (Lasso) and L2 regularization (Ridge). L1 regularization encourages sparsity by promoting some coefficients to exactly zero, effectively performing feature selection. L2 regularization helps control the magnitude of the coefficients and prevents overfitting (Equation 10).

$$\min_{w} \frac{1}{2n_{samples}} \|Xw - y\|_2^2 + \alpha\|w\|_1 + \frac{\alpha(1-\rho)}{2}\|w\|_2^2 \quad (10)$$

Gaussian regression is a supervised learning algorithm that models the relationship between input variables and a continuous target variable using a Gaussian distribution. It is a flexible and powerful method for regression tasks that can capture complex non-linear relationships. The main idea behind Gaussian regression is to assume that the target variable follows a Gaussian (normal) distribution. Given a set of input variables and their corresponding target values, the algorithm learns the parameters of the Gaussian distribution that best describe the relationship between the inputs and the target. Gaussian regression offers flexibility in choosing the covariance function, also known as the kernel function. Different kernel functions capture different patterns in the data, allowing the model to adapt to various types of relationships.

Gaussian regression is particularly useful when dealing with small to moderate-sized datasets, where it can effectively capture complex relationships and provide uncertainty estimates. However, it may become computationally expensive for larger datasets due to the need to invert the covariance matrix.

2.7 UAV for medical delivery

Unmanned Aerial Vehicles (UAVs), commonly known as drones, have emerged as a promising technology for medical delivery in various healthcare settings. UAVs offer the potential to enhance the efficiency, accessibility, and timeliness of medical supply delivery, particularly in remote or inaccessible areas.

The use of UAVs for medical delivery has several advantages. Firstly, UAVs can overcome geographical barriers and deliver medical supplies to hard-to-reach locations, including rural areas, disaster-stricken regions or places with harsh climate conditions where rapid manned access is not possible. They can bypass infrastructural limitations such as damaged roads or inadequate transportation networks, ensuring prompt delivery of critical healthcare resources. Secondly, UAVs have the capability to transport medical supplies swiftly, reducing delivery times and enhancing emergency response. This rapid delivery can be crucial in time-sensitive situations, such as delivering life-saving drugs, blood products, or emergency medical equipment to remote locations or during natural disasters. Moreover, UAVs can optimize supply chain logistics by reducing costs associated with traditional delivery methods. They eliminate the need for human transportation, which can be expensive and time-consuming. Additionally, UAVs can operate autonomously, allowing for round-the-clock delivery services without the limitations of human fatigue or working hours.

However, there are certain challenges and considerations when deploying UAVs for medical delivery. Regulatory frameworks and airspace management must be established to ensure safe and efficient operations. Integration with existing healthcare systems and coordination with healthcare providers is essential to ensure seamless integration of UAV deliveries into the healthcare workflow. Furthermore, issues such as payload capacity, battery life, and weather conditions can impact the range and reliability of UAV deliveries. Robust navigation systems, obstacle detection and avoidance mechanisms, and effective communication networks are crucial to ensure accurate and secure delivery operations.

The following cases are some existing applications,

Remote Areas: In regions with limited infrastructure and difficult terrain, UAVs have been used to deliver medical supplies, such as vaccines, medications, and diagnostic samples, to remote communities. For instance, in Rwanda, Ghana, the company Zipline has implemented a

network of UAVs to deliver blood products to rural areas, ensuring timely access to critical transfusions [30]. They have partnered with local governments and healthcare providers to deliver supplies to remote areas. Zipline's drones are capable of making long-range deliveries and have successfully facilitated thousands of medical deliveries in challenging terrains.

Figure 4: zipline UAV - P1 Zip [30].

DHL partnered with the Tanzanian government and other organizations to launch a drone delivery service for medical supplies. The project aimed to improve access to essential medicines and vaccines in remote areas. Drones were used to transport supplies from a central location to health facilities located in hard-to-reach regions, significantly reducing delivery times [31], [32].

Figure 5: DHL and Tanzania drone project [33].

Urban Areas: UAVs can also be deployed in densely populated urban areas to enhance medical delivery efficiency. They can assist in the rapid transport of medical supplies between hospitals, clinics, and laboratories, reducing traffic congestion and delivery times. California's UC San

Diego Health collaborated with UPS to establish a program utilizing drones for medical deliveries. The program involved transporting medical samples such as blood tests and specimens between health facilities within the UC San Diego Health system. The drones allowed for faster and more efficient transportation of critical samples, reducing the time required for diagnosis and treatment [34].

Figure 6: UC San Diego Health Drone Delivery Program [34].

Matternet, a drone logistics company, partnered with Swiss Post to launch a drone delivery network for medical samples in Switzerland. The project involved transporting lab samples, such as blood tests and pathology specimens, between hospitals and laboratories. The use of drones significantly reduced transportation times and provided an efficient and reliable method for delivering time-sensitive medical samples [35].

Figure 7: Switzerland's medical drones take off [35].

Island Communities: Islands often face challenges in accessing medical resources due to their geographical isolation. UAVs offer a solution by enabling the transport of medications, medical equipment, and even organs for transplantation between islands. In Scotland, the "Drone Blood"

project explored the use of UAVs to transport blood samples and other medical supplies between remote islands [36].

Figure 8: NHS medical delivery drone project [36].

UK's National Health Service (NHS) partnered with Windracers, an aerospace logistics company, to conduct a trial using long-range UAVs for medical supply delivery. The project aimed to transport medical items, including Personal Protective Equipment (PPE) and COVID-19 test kits, between the mainland and the Isle of Mull, a remote island off the coast of Scotland. The UAVs successfully delivered essential supplies, demonstrating the potential of drones to support healthcare services in remote areas [37].

Figure 9: UK's National Health Service (NHS) and Windracers medical delivery drone project [37].

2.8 Aircraft Sizing – Fixed-wing UAVs

There are many available methodologies that can be used for fixed-wing UAV sizing depending on the expected results. Some of the main works of literature that can be used are, "Aircraft Design: A Conceptual Approach" by Daniel P. Raymer [38], "Introduction to Flight" by John D. Anderson Jr [39], "Aircraft Systems: Mechanical, Electrical, and Avionics Subsystems Integration" by Ian Moir and Allan Seabridge [40], "Aircraft Design: A Systems Engineering Approach" by Mohammad H. Sadraey [41] and "Introduction to Unmanned Aircraft Systems" by Douglas M. Marshall and Richard K. Barnhart [42].

The following equations and methods are adapted from the literature for sizing and performance analysis. Following equations allow to estimate the total weight of the UAV and the battery weight with the structural weight ratio and the propulsion weight ratio keeping the payload weight fixed. The battery weight is estimated with the power required for the performance.

$$W_{TO} = (W_{ST}/W_{T0}) * W_{T0} + (W_{PR}/W_{T0}) * W_{T0} + W_{PL} + W_{Bat} \quad (11)$$

$$P_R = \frac{W_{To}}{\frac{C_L}{C_D}} * V_c \quad (12)$$

$$E_R = P_R * \Delta t \quad (13)$$

$$W_{bat} = \frac{E_R}{SED} \quad (14)$$

where,

W_{TO} – Take off weight of the aircraft

W_{ST}/W_{T0} – Structural to total weight ratio

W_{PR}/W_{T0} – Propulsion to total weight ratio

W_{PL} – Payload weight

W_{Bat} – Battery weight

P_R – Power required

Vc – Cruising velocity

$\frac{C_L}{C_D}$ – Lift to drag coefficient

E_R – Energy required

Δt – Endurance

SED – Specific Energy density

Geometry parameters,

$$C = \frac{b}{AR} \tag{15}$$

$$S = b * C \tag{16}$$

$$WingLoading = \frac{W_{TO}}{S * g} \tag{17}$$

$$Re = \frac{\rho v l}{\mu} = \frac{v l}{\nu} \tag{18}$$

$$Mach = \frac{v}{c} \tag{19}$$

where,

b – Wingspan

C – Wing chord

AR –Wing aspect ratio

g – Gravitational acceleration

S – Wing area

Aerodynamic parameters,

$$L = C_L \frac{1}{2} \rho V^2 S \tag{20}$$

$$C_D = C_{D0} + k\, C_L^2 \tag{21}$$

$$k = \frac{1}{\pi A R e} \tag{22}$$

$$D = C_D \frac{1}{2} \rho V^2 S \tag{23}$$

$$V_{stall} = \sqrt{\frac{W}{\frac{1}{2} C_{L(max)} \rho S}} \tag{24}$$

where,

L – Lift

C_L – Lift coefficient

Vstall – Stall velocity

$C_{L(max)}$ – Maximum achievable lift coefficient

D – Drag

C_D – Drag coefficient

C_{D0} – Drag coefficient

e − wing planform efficiency factor

Take off performance,

$$\frac{dV}{dt} = \frac{T - D - F}{m} \quad (25)$$

$$F = \mu(W - L) \quad (26)$$

$$V_R = 1.1 * V_{Stall} \quad (27)$$

Landing,

$$\frac{dV}{dt} = \frac{-T - D - F}{m} \quad (28)$$

where,

T – Thrust of propulsion system pushing aircraft along the runway

D – Aerodynamic Drag of vehicle resisting the aircraft motion.

F – Rolling resistance friction due to the contact of wheels or skids on the ground

$\frac{dV}{dt}$ – Acceleration along the runway

m – Mass of the aircraft

V_R – Rotation Velocity

μ – Friction coefficient

SED – Specific Energy density

Thrust, power and energy calculations,

$$Tr_{min} = \frac{Wto}{L\_D_{max}} \quad (29)$$

$$PR_{TRmin} = Tr_{min}\frac{Vc}{n} \quad (30)$$

$$V_{TRmin} = \sqrt{2\frac{\frac{Wto}{S}}{\rho}\left(\frac{k}{CD0}\right)}^{0.25} \quad (31)$$

$$CL_{Cruise} = \frac{2Wto}{SV_c^2} \quad (32)$$

$$TR_{Vc} = 0.5\rho Vc^2 SC_D \quad (33)$$

$$PR_{Cruise} = TR_{Vc} * \frac{Vc}{n} \quad (34)$$

$$PR_{min} = \frac{1}{n} * \sqrt{2 * \frac{Wto^3}{\rho * S}} * \left(\frac{256 * K^3 * C_{D0}}{27}\right)^{0.25} \quad (35)$$

$$ER_{cruise} = PR_{cruise} * \Delta t \quad (36)$$

$$Battery\ Capacity = \Delta t * \left(I_{prop} + I_{PL} + I_{avionics}\right) \quad (37)$$

where,

Tr_{min} – Minimum thrust required

TR_{Vc} – Required thrust for cruising velocity

PR_{Cruise} – Required power for cruising

PR_{min} – Required minimum power

n – Power efficiency

ER_{cruise} – Required energy for the cruising

I_{prop} – Current required for the propulsion system

I_{PL} – Current required for payload

$I_{avionics}$ – Current required for avionics

Performance,

$$Endurance = \frac{E_{availble}}{PR_{cruise}} \tag{38}$$

$$Range = \Delta t_{available} * V_{cruise} \tag{39}$$

$$Rate\ of\ Climb\ = \frac{Excess\ power}{W_{to}} = \frac{Available\ power - PR_{Cruising}}{W_{to}} \tag{40}$$

Tail sizing and Longitudinal stability equations are presented in Appendix A.

2.9 V-n diagram

The V-n diagram, also known as the "flight envelope" diagram, is a graphical representation used in aviation to depict the permissible limits of an aircraft's manoeuvring capability. It provides a visual understanding of the relationship between an aircraft's load factor and its corresponding airspeed. The V-n diagram holds significant importance in structural analysis for aircraft design and analysis. V-n diagram can be used to obtain load limitations, structural integrity, design optimization, compliance with regulation, safety assessment and performance evaluation.

Generally, V-n diagrams are prepared for various flight conditions such as configuration variations, altitudes and weight variances. The aviation regulations always specify how to construct the effect of each event in applicable paragraphs that can be followed. For light aircraft sizing the EASA regulations for very light aircraft (CS-VLA) and CS-23 regulations for light aircraft can be used [43].

In the case of low-weight UAVs with low wing loadings, the conventional V-n diagram might be not able to obtain as the used regulations are designed for higher weight aircrafts [44]. In these cases, a more convenient alternative can be considered [43]. Some of the issues that can be arise with low wing loading aircraft are presented in Figure 10, while some of the different types of V-n diagrams are presented in Figure 11.

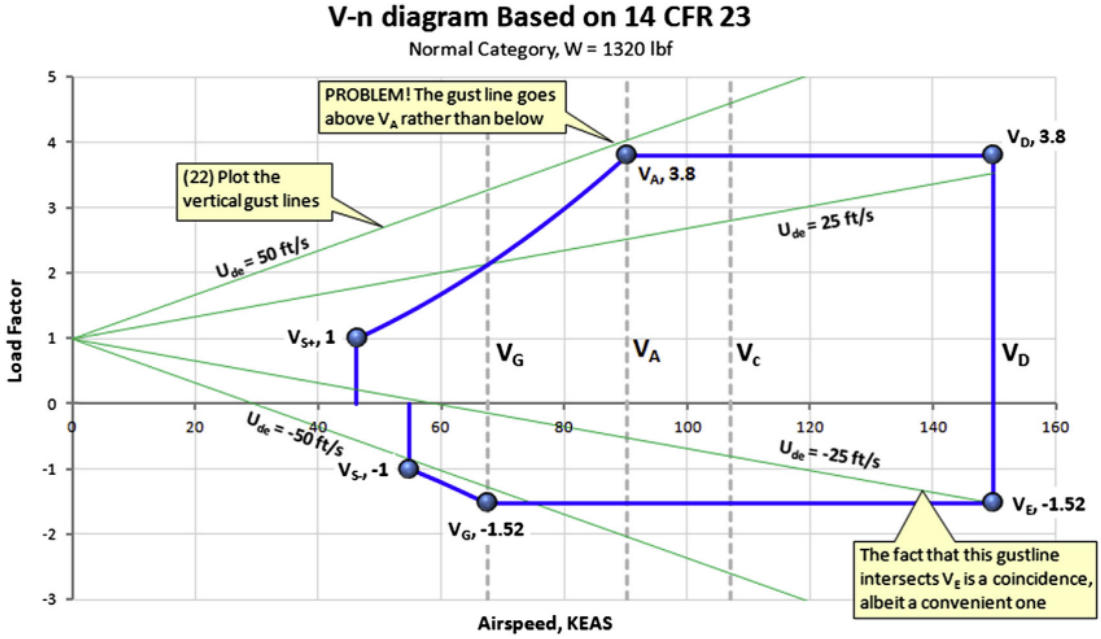

Figure 10: Highlighting the influence gust lines in non-conventional V-n diagrams [43].

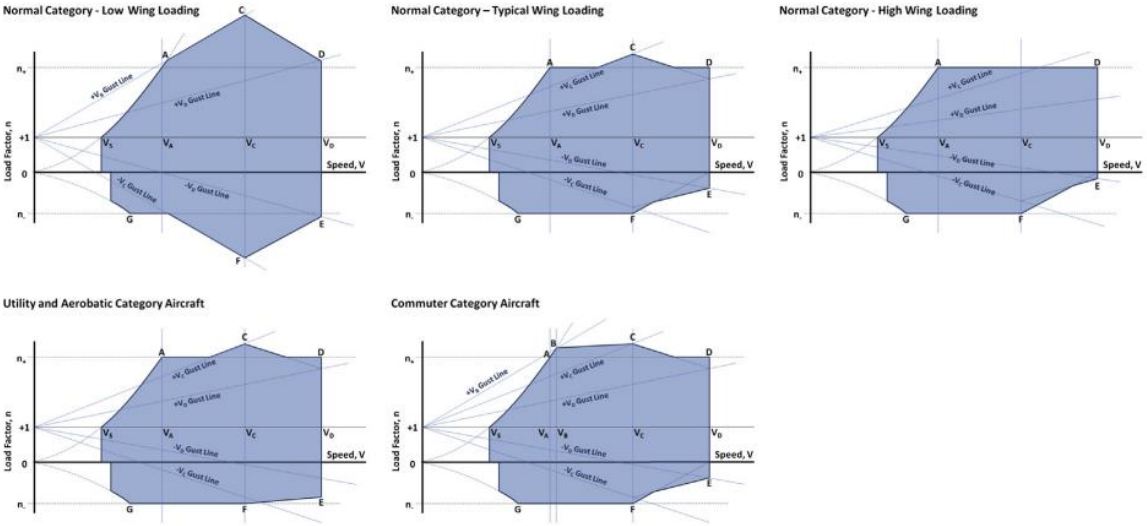

Figure 11: Different types of V-n diagrams [43].

3 First aircraft prototype – Design and manufacturing

As described in the introduction, to apply the methodology and manufacturing, the first aircraft prototype is sized and designed. After manufacturing and test flights, this aircraft is aimed to fly in Nepal at 3000m altitude for 100 km round trip. This aircraft will be used to obtain the flight data of these test flights to further optimize the sizing methods, verify the structural integrity, test the autonomous flight controller, plan the navigation system and performance. The first aircraft is designed according to the following requirements,

- Maximum speed: 200 km/h
- Cruise: 70 km/h
- Range at 3000m: 100 km
- Payload: 1 kg
- Wind tolerance: 50 km/h
- Gust wind: 80 km/h
- Weather: Rain, snow, windy and low temperatures
- Powerplant: Electrical propulsion
- Maximum wingspan: 3 m – For transportation

Other than these requirements, while designing it should be considered that the developed UAV should be easier to transport (easy to assemble and disassemble).

In order to meet the above requirements, the subsequent steps are followed to manufacture the prototype.

1. Historic data analysis to estimate the initial sizing parameters
2. Mission profile definition
3. Initial weight estimation according to the required performance
4. Aircraft sizing – Geometry, powerplant, battery selection
5. Tail sizing
6. Stability analysis
7. Design
8. Structural analysis
9. Manufacturing
10. Test flight

By analysing the fixed-wing electrical UAVs that match the given requirements such as Yangda FW-250 and KapetAIr, the following initial parameters are determined,

- Aspect ratio = 10
- Initial total weight = 10 kg
- Structural to total weight ratio = 0.4
- Propulsion to total weight ratio = 0.15
- Specific energy density of battery (SED) = 180 Wh/kg

As the initial configuration a simple wing geometry is chosen. A V-tail configuration is chosen according to the requirements.

A computational tool is developed for the sizing of lightweight UAVs of the same configuration, given the initial parameters and requirements. This computational tool is not described in depth in this thesis. However, it was used for the sizing of the first aircraft and after validating the methodology it was used for the sizing of the second aircraft. This computational tool uses the equations described in the literature review - section 2.8 - Aircraft Sizing – Fixed-wing UAVs and Appendix A.

3.1 Mission profile

The following mission profile is considered from the requirements.

- Range at 3000m: 100 km
- Cruising speed: 70 km/h

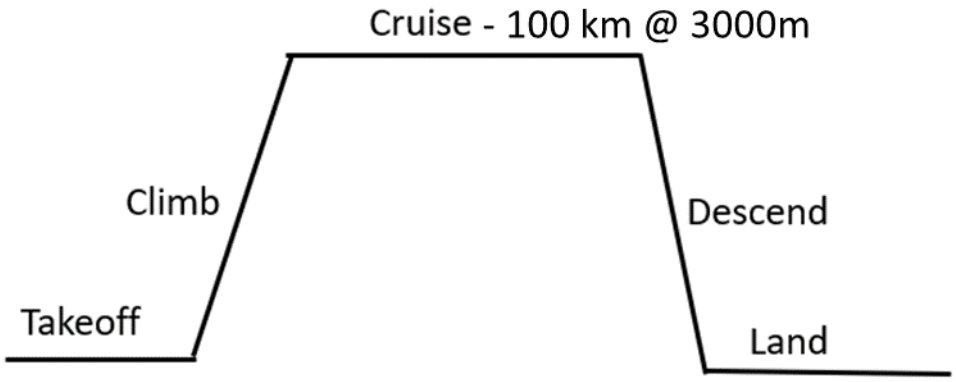

Figure 12: Mission profile of the 1st aircraft prototype.

For simplification and the first iteration all the following calculations are only for the cruising stage of the flight.

3.2 Weight estimation, aircraft sizing and design

The total weight of the UAV can be divided into portions as follows,

- Structural weight
- Payload
- Avionics weight
- Propulsion weight – motor, propeller and ESC
- Battery weight

The structural and propulsion weight are obtained from similar aircraft as a ratio to the total weight. The battery weight is calculated according to the required performance.

In this present case, the following method of iterations of weight estimation is used. In each step where the total weight is estimated, the sizing equations determine the required propulsion and battery weight in order to achieve the required performance.

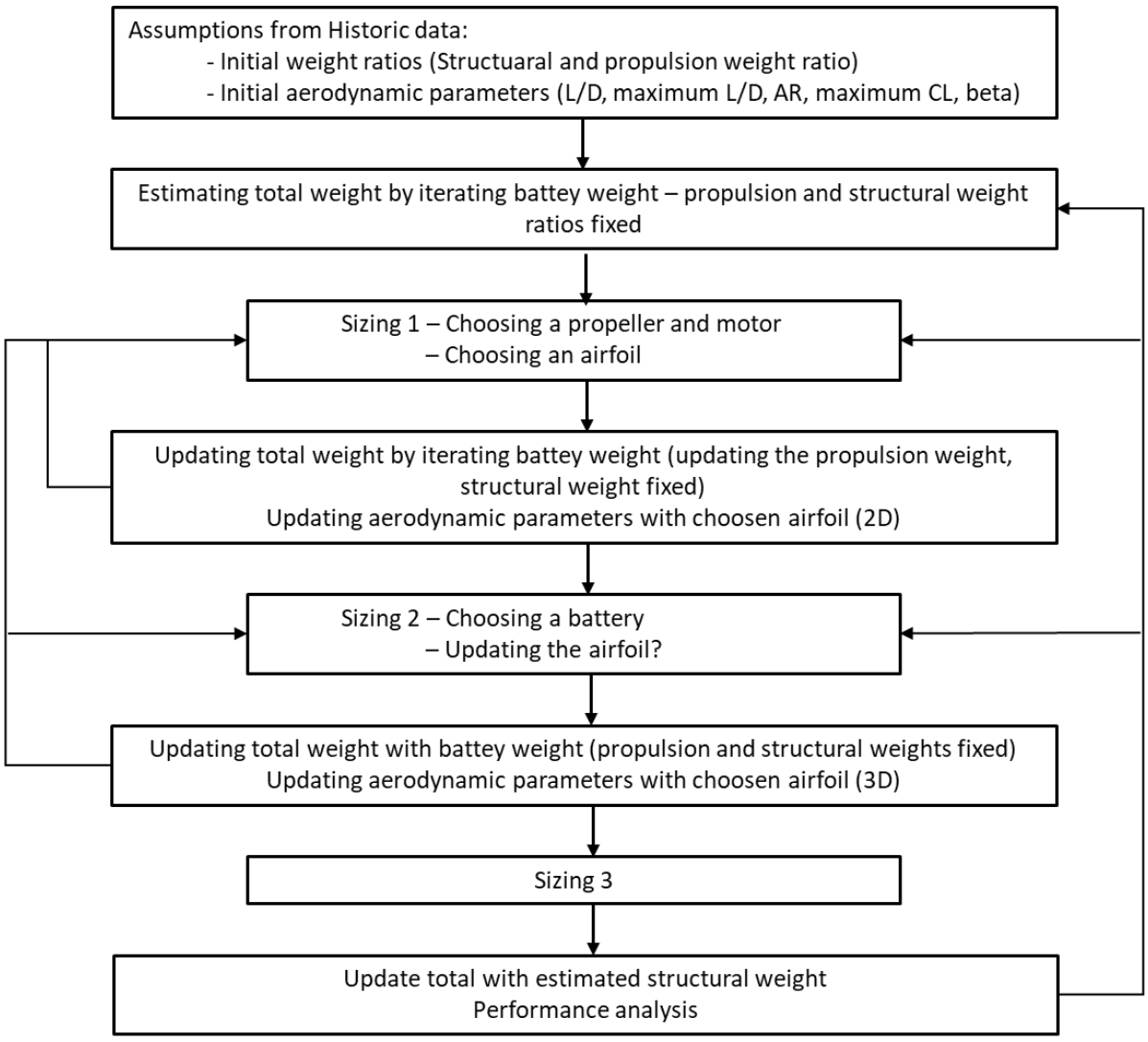

Figure 13: Scheme of the weight estimation and sizing program.

The basic sizing equations are used to calculate performance, stall speed, power, thrust, maximum speed, rate of climb, turn radius and battery capacity. The used sizing procedure is included in the literature review - section 2.8 - Aircraft Sizing – Fixed-wing UAVs. The estimated initial aerodynamic and weight ratios are used in the first sizing calculations.

After the first sizing calculations, the required parameters for choosing a propulsion system and an airfoil (maximum CL required, design CL, L/D and beta) are calculated. The total weight is updated using the propulsion system weight with the chosen motor, propeller and ESC. In sizing 2, the required parameters for battery weight are calculated using the 2D data from the chosen airfoil. A battery is selected accordingly. Sizing 3 calculates the sizing parameters for the updated total weight with the battery and the 3D data from the chosen airfoil. 2D airfoil data and 3D plane aerodynamic parameters were obtained from XFLR5 software.

However, it should be noted that the sizing process consisted of many iterations to obtain the tailored final results. The following results were obtained from the weight estimations and sizing in Table 1,

Table 1: Resultant values from the sizing program.

	Sizing 1	Sizing 2	Sizing 3
Wst_Wto	0.4	0.4	0.4
Wele_Wto	0.15	0.30	0.24
Wto (kg)	**3.619**	**7.726**	**9.779**
Wbat (kg)	**0.627**	**1.336**	**2.5**
Wstructural (kg)	**1.447**	**3.090**	**3.911**
Wpropulsion (kg)	**0.543**	**1.3**	**1.3**
Wavionics (kg)	-	2	2
Wpayload (kg)	1	1	1
Range (km)	128	128	139.813
Endurance (h)	1.736	1.736	1.896
Stall speed (m/s)	8.699	12.710	14.3
Vmax (m/s)	-	-	48.56

The payload weight is fixed considering the requirements. The avionic weight can be predicted from the weight of essential electronic components and the secondary components. The avionics includes components with known weights such as telemetry, receiver, antennas, GPS, power board, autopilot, servos, wires, airspeed sensor, switches, cables and secondary components such as camera, lights and image processing tools. The predicted weight of all the avionics is 2 kg.

In the next step, the tail was sized according to the stability analyses using the equations from Appendix A as well as stability analysis from XFLR5 software. Aileron, elevator and servos are sized by simulating the most critical condition in XFLR5 software and obtaining pressure distribution and hinge moments.

While some requirements such as the expected range for the flight were able to maximize during the sizing, other parameters such as the expected maximum speed were not been able to achieve.

Detail design of the UAV is constructed in CAD software SOLIDWORKS. The prototype is designed considering that it is required to assemble and disassemble easily and pack in a box for transportation. Hence the wing panels (3 panels separately), tail boom, fuselage and tail panels (2 panels separately) can be separated easily.

For the fuselage design, the required payload volume was considered. The avionics and payload were positioned inside in order to balance the C.G. position of the aircraft as required.

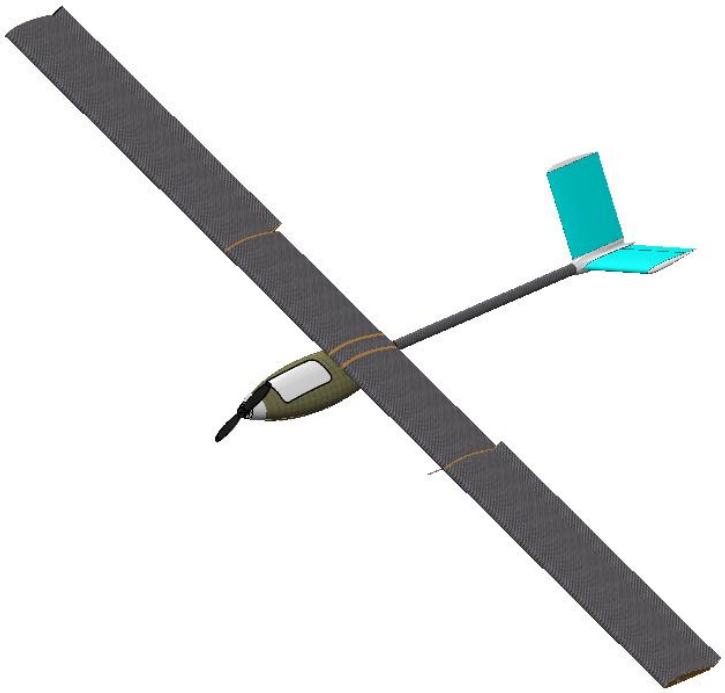

Figure 14: Outside design of the 1st aircraft design - CAD images.

In order to manufacture with the resources and the budget available, a simpler assembly process was designed. The wing consists of a carbon composite spar with plywood ribs at the end of each panel. The wing panels are XPS foam. The wing panel foam is laminated with carbon and glass composites. Wing panel spars are connected to each other by carbon rods and panel connectors. The tail panels are also XPS foam laminated with glass fibre sheets, which also includes carbon composite spar and plywood ribs at the end.

The fuselage is carbon composited laminate on the 3D printed cover. In addition to the carbon layers, Kevlar composite layer is added on the top for belly landing and to absorb impact from crash landing situations. Inside the fuselage, the frames, floor and wing-fuselage connection are designed in plywood. The tail boom is a carbon composite tube which connects to the fuselage through a carbon composite tail boom connection tube which is attached to the fuselage frames. 3D printed fairings are used to provide aerodynamic efficiency.

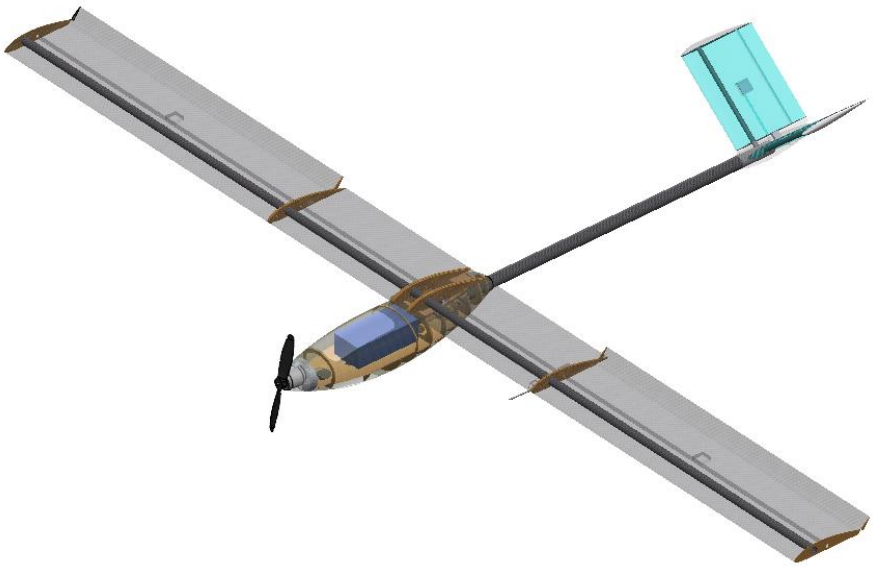

Figure 15: Inside design of the 1st aircraft design - CAD images.

3.3 Structural analysis

This designed aircraft is expected to fly around harsh environmental conditions. V-n diagram is constructed to obtain the structural limits. The V-n diagram was generated considering the sea level's altitude to design a more conservative structure to account for unknown environmental and aerodynamic parameters. In order to resist the high gust wind in the flying region, the maximum gust speeds in the regulations are used for calculations.The following types of loads are considered for the structural analysis,

- Inertial loads
- Aerodynamic loads (gust and manoeuvring loads)
- Propulsion loads

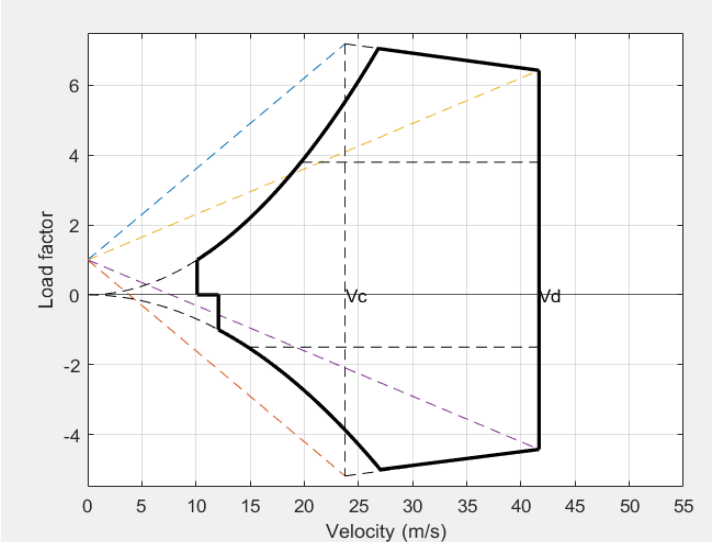

Figure 16: Constructed V-n diagram for structural analysis.

Each point of the V-n diagram is simulated XFLR5 software to obtain the aerodynamic loads. The inertial loads are calculated using the load factor obtained from the above diagram and the calculated horizontal lead factor. Propulsion loads are calculated using the maximum motor and propeller parameters given by the supplier.

The carbon wing spars, tail spars and tail boom tubes are sized analytically according to the classical laminate theory (CLT). Which later tested with the FEM in Abaqus CAE along with the wing tip deflection constraints. The wing spar was sized to take all the wing loads for redundancy. The carbon composite skin, plywood rib thickness, wing-fuselage connection carbon rods and ribs are determined from structural analysis in Abaqus CAE.

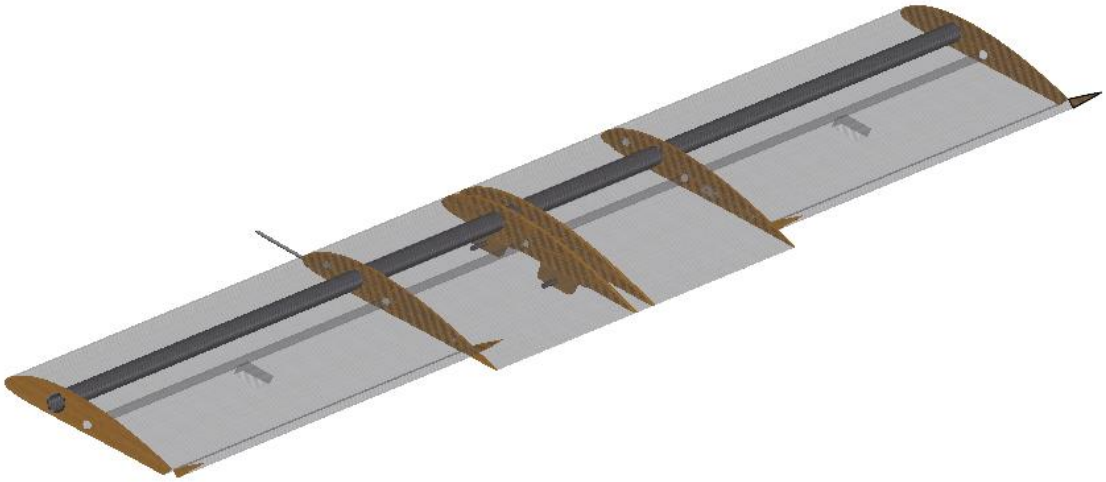

Figure 17: Wing design of the first aircraft prototype - CAD images.

The plywood frames and floor, composite skin in the fuselage is also analysed using Abaqus. For all the analyses a safety factor and a quality factor are considered.

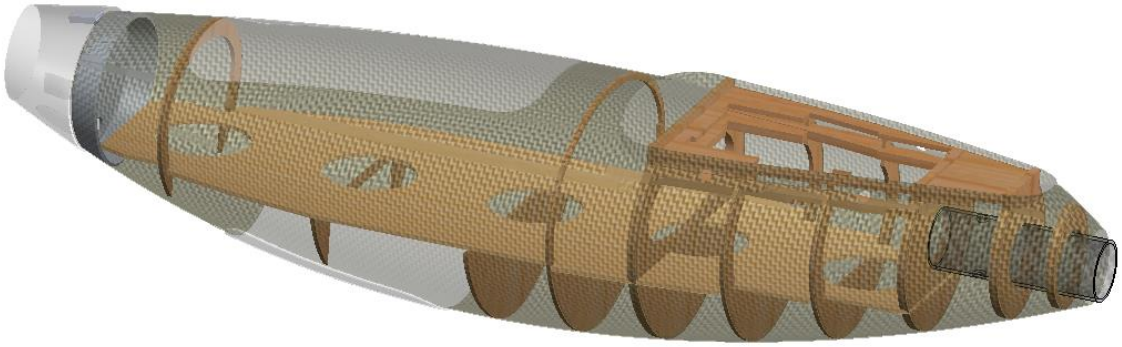

Figure 18: Fuselage design of the first aircraft prototype.

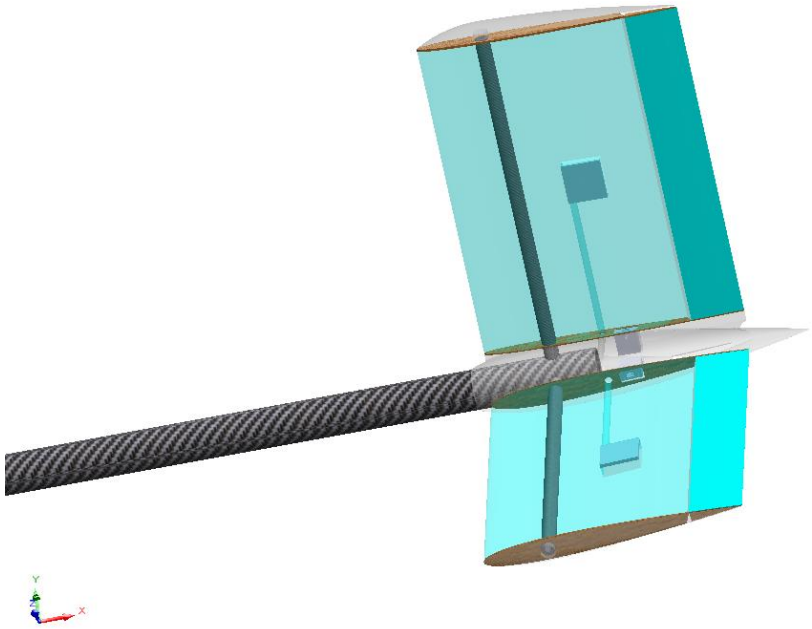

Figure 19: Tail boom and tail design.

3.4 Manufacturing

The designed UAV was manufactured using available resources. The XPS foam for the wing and tail was cut with a 2D CNC hot wire cutter. The plywood ribs for the tail and wing and fuselage frames are cut with a 2D Laser cutter machine. The fuselage model and other plastic parts are printed with a 3D printer using lightweight PLA. The wing, tail and fuselage were laminated with the hand layup method.

The fuselage frames and floor are assembled and glued with the 3D printed outer shape (Figure 20). Then the surface of the 3D printed mould is prepared by sanding. Non-crimp unidirectional carbon fibres and ±45° woven carbon fibre sheets are used with epoxy resin for the composite hand lay up (Figure 21). The layup is finished with ±45° woven Kevlar fibre sheet. A thin layer of white top coating is used to give a light colour finish to the fuselage, which is important to avoid heating up the fuselage (Figure 23). Finally, the excess material is trimmed, and the surface is sanded and polished, the final product is presented in Figure 24. The hole covers are 3D printed with lightweight PLA.

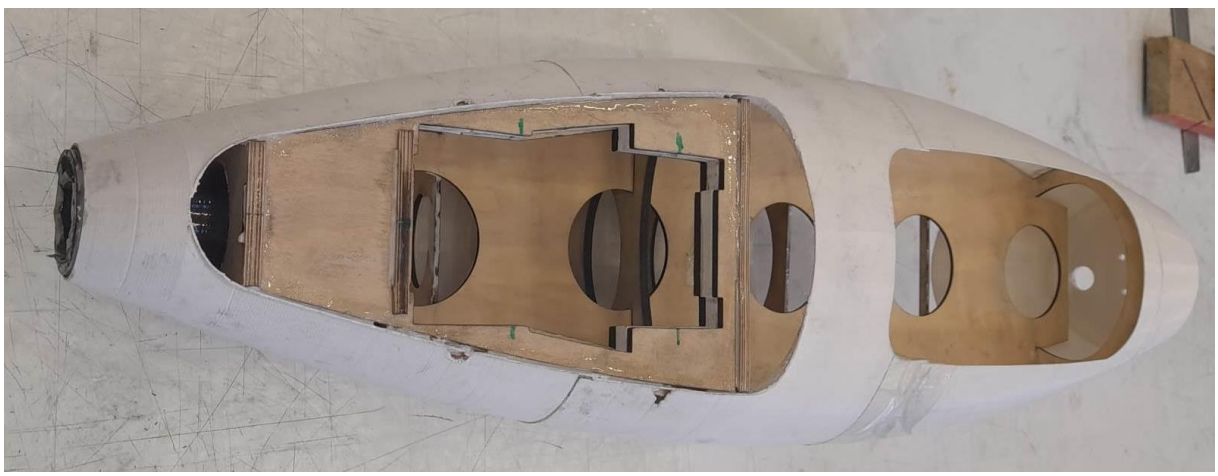

Figure 20: Fuselage with plywood assembly and the 3D printed cover.

Figure 21: Fuselage when laminating with carbon sheets with Epoxy resin - hand layup.

Figure 22: Fuselage laminating with finishing Kevlar sheets.

Figure 23: Applying a white top coating on the fuselage.

Figure 24: Fuselage after trimming, sanding and polishing.

For manufacturing of the wing, the carbon spar tube is inserted to the aerofoil shaped foams. The spar and ribs are glued to the foam using epoxy glue. The wing foams are laminated with ±45° woven carbon fibre sheets using hand layup method. An extra layer of low weight glass fibre layer is added on top for smoother finishing. The excess material trimmed, and the elevators are removed. The space for servos is also cut out. The panels are sanded and polished for smoother finish. The servos are inserted with servo rods and connected to the elevators with servo horns. The elevators are connected to wing panels by hinges and tapes for aerodynamic efficiency. Wing-fuselage connection ribs are imbedded in the middle panel around the spar.

Figure 25: Wing manufacturing with composite hand layup.

The tail is also manufactured by inserting tail spar tubes to the tail aerofoil shaped XPS foams. The spar and plywood ribs are glued to the foam using epoxy glue. The panel connection rod and the piece are glued to the panels. The panels are laminated with glass fibre sheets using epoxy resin.

Figure 26: Tail manufacturing with foam and glass fibre.

The final assembled first aircraft is presented in Figure 27.

Figure 27: First aircraft after assembled.

The weight of all the independent components as well as the assembled UAV was measured in order to compare with the predicted weights ratios. The initially calculated weights, predicted weights after design and the final measured weights are presented in Table 2. After manufacturing around 800 g has been able to reduce from the total expected weight, which can be used to increase the payload capacity or the performance such as range and endurance.

Table 2: UAV weight during sizing, design and after manufacturing.

	Initially calculated weights	Predicted weights after design	Measured weights after manufacturing
Total weight (kg)	9.779	8.612	8.917
Structural weight (kg)	3.911	4.191	4.150
Structural weight ratio	0.4	0.487	0.465
Avionics weight (kg)	2	1.630	1.675
Propulsion weight (kg)	1.3	0.410	0.592
Electronic weight ratio	0.235	0.237	0.142

3.5 Flight test

After manufacturing, all the parts were assembled and the flight was tested in Covilhã, Portugal at around 430 m altitude. The UAV was flown successfully.

Figure 28: First aircraft prototype assembled.

Figure 29: First aircraft flight test photos.

Figure 30: First aircraft flight test photos.

In addition, the flight data was extracted from the telemetry to use in the next version of the UAV. Some of the observed data from a portion of the flight are presented in Figure 30 and Figure 31.

Figure 31: Flight test data of a portion of the flight - Airspeed (m/s) and altitude (m).

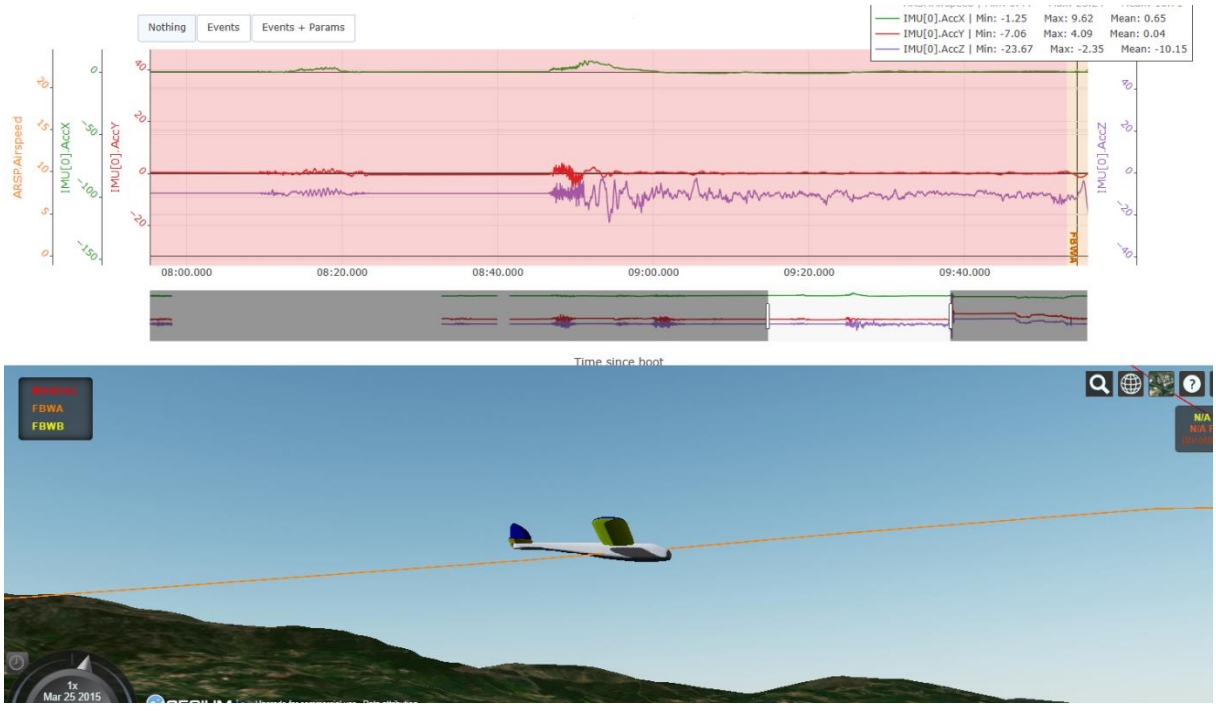

Figure 32: Flight test data of a portion of the flight - X, Y Z acceleration (m/s^2).

4 Medical UAV – Second Aircraft

Following the successful flight testing of the prototype of the first aircraft, the sizing of the optimized Medical UAV (Second Aircraft) has started.

The aircraft is sized using the same methodologies used in the first aircraft sizing with the updated initial parameters obtained from the manufacturing and flight test.

The following requirements are considered in the sizing:

- Maximum speed: 200 km/h
- Cruise speed: 120 km/h
- Minimum speed: 50 km/h
- Range: 150 km @ 5000m
- Payload: 5 kg
- Wind tolerance: 50 km/h
- Gust wind: 80 km/h
- Weather: Rain, snow, windy and low temperatures
- Powerplant: electrical propulsion
- Maximum wingspan: 3 m – For transportation

4.1 Mission profile

In order to calculate the power requirements as well as the performance, the following mission profile is taken into account. Only the takeoff, climbing and cruise stages are considered for the power requirement calculations.

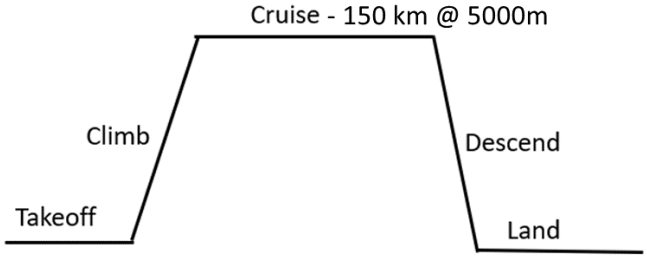

Figure 33: Mission profile of the second aircraft.

4.2 Second Aircraft sizing

This section presents the calculations used for the sizing of the second aircraft. The developed sizing program used in the first aircraft is used here, which provided the aircraft parameters in three sizing steps.

Aerodynamic analysis

For the first iteration of the second aircraft, the wing airfoil and the geometry of the first aircraft wing are tested. To carry out the sizing calculations, the 2D data from the airfoil is required for the calculated flying speeds and altitude.

XFLR5 software is used for the 2D analysis of the wing airfoil. The Reynolds number and the Mach number have to be calculated for the analysis. Two types of flight conditions are analyzed, the cruising condition and the maximum speed flight. Reynolds number for these each flight is calculated using Equation 18 and Equation 19.

Table 3: Data for 2D wing analysis

Kinetic viscosity	1.4207E-5 m^2/s
Chord	0.25 m
Cruise speed	35 m/s
Maximum speed	55 m/s
Speed of sound at 5000m	320 m/s
Mach number at cruise	**0.109**
Mach number at maximum speed	**0.172**
Reynolds number at cruise	**615,894**
Reynolds number at maximum speed	**967,833**

Type 1 analysis for fixed speed with viscous flow is used for the 2D analysis in XFLR5 software. These plots can be used to obtain the initial airfoil data indicated in Figure 34, Figure 35, Figure 36 and Figure 37.

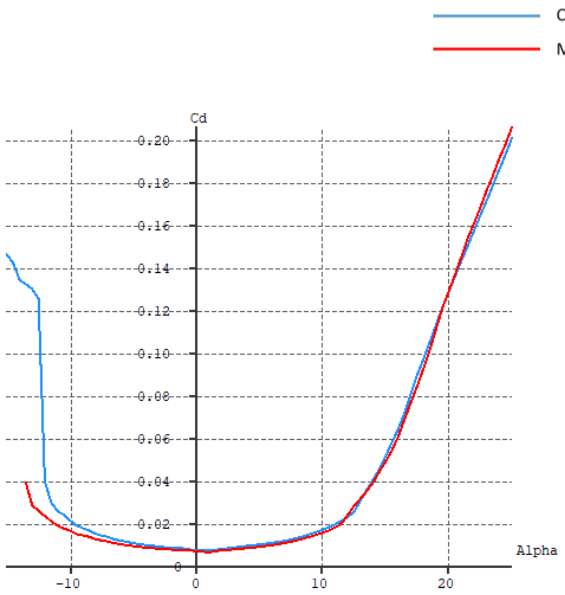

Figure 34: 2D airfoil analysis - Cd vs alpha graph

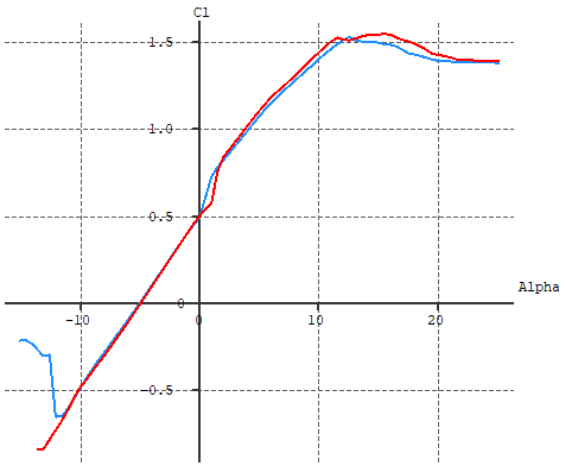

Figure 35: 2D airfoil analysis - Cl vs alpha graph.

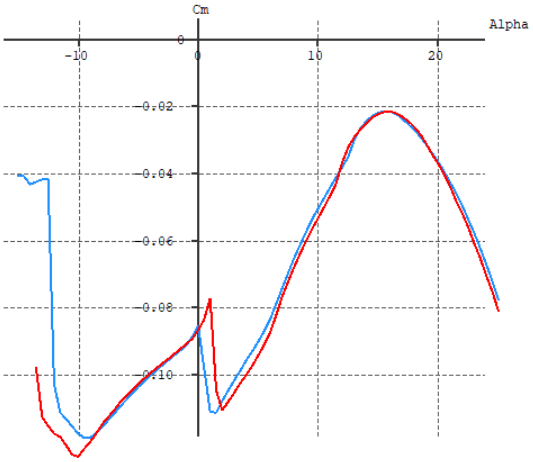

Figure 36: 2D airfoil analysis - Cm vs alpha graph.

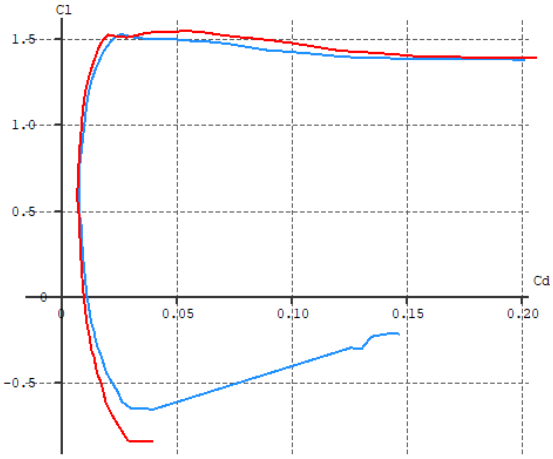

Figure 37: 2D airfoil analysis - Cl vs Cd graph

As the wing dimensions are already known, it is possible to conduct a 3D wing analysis to be used in the sizing. 3D wing analysis was also conducted in XFLR5 software with fixed speed (Figure 38) and wing only analysis which uses the Lifting Line Theorem (LLT) - Figure 39.

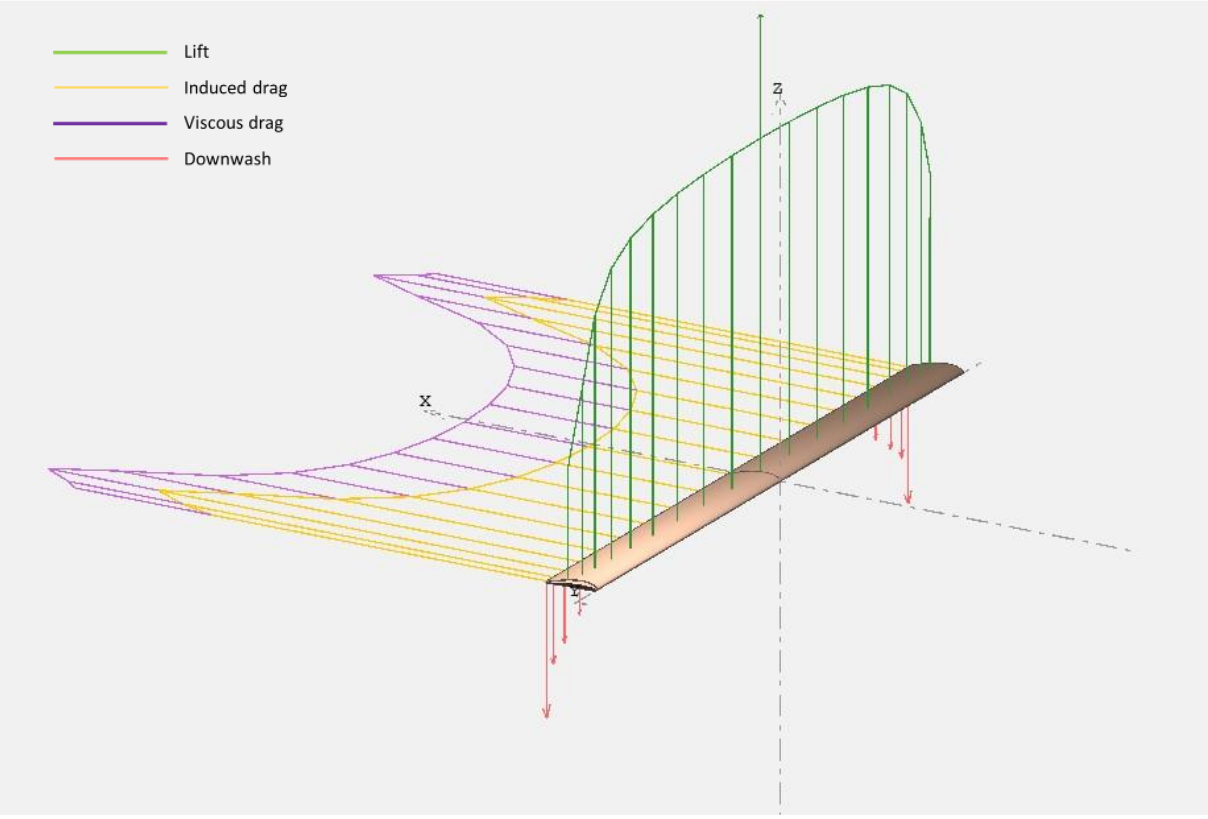

Figure 38: 3D wing panel analysis captured at 3 degrees of AOA.

Aerodynamic analyses can also be conducted to obtain the pressure, lift and drag distribution (Figure 39) through span and chord, which can be later used in load calculations (Table 4).

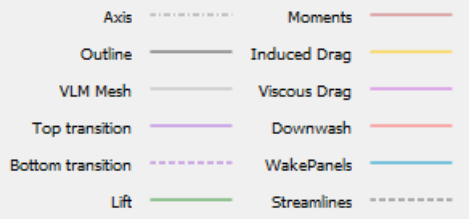

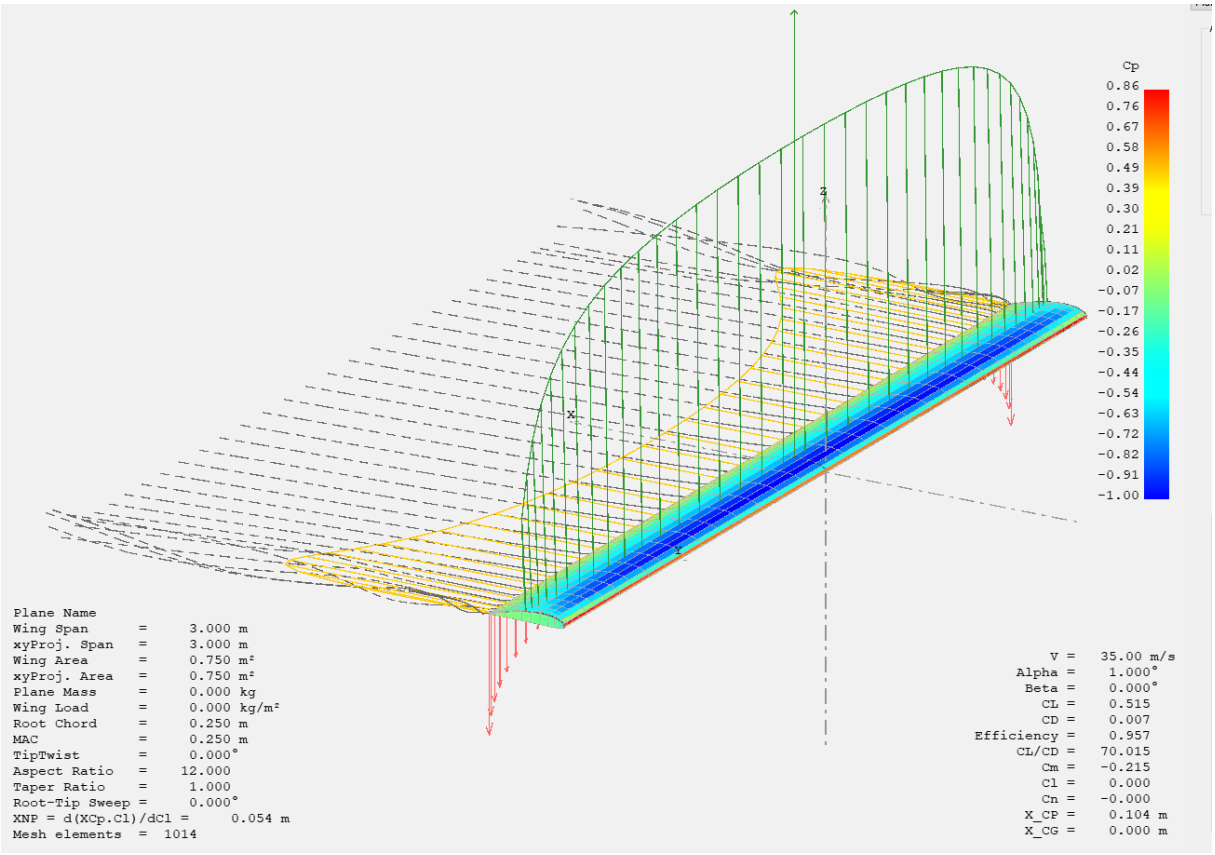

Figure 39: Aerodynamic analysis per wingspan.

Table 4: Airfoil data used for sizing.

Cruising condition	2D	3D
Clmax	1.523	1.438
Stall AOA	12.5 º	15 º
Cd @ 0 AOA	0.00765	0.014
Slope of the lift curve	0.0638 per deg	0.0632

Weight estimation

For the weight estimation, the initial weight ratios are obtained from the first aircraft results, as shown in Table 5. In total, the aircraft weight is divided into structural weight, battery weight, payload, avionic weight and propulsion weight. The avionics and propulsion system weight are considered electronic weight. The motor, propellers and Electronic Speed Controller (ESC) are considered in the propulsion weight.

Table 5: Used initial weight ratios.

	Measured after manufacturing
Structural weight ratio	0.465
Electronic weight ratio	0.142

However, some of the electronics of the aircraft are already known and are listed in Table 6 and in total 0.85 kg. However, considering the additional avionics required, a total weight of 2kg is reserved for avionics.

Table 6: Avionic weights.

	Weight (kg)
UAV RFD 868ux	0.05
Herelink AUM	0.12
Antenna	0.01
NAV lights LED	0.02
Cables	0.05
Pixhawk Cube Orange	0.18
Power Module	0.05
Switches	0.08
Nav Light	0.002
RKT GPS	0.07
Telemetry	0.1348
receiver	0.0338
Mini LiDAR	0.05
Total	**0.851**

Sizing

The same methodology of sizing the first aircraft is used with the initial values of Table 7.

Table 7: Initial parameters used for sizing.

Span	3 m
AR	12
Battery specific energy density	195 Wh/kg
Payload weight	5 kg
Power efficiency	60 %
Wing planform efficiency factor	0.8
Altitude	5000 m

After the first sizing iteration, the values of Table 8 are obtained from the sizing program. Sizing step 1 provides the parameters for choosing the wing configuration and the propulsion system. For this case, as the wing geometry is already decided, it can be used to verify whether the expected performance can be met with the chosen wing configuration. The resulting design lift coefficient for cruise and maximum speed can be used to identify the required angle of attack for cruising and maximum speed. The aerodynamic data obtained in the previous section is used to determine the angle of attack, 2 degrees for this case. It was decided to choose the wing incidence with this angle of attack.

Using the resulted power requirement (PR) values from the sizing step 1, the motor and the propeller are chosen. These values are updated in the sizing step 2, which provides the

parameters to choose a battery (battery weight and capacity). Final results are obtained by updating these parameters in the sizing process.

Table 8: Results of sizing steps.

	Sizing 1	Sizing 2	Sizing 3
Wto (kg)	25.52	24.07	23.34
Wstructural (kg)	12.76	12.04	11.67
Wpropulsion (kg)	3.83	2.42	2.42
Wbat (kg)	3.94	4.62	4.13
CL_d_cruise	0.74	0.70	0.68
CL_d_Vmax	0.30	0.28	0.27
PR_cruise (W)	634.74	595.20	576.13
PR_maxV (W)	1300.16	1275.0	1262.86
Range available (km)	150	150	198.71
Endurance available (hrs)	1.19	1.19	1.58
Maximum speed (m/s) - with 80% of propulsion power	-	-	51.26

Following this, the tail of the aircraft can be sized considering the longitudinal and lateral stability. For this application, a V-Tail configuration was chosen. The final sizing values are presented in Table 9.

Table 9: Final sizing of the second aircraft.

Span (m)	3
Chord (m)	0.25
Wto (kg)	24
Cruise speed (m/s)	35
Maximum speed (m/s)	51
Minimum speed (m/s)	24
Takeoff speed (m/s)	26.9
Wing incidence angle (deg)	2
Tail incidence angle (deg)	-4.5
Tail dihedral angle (deg)	35
Wing to tail length (m) (From a.c. to a.c.)	1.5

4.3 Design

This section presents the design of the fuselage of the aircraft. The design was carried out considering the manufacturing constraints, volume requirements, assembly, and transport requirements. The payload is considered at the centre of gravity (CG) of the aircraft to eliminate

the effect of the payload on the CG position. The CG position of the aircraft is designed to be at 25% of the wing chord.

The fuselage is designed as a composite monocoque structure with inside frames (Figure 40). The motor is connected from the front of the fuselage and the tail boom carbon tube from the back end, which is held by the last two frames, a design similar to the first aircraft. The fuselage is designed with two main openings to access the inside, where on the top opening the wing sits. The wing is connected to the fuselage through 2 carbon rods (Figure 41).

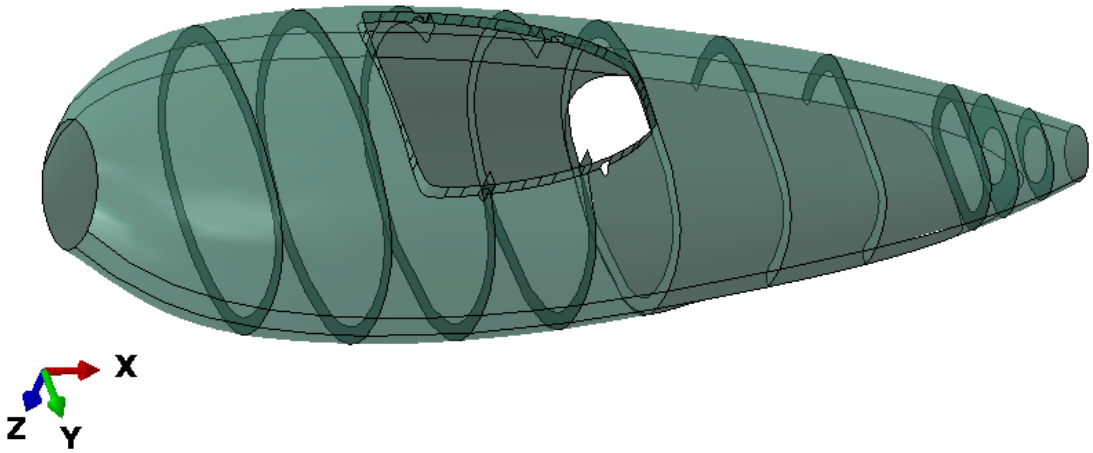

Figure 40: Fuselage design.

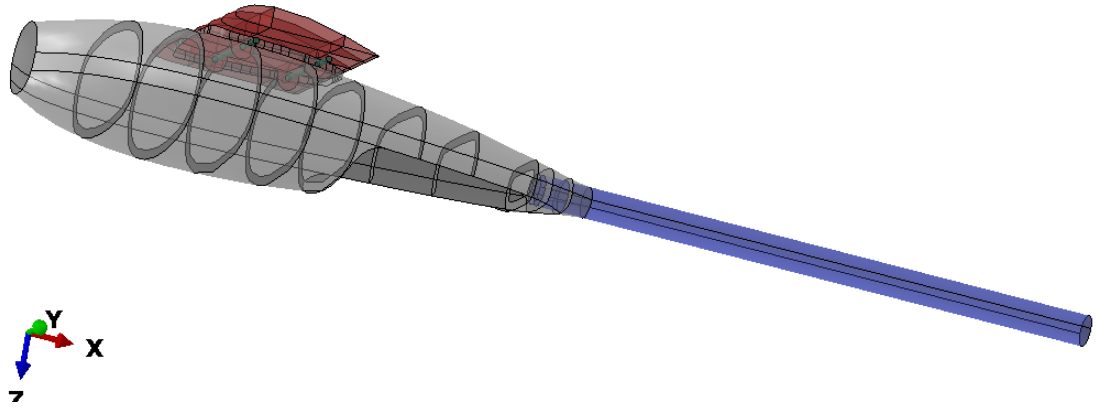

Figure 41: Fuselage design with wing and tail connections.

4.4 Load calculations

Loads applied to an aircraft are,

- Aero loads (Aerodynamic loads, Gust loads, Maneuvering loads - Lift, drag, and moments induced by airflow)
- Inertial loads
- Ground loads (applied loads while on the ground – Takeoff, landing, touchdown, breaking, ground manoeuvres, taxiing, turning)
- Propulsion loads (Loads generated by the aircraft's propulsion system - Thrust, Torque, Thrust misalignment loads)

At each point of the aircraft mission, different magnitudes of the above loads are applied. Hence, in order to structurally analyze an aircraft, there are numerous amounts of loading cases

to analyze, where each of these cases is distinct. Most of these applied loads in each case are nearly impossible to predict for a new design. Hence, the loading is predicted using statistical data from similar aircraft, wind tunnel tests and computational simulations.

Considering the mission profile and the requirements, the loads applied to this aircraft are Aerodynamic loads (manoeuvre and gust), Inertial loads, Propulsion loads and Landing loads. For the considered analysis of the fuselage, only the flight loads are evaluated. V-n diagram is created according to the EASA – CS-VLA regulations for very light Aeroplanes [45]. Aerodynamic parameters are obtained from XFLR5 simulations. A safety factor of 1.5 is considered in the applied loads to the fuselage. As the whole aircraft is mainly manufactured with composite materials, a quality factor of 1.25 is also considered in the applied load to account for manufacturing faults and material inconsistencies. Following V-n diagram is created for the sea level altitude in order to account for uncertain environmental factors.

The generated gust and manoeuvre diagrams are presented in Figure 42. However, this generated V-n diagram is different from conventional V-n diagrams, such as in Figure 43, as the cruise speed gust line goes above point A in the manoeuvring diagram. Moreover, this issue is due to the fact that the wing loading of the aircraft is low and the gust lines are steeper. The issue was handled according to the method described in reference [43], by extending the stall lines till it meets the gust lines. The combined flight envelope was obtained and presented in Figure 44.

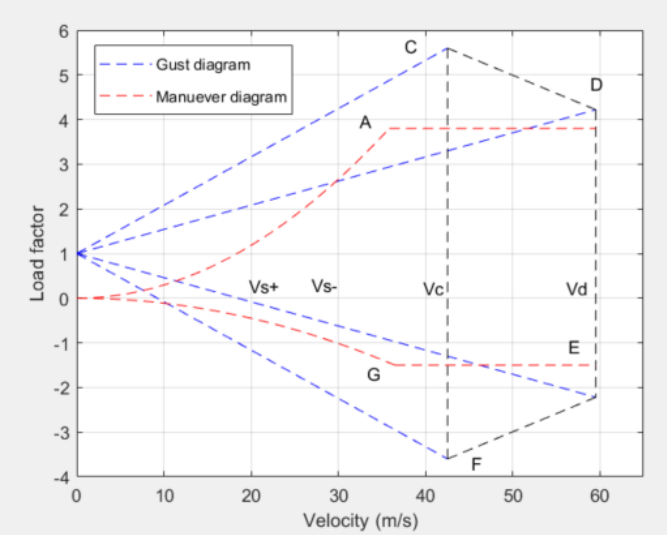

Figure 42: Gust and maneuver diagrams.

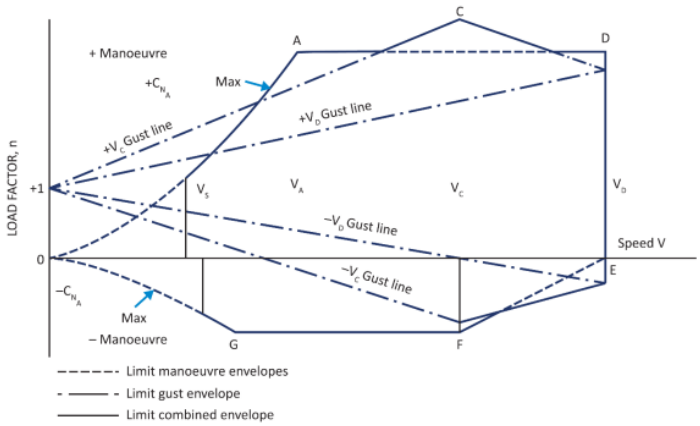

Figure 43: Conventional V-n diagram from EASA CS-VLA regulations [45].

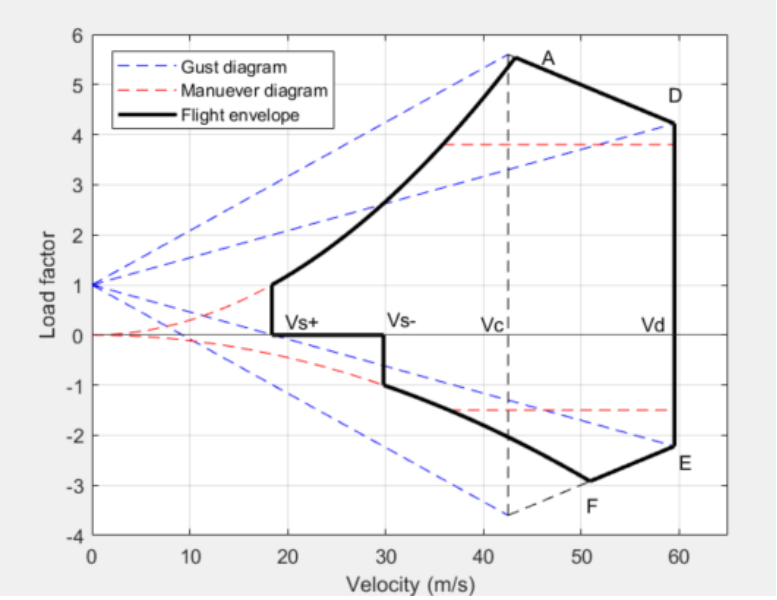

Figure 44: Combined flight diagram.

For the application of this work, one of the points from the V-n diagram is analyzed. Point A in the Figure 44, where the stall line meets the gust line is chosen to use for the structural analyses. For this load case, from the V-n diagram, the load factor of 5.5 and speed of 43 m/s are considered. Having the almost stall condition, from Table 4, the 3D stall angle of 15º is considered as the aircraft angle of attack (AOA). Additionally, considering the fixed wing incidence angle of 2º, the following references are used for calculations.

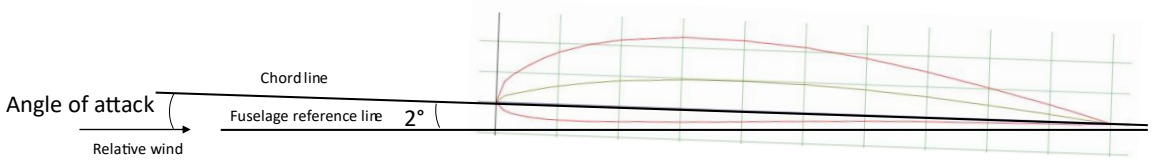

Figure 45: Leveled flight reference.

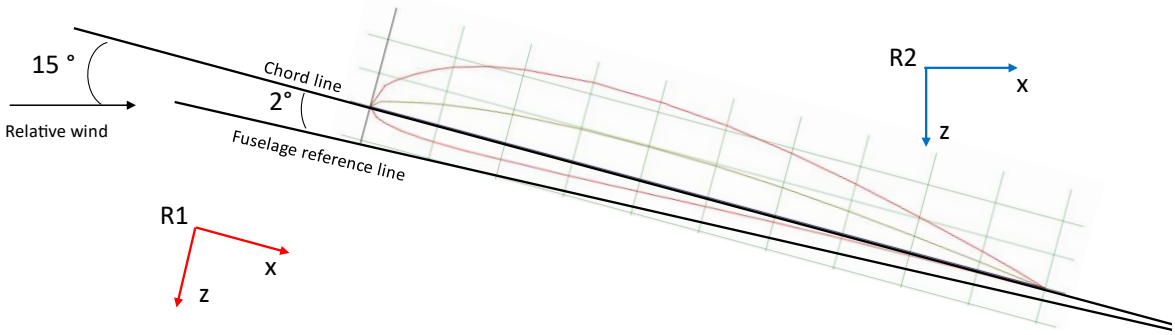

Figure 46: Aircraft configuration at the analyzed point.

As the structural calculations are conducted in Abaqus finite element software with the x-axis along the fuselage reference line, the R1 coordinate system for the calculations is used as indicated in Figure 46.

The aerodynamic loads are obtained from the XFLR5 calculations, which provide the forces with reference to the wind direction, hence the load values are in the coordinate system of R2 in Figure 46.

In this analyzed load case, the fuselage of the aircraft is subjected to wing-fuselage connection forces, tail loads, inertial loads, and propulsion loads. When modelling the fuselage, a portion of the wing is also modelled, and equivalent wing loads are applied. Wing loads are calculated using the aerodynamic loads applied to the wing obtained from XFLR5 simulations. The applied lift, drag and pitching moment are obtained from the XFLR5 simulations in the coordinate system of R2 (Table 10 and Figure 47).

Table 10: Obtained aerodynamic loads from XFLR5 simulations in R2 coordinate system.

R2 coordinate system	Values for one side of wing
Fx (Drag)	20.22 N
Fz (Lift)	- 648.77 N
My (Pitching moment)	3871.2 Nmm

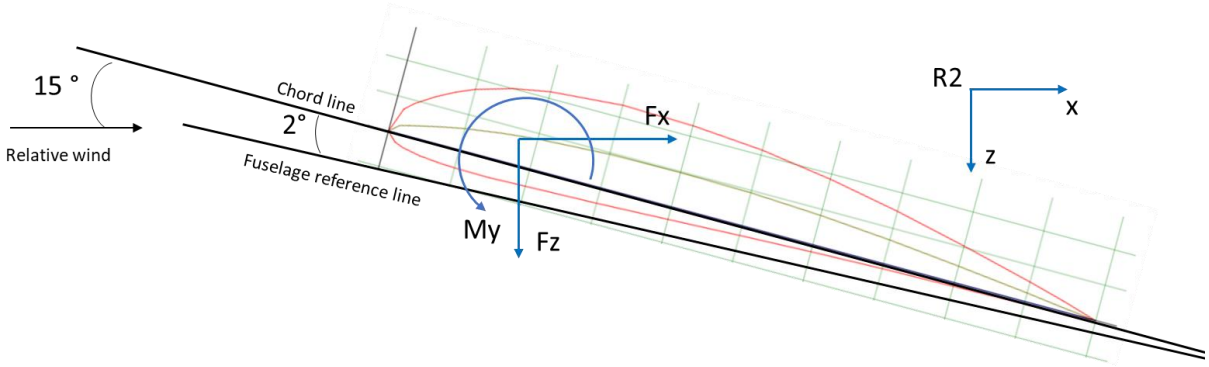

Figure 47: Aerodynamic loads from XFLR5 in R2 coordinate system.

The equivalent loads are projected on to the R1 coordinate system to apply on the FEM as presented in the following Figure 48.

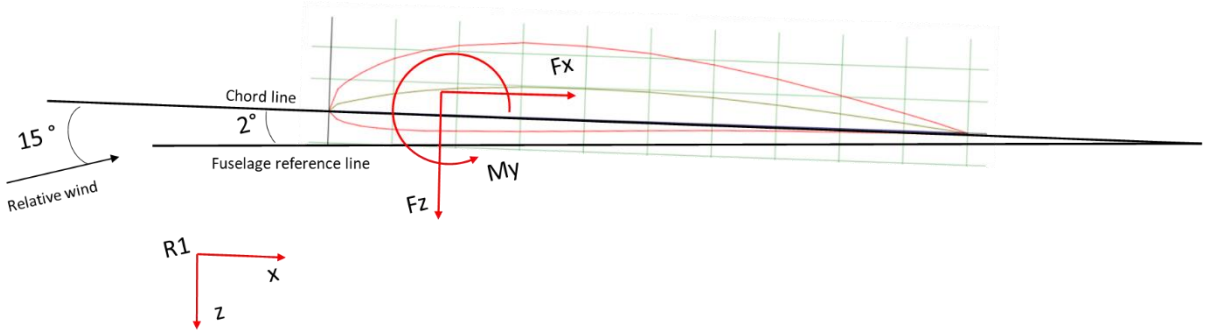

Figure 48: Equivalent aerodynamic loads on FEM with R1 coordinate system.

To analyze the centre region of the fuselage, a part of the wing is modelled to add the boundary conditions and loadings away from the analyzed region. The equivalent loads to model are calculated as follows.

Three ribs are modelled on each side of the wing. The lift is assumed uniformly distributed over the wingspan. The applied force Fz and the moment Mx is calculated using Equation 41 and Equation 42 considering Figure 49, where L_{R1} is the lift obtained in the coordinate system R1.

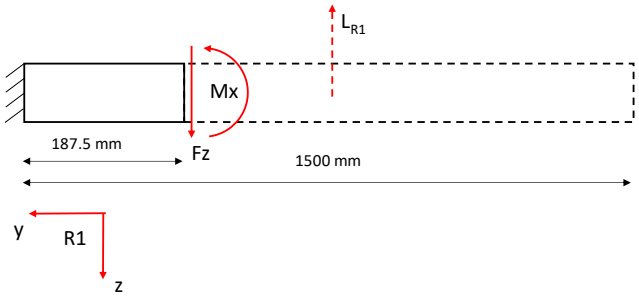

Figure 49: Applied force and moment calculation on the modelled wing section.

$$Fz = -L_{R1} \tag{41}$$

$$Mx - Fz * 187.5 = L_{R1} * \frac{1500}{2} \tag{42}$$

The same calculations are considered for the drag load applied on the modelled wing section. All the aerodynamic values applied on the modelled section of the wing according to the R1 coordinate system and considering a safety factor of 1.5 and a quality factor of 1.25 is indicated in Table 11.

Table 11: Aerodynamic loads converted to R1 coordinate system.

R1 coordinate system	Values for one side of wing
Fx	-235.875 N
Fz	-1190.19 N
Mx	743871.4 Nmm
My	7258.506 Nmm
Mz	-147422 Nmm

Inertial loads applied to the aircraft are the weight of the aircraft, considering the vertical load factor and the horizontal lead factor. The vertical load factor is obtained from the V-n diagram relative to the analyzed point A, which is 5.5, applied on the positive z direction of the R2 coordinate system. The horizontal lead factor (along the x-axis) according to the R2 coordinate system (Figure 47) can be calculated with the following Equation 43 and Equation 44. It should be taken into account that the thrust is applied along the fuselage reference line. The horizontal lead factor of 0.23 was obtained.

$$T * cos(13°) - Fx = \frac{W}{g} * a_x \tag{43}$$

$$n_x = \frac{T * cos(13°) - Fx}{W} \tag{44}$$

where,

T – Motor thrust

W – Weight

a_x – Acceleration in x direction

n_x – Lead factor in x direction

The calculated inertial loads converted to the R1 coordinates system are presented in Table 12

Table 12: Applied inertial loads in R1 coordinates system.

R1 coordinate system	Inertial loads
Fx	527.265 N
Fz	2283.835 N

Tail loads are calculated considering the longitudinal stability of the aircraft with the Equation 45 according to Figure 50. Then converted to the R1 reference system, the results in Table 13.

were obtained, safety factor and the quality factor already applied. Considering that there are no lateral loads present in inertial loads or in wing loads and for symmetrically distributed tail lift in both tails which cancels out the lateral component of the total lift on a V-tail configuration, the tail loads are only present in x and z directions.

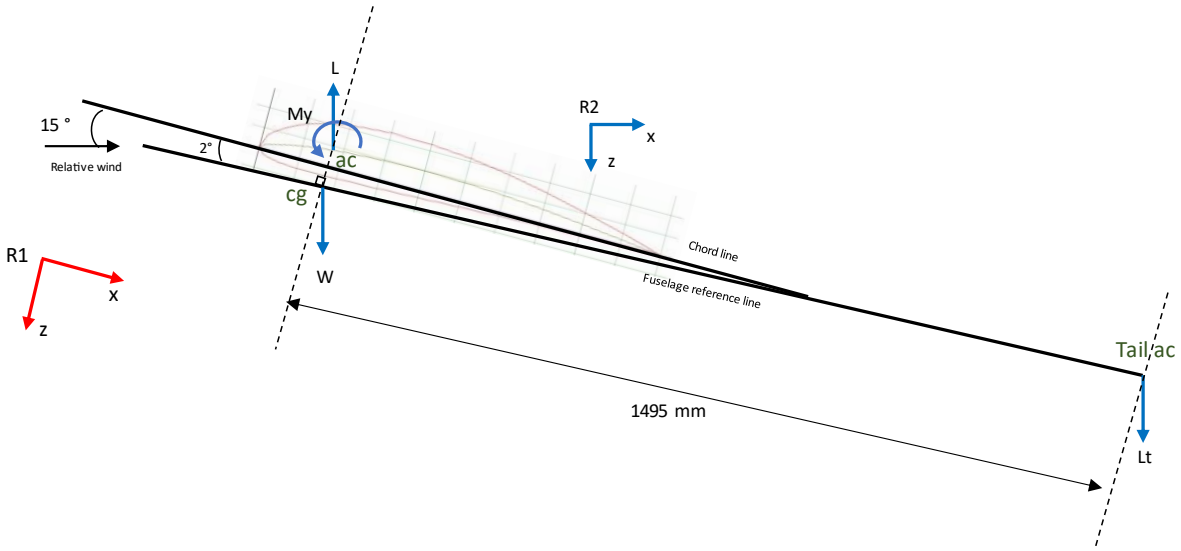

Figure 50: Longitudinal stability of the aircraft in R2 coordinate system.

$$M_y + L * \Delta(x_{ac} - x_{cg}) - L_t * \Delta(x_{ac_{tail}} - x_{cg}) = 0 \qquad (45)$$

where,

M_y – Wing pitching moment

L – Wing lift

x_{ac} – Wing aerodynamic centre

x_{cg} – Aircraft centre of gravity

L_t – Tail lift

$x_{ac_{tail}}$ – Tail aerodynamic centre

Table 13: Tail loads in R1 coordinate system.

R1 coordinate system	Tail loads
Fx	12.575 N
Fz	54.468 N

5 Optimization algorithm for composite structures

This chapter explains the development of the general optimization tool to optimize the number of layers and orientation of any composite structure while minimizing the weight. The model of the structure is constructed in Abaqus CAE using python script. The algorithm is later used in an active optimization of the fuselage of the Medical UAV designed in the previous chapters.

5.1 Overview

The developed optimization tool optimizes the finite element model which is created in Abaqus using Genetic Algorithm (GA). GA is programmed in python which connects to the Abaqus through python scripting. The program can be consulted in Appendix D.

The whole program can be divided into 3 main parts:

- Initial parameters
- Abaqus model
- GA

The model geometric parameters, material data, applied loads, constraints and GA parameters have to be defined in the initial parameters. Then the Abaqus model is created using python scripting or generated using Abaqus interface and then import the input file to the script. The created program can optimize each section of the model, while considering the effect of adjacent section layup. The GA iterates while simulating each individual in Abaqus until the stopping criteria is met. Adapted methods for saving computational expenses are introduced to the program.

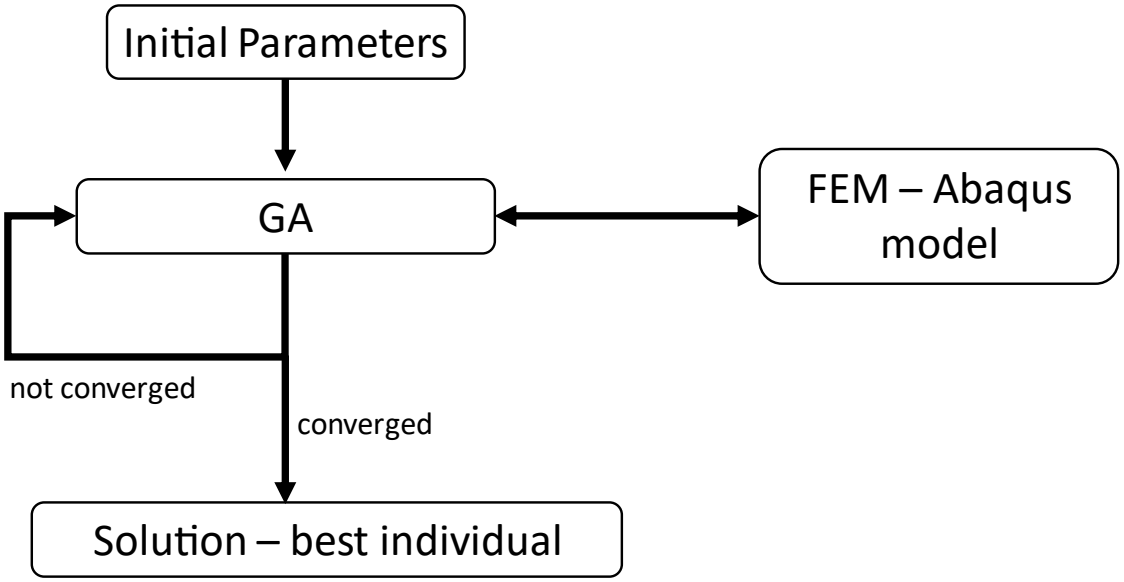

Figure 51: Schematic of the optimization tool.

5.2 Genetic Algorithm

The objective is to develop a general GA optimization program that can be used in any composite structure. This created version takes into account the failure index of the composites to size the sections. The Figure 52 present a schematic of the developed genetic algorithm, which can be described in following subtopics.

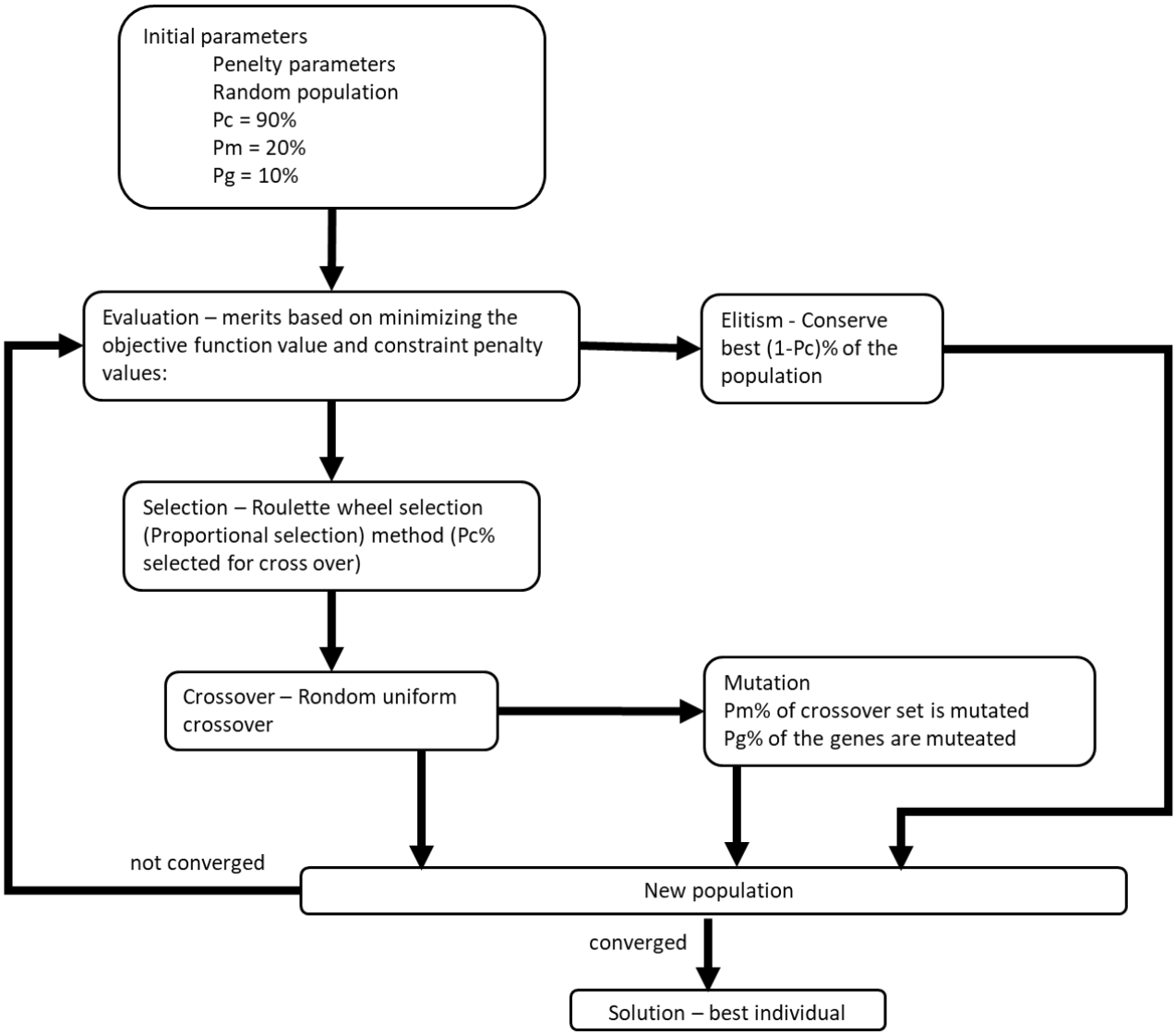

Figure 52: Schematics of developed genetic algorithm process.

Problem definition

The created program considers a single objective optimization of the composite structures, which aims to minimize the objective function. Hence, geometry and material properties are fixed as initial parameters. The problem can be defined as,

$$minimize\ f(\boldsymbol{x}), \qquad \boldsymbol{x} \in \mathfrak{R}^n \tag{46}$$

Where $\boldsymbol{x}$ is the defined variable and $f(\boldsymbol{x})$ is the objective function.

Design variables

The total structure is divided into sections as desired. Design variables are defined for each section. In order to optimize both the number of layers as well as the ply orientation, each section of the structure has 3 design variables. These 3 variables account for the number of layers in each ply orientation in each section. In this developed program only 3 main ply orientations are considered (0º, 90º, ±45º). The plus and minus 45º shares the same number of layers. The order of the layup and the symmetrical layup option can be defined in the initial parameters. This program allows to add any desired ply orientations to the problem.

$$\boldsymbol{x} = x_{11}, x_{12}, x_{13}, x_{21}, \ldots\ldots\ldots\ldots, x_{ij}, \ldots\ldots\ldots\ldots \quad (47)$$

Where *i = 1, 2, 3, ... n* is the number of sections and *j = 1, 2, 3* is the ply orientations as defined in the initial parameters.

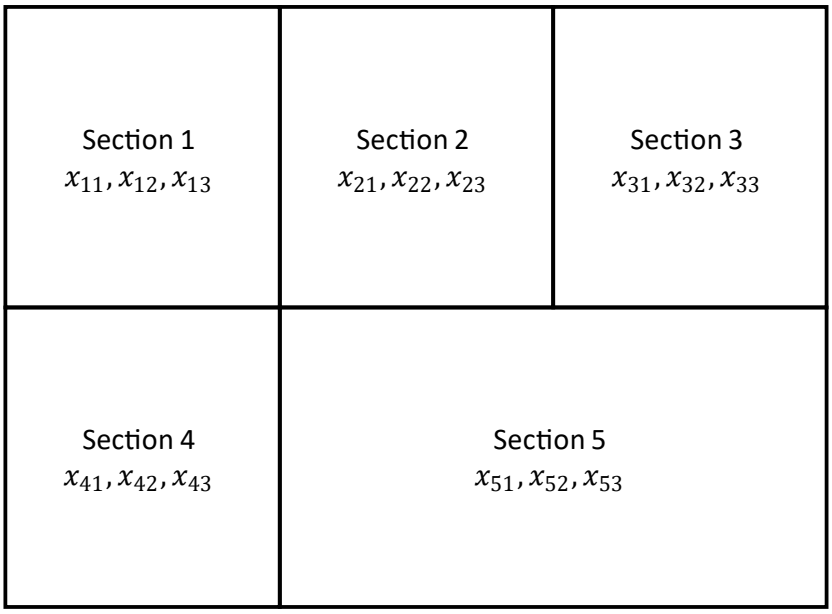

Figure 53: Representation of design variables for 5 section problem.

The design variables range from lower boundary to the upper boundary given as the initial parameters. In this program, the variables are coded as binary digits. In default 4 bits are used for each variable in the variable array.

Objective function

Structural mass is defined as the objective function which is the sum of the mass in each section considered.

$$f(\boldsymbol{x}) = \sum_{i=1}^{n} A_i * \rho * \sum_{j=1,2,3} x_{ij} \quad , \quad i = 1, 2, 3, \ldots\ldots n \quad (48)$$

Where, *i = 1, 2, 3, ... n* is the number of sections and *j = 1, 2, 3* is the ply orientations. A_i is the surface area of the i^{th} section, ρ is the aerial density of the used carbon sheets, and x_{ij} is the number of layers of j^{th} orientation in the i^{th} section.

Fitness function

The fitness of each individual is calculated using the following fitness function,

$$e(\boldsymbol{x}) = -f(\boldsymbol{x}) + \lambda(k) * \sum_{j=1}^{m} u_j(\boldsymbol{x}) \quad (49)$$

Where, m is the total number of constraints, λ is the penalty coefficient defined in initial data and u_j is the penalty violation parameter calculated using constraints.

Constraints

Inequality and equality can be written as follow,

$$g_i(\boldsymbol{x}) \leq 0 \quad (50)$$

$$h_i(\boldsymbol{x}) = 0 \quad (51)$$

Where ***g(x)*** and ***h(x)*** are inequality and equality constrain. As with many other GA methodologies, an exterior penalty function is used for the penalization of the unfeasible solutions, which depends on the distance from the solution boundary.

The used penalty violation parameter u_j can be defined as follows,

$$u_j(\boldsymbol{x}) = \begin{cases} max[0, g_j(\boldsymbol{x})] \\ |h_j(\boldsymbol{x})| \end{cases} \quad (52)$$

The following constraints are defined for the analyzed application of this work.

Upper (***ub***) and lower boundary (***lb***) are defined for each section in the initial parameters.

The following constraints are considered in this program.

1. The number of layers in each ply orientation is higher than the lowest number of layers (Lower boundary for each variable)

$$g_1(x_{ij}) = lb_i - x_{ij} \quad (53)$$

2. The number of layers in each ply orientation is lower than the highest number of layers (Higher boundary for each variable)

$$g_2(x_{ij}) = x_{ij} - ub_i \quad (54)$$

3. Each section should have at least one layer.

$$g_3(\boldsymbol{x}_i) = 1 - \sum_{j=1}^{3} x_{ij} \quad (55)$$

Where $\boldsymbol{x}_i$ is the number of plies in section *i*.

4. The structure shouldn't break (Failure Index < 1)

$$g_4(y_{ij}) = y_{ij} - 1 \quad (56)$$

Where y_{ij} is the failure index of ply j in section i. Here the failure index is obtained from the Abaqus model. Additionally, custom constraints can be easily added to the program by introducing them as equations.

Selection

The roulette selection technique also defined as fitness proportionate selection is used to select individuals from the population for the crossover. This selection technique provides the opportunity to select individuals proportional to their fitness value. Hence the genes of individuals with better fitness have more probability to pass over to the next generation. The selection process can be expressed as follows. As in Equation 57, take the sum of all the individuals in the population. Then Calculate the proportion of each induvial in the population as in Equation 58. Calculate the cumulative probability of each individual in the population, Equation 59. Generate a random number between 0 and 1. Select the individual k whose cumulative probability C(i) is the smallest value greater than the random number.

$$S = \sum_{k=1}^{n} e_k(\boldsymbol{x}) \tag{57}$$

$$P_k = \frac{e_k(\boldsymbol{x})}{S} \tag{58}$$

$$C_k = \sum_{j=1}^{k} P_j \tag{59}$$

Where, n is the population size, S is the total fitness of the population, P_k is the proportion of k^{th} individual in the population and C_k is the cumulative sum of the k^{th} individual in the population.

The selection process can be presented as following Figure 54. The pie chart represents the proportion of the population, and the straight arrows represent the chosen individual when the wheel is rotated. The selection process selects N individuals according to the given initial value of Pc, which is the percentage of the population chosen for crossover (N = n*Pc). This selected set of individuals is referred to as the ‘selected individual pool’.

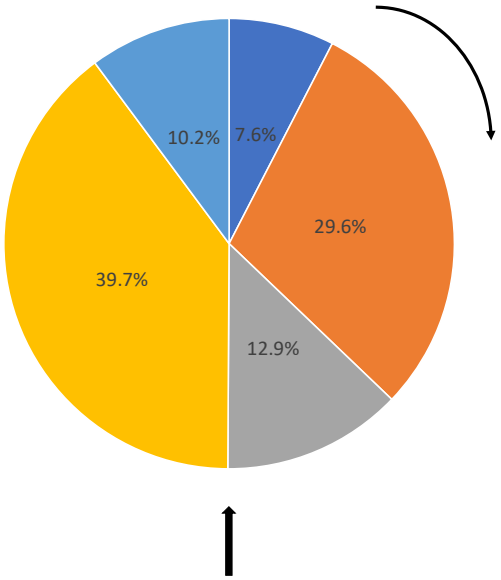

Figure 54: Representation of the Roulette selection method.

Crossover

The above selected N individuals are subjected to crossover or preservation and added to the new population. The probability of preserving the individual or mating is determined with the percentage given as initial data, which is normally kept at 50%.

Multi point uniform method is used as the crossover technique. Which creates two individuals by taking two parents randomly from the selected individual pool. The new two individuals are created by taking genes from each parent. The gene selection is defined using a random binary array. If the random binary digit is 0, for that position of the chromosome, the gene of child 1 is selected from parent 1 and for child 2 from parent 2. If the random digit is 1, the gene is selected from the opposite parent. This process allows to create 2 distinct but related children from the same parents. The process is featured in the following figure.

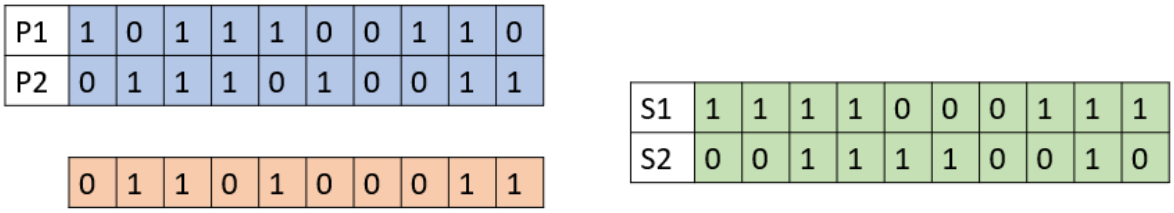

Figure 55: Representation of the multi point crossover method.

Mutation

Selected proportions of the population are mutated according to the indicated initial parameters. The individual to mutate as well as the number of genes to mutate are generated randomly. The mutation simply inverts the selected genes in the individual.

Elitism

Elitism is a strategy that aims to preserve the best individuals from one generation to the next, ensuring their survival and potential propagation. It involves selecting a certain number of the fittest individuals from the current population and directly transferring them to the next generation without any changes. This approach helps maintain the best solutions found so far,

preventing their loss due to the randomness of the selection and reproduction processes. The main purpose of elitism is to prevent the premature convergence of the GA and improve its convergence speed and solution quality. By preserving the best individuals, elitism ensures that valuable genetic information is not lost and can be further refined and explored in subsequent generations. This allows the GA to focus on refining the already high-quality solutions while still exploring new regions of the search space.

This strategy is implanted on this developed algorithm with preserving the best 10 individuals in each generation.

Initial parameters

The following set of parameters is defined as initial data. The default values are indicated here. The values can be changed as desired with the application.

$ub - Upper\ boundary$

$lb - Lower\ boundary$

$tol - maximum\ tolerance$

$maxiter - Maximum\ number\ of\ iterations$

$n - Population\ size$

$l - numbe\ rof\ bits\ per\ variable$

$Pc - \ Fraction\ of\ the\ population\ selected\ for\ crossover$

$Pm - \ Fraction\ of\ the\ population\ selected\ for\ mutation$

$Pg - \ Fraction\ of\ the\ genes\ selected\ for\ mutation$

$\lambda - \ penalty\ coefficient$

5.3 Finite Element Model

As described in the overview, each individual generated in GA is modelled in the Abaqus model and results are exported into GA for evaluation. The whole Abaqus model can be described in 3 sections,

- Initial model
- Update layups
- Post-Processing

In order to avoid simulating the same order of layups again and again in Abaqus, the Python integrated database 'MySQL' is used to store each simulated layup and results.

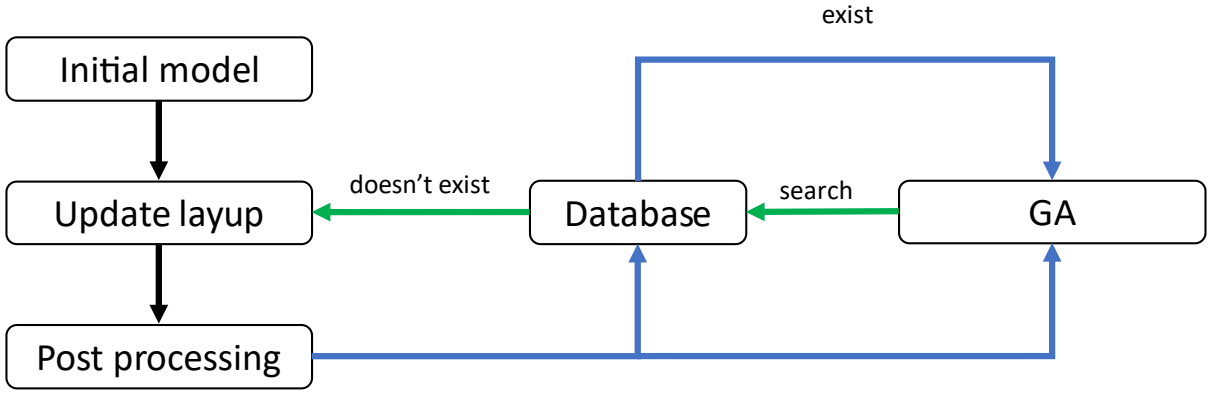

Figure 56: Schematic of the finite element model with GA.

Green lines represent the flow of layups (design variables) and blue lines present the flow of results of layups. The initial model is only created once during the start of the optimization process. Later only the layups are updated in Abaqus.

Initial model

The initial model is independent of the GA. Here the geometric model in Abaqus is created where parts, materials, properties, mesh, loads, interactions, field output requests and job are created. Python scripting implemented in Abaqus is used to generate above mentioned Abaqus model.

A cylinder with two frames is used as an example is presented below (Figure 57). The part is divided into 5 sections for optimization. Geometric parameters such as radius, length and frame lengths are defined as initial parameters. Considering a symmetric layup option for the given initial layup of $[\pm 45°, 90°, 0°]$ following composite layups are created in Abaqus. One composite layup was created for each section.

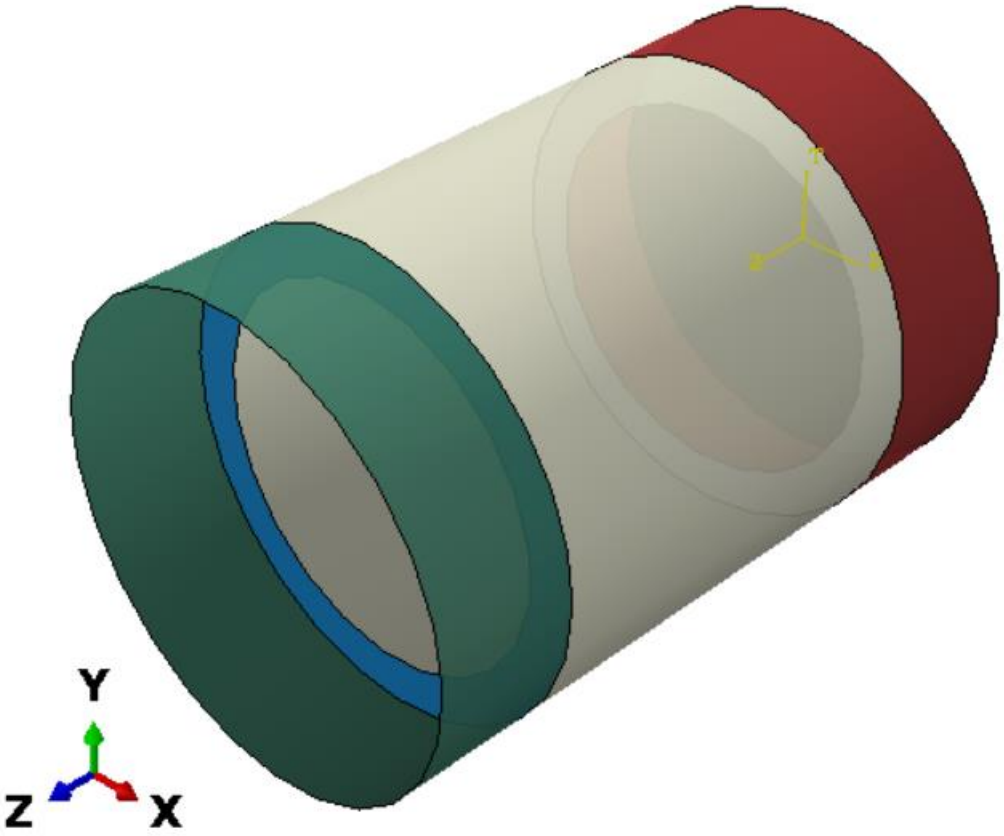

Figure 57: Created finite element model for the cylinder (Each colour represents a section).

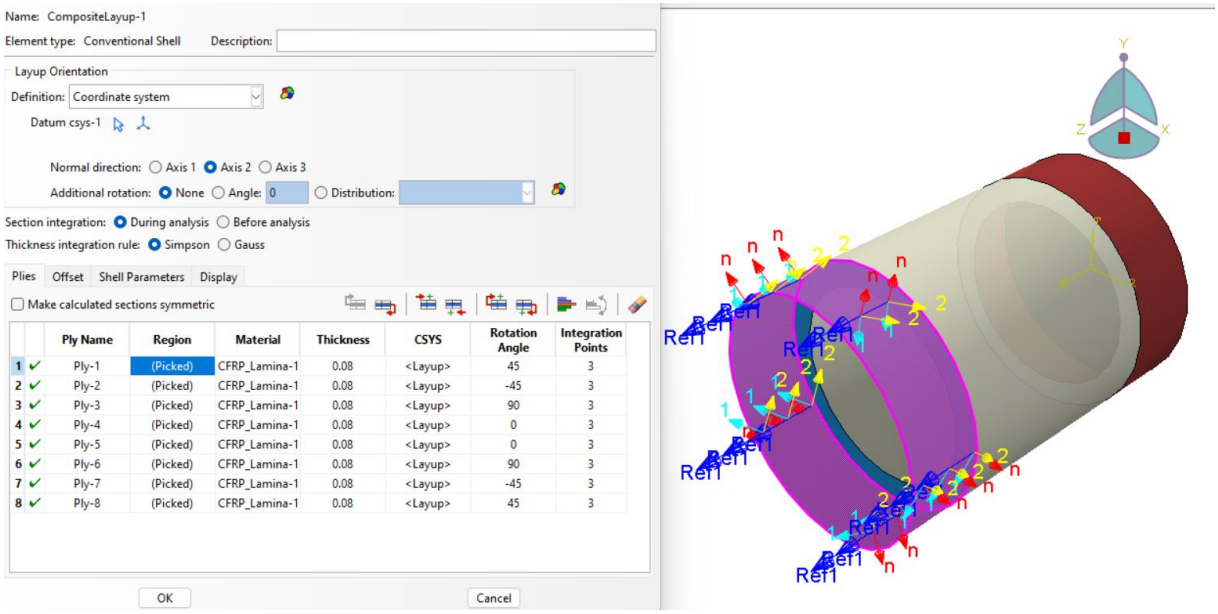

Figure 58: Fixed ply layers in the composite layup for section 1.

In order to optimize both the number of layers as well as the orientation, in Abaqus a fixed layup is created where the thickness of each orientation is updated according to the variables from GA (Figure 58). The design variable in GA is the number of layers, hence, in Abaqus, the variables are multiplied by the layer thickness of a single carbon sheet which is defined initially.

Updating layups

This section describes the connection of the GA with the Abaqus model. The model takes the layup as input from GA (through the database). The given input is the number of layers for each orientation for each section (3 variables for each section). Based on the input, multiplied by the layer thickness, each composite layup for each section is updated with the new values. Hence, in Abaqus only the thickness of each ply updates, keeping the iteration process efficient. Then the job is submitted for analysis.

Example for the 5 sections cylinder of earlier:

- An individual from GA: [9, 2, 14, 7, 1, 12, 6, 10, 11, 3, 5, 8, 13, 4, 15]
- Which corresponds to: [sec_1-$ply_{\pm 45}$, sec_1-ply_{90}, sec_1-ply_0, sec_2-$ply_{\pm 45}$, sec_2- ply_{90}, sec_2-ply_0 ,……., sec_5- ply_0]
- Updating the section layups accordingly and submitting the job.

Post-Processing

This section describes the process after the simulation submitted in Abaqus with the input layups from the GA for an individual. After the job is completed, in each section the maximum Tsai – Hill value in each ply is noted using a Python script. The maximum Tsai Hill value for each ply for each section is returned to the GA for evaluation.

Example for the 5 sections cylinder of earlier. The results of the cylinder are in Figure 59. For section 4, the maximum value is indicated (Figure 60).

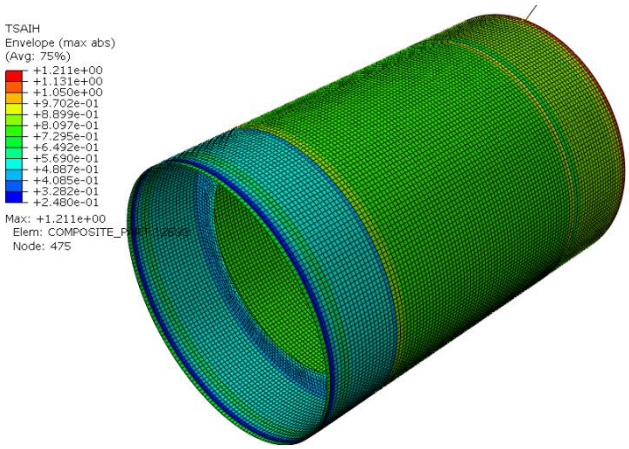

Figure 59: Resultant TSAIH values from the post-processing

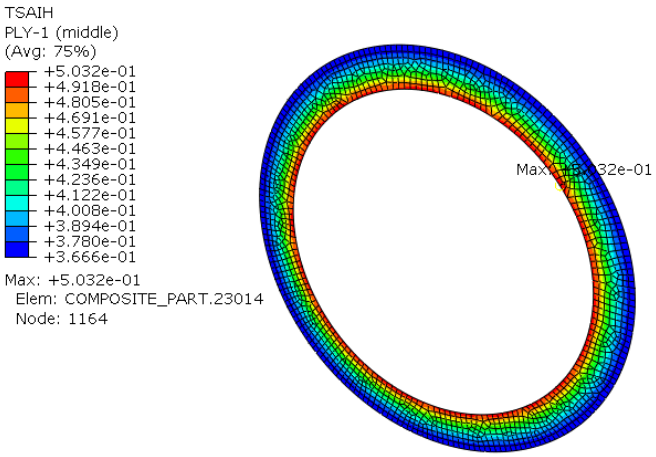

Figure 60: Maximum TSAIH value from section 4.

The Tsai Hill values of each ply then returned to GA, [0.9938, 0.5468, 1.17337, 1.3594, 0.7419, 1.6045, 0.6568, 0.4644, 0.75284, 0.4368, 0.2043, 0.5190, 0.2870, 0.1199, 0.3251].

5.4 Surrogate model

The above explained methodology is computationally expensive as in each iteration each new individual is simulated in Abaqus. For a model with more sections, the simulation in Abaqus and results extraction becomes much too expensive. In order to avoid this, this section presents the generation of a surrogate model which will numerically represent the Abaqus finite element simulation.

The surrogate model is created by simulating in Abaqus a few points calculated from the Design of Experiments (DoE) technique, and then interpolating the points with regression method to generate numerical models. Following this GA can use the surrogate model instead of simulating each new individual in Abaqus.

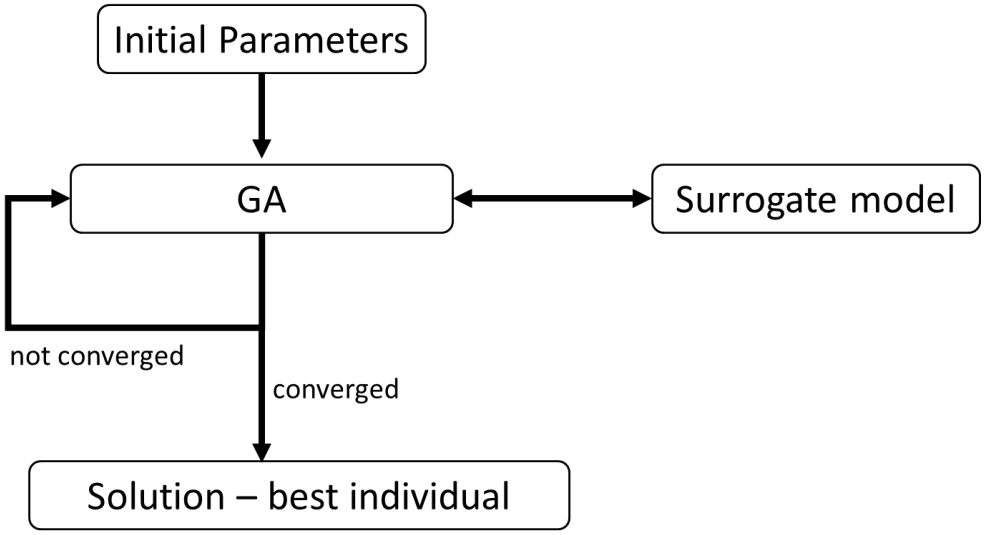

Figure 61: Schematic of the surrogate model with GA.

The developed surrogate model can be described in 2 steps.

1. Abaqus simulation
2. Regression

Abaqus simulation

The selected points are simulated in Abaqus to use in the regression model. The combinations of layers to simulate are determined using DoE with the 'Latin Hypercubic method', which is implemented in Python. The number of samples should be determined using a convergence analysis of sensitivity. Factors such as interpolated values, interpolation error, regression model parameters, prediction accuracy or computational efficiency can be used for sensitivity analysis.

Regression

Using the simulated points, the regression methods can be used to interpolate the rest of the points in the range. Different types of regression methods are tested to obtain the most precise prediction possible. For this work, the Scikit-learn library that is already implemented in Python is used. The following methods of regression are tested to obtain the most suitable and computationally efficient method.

- Linear regression
- Linear regression with polynomial features
- Gaussian regression
- Linear regression with the Ridge model
- Linear regression with the Lasso model
- Linear regression with ElasticNet model

The above methods are tested along with the validation of the algorithm cases in the next chapter.

Considering that in a layup, the number of layers in adjacent plies and adjacent sections affects the analyzed ply failure index, the regression method should take this effect into account. For this reason, all the variables are considered in the regression to obtain the resultant value. Which makes this a multi-variable regression problem with more than one independent variable and one dependent variable.

For the example of 5 section cylinder presented in section 5.3, for an analyzed individual with 15 variables (5 sections x 3 plies), the Abaqus simulation provides 15 failure indexes (5 sections x 3 plies). In the regression, 15 equations are generated, each equation representing each ply in each section. To generate the equation all 15 input variables are used with one failure index as presented in Figure 62.

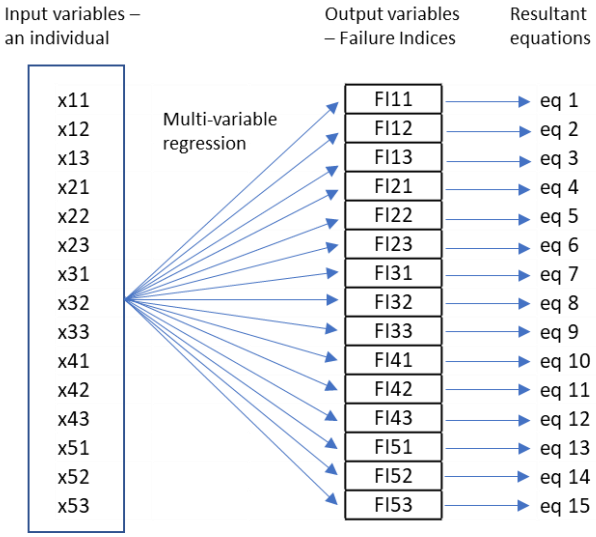

Figure 62: Multi-variable regression representation for the example of 5 section cylinder.

6 Validation of the algorithm

This section presents the validation of the algorithm presented in the last chapter. Here 4 different load cases with known solutions are tested with the GA and surrogate model. These cases are modelled as single sections for simplicity.

The following 4 load cases are analyzed:

1. Plate with tensile load
2. Plate with pure shear
3. Four-point bending
4. Cylinder with internal pressure

Following these 4 cases, the algorithm is tested with a multi section test for further validation. These test cases are also used to determine the most precise regression method for this application.

6.1 Abaqus models

Four initial Abaqus models are created for each case. The same material properties are used in all cases. The loads are applied to obtain the final answer in the middle of the range of the upper and lower boundary.

Materials

Carbon composites are used as the material. Non-crimp unidirectional carbon sheets with the following material properties are used (Table 14). The following properties are obtained considering the vacuum resin infusion manufacturing process.

Table 14: Material properties used in the Abaqus model.

	Magnitude	Units
Carbon density	1.77	g/cm^3
Carbon areal density	80	g/m^2
Fibre volume fraction	60 %	
Resin density	1.15	g/cm^3
Laminate thickness	0.08	mm
Laminate gross weight per area	114	g/m^2

Mechanical properties used in Abaqus are defined below. The unit system of MPa/mm/tone is considered for the following data.

Elastic mechanical properties with engineering constants.

E1	E2	E3	Nu12	Nu13	Nu23	G12	G13	G23
100000	10000	10000	0.34	0.34	0.34	5400	5400	3050

Figure 63: Laminate mechanical properties used in the Abaqus model.

Elastic failure stresses

Ten Stress Fiber Dir	Com Stress Fiber Dir	Ten Stress Transv Dir	Com Stress Transv Dir	Shear Strength
1400	-930	47	-130	53

Figure 64: Laminate failure stresses used in the Abaqus model.

Elastic failure strains

Ten Strain Fiber Dir	Com Strain Fiber Dir	Ten Strain Transv Dir	Com Strain Transv Dir	Shear Strain
0.025	0.01	0.002	0.018	0.03

Figure 65: Laminate failure strains used in the Abaqus model.

Models

Case 1: Plate with tensile load

A 100 x 100 mm^2 plate of shell elements with tensile load (1700 MPa) applied to one edge is created. And boundary conditions as shown in the following Figure 66 are applied to simulate a plate with tensile stress. The composite layup is defined for the plate with symmetric conditions for $[\pm 45^o, 90^o, 0^o]_s$ layup. For this case, the expected answer should be all 0^o plies for the most optimized layup. The tensile loads are selected as the answer to be [0, 0, 7] when the lower boundary is 0 and the upper boundary is 15 layers. The plate is meshed and submitted for analysis.

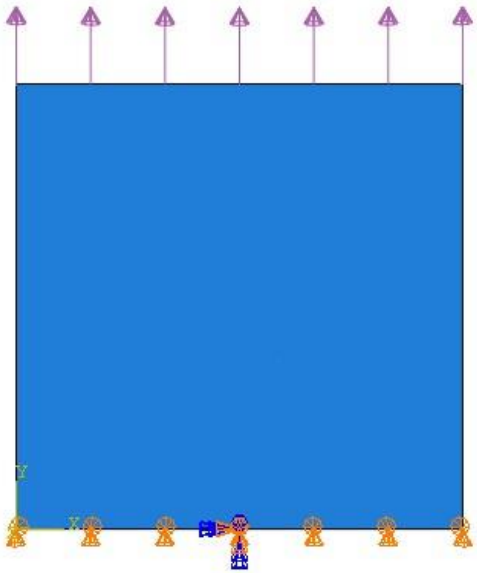

Figure 66: Case 1 - Geometry boundary conditions and loads.

Case 2: Plate with pure shear

Similar to the tensile plate, a shell element plate to simulate pure shear conditions is created with the shear loads applied and boundary conditions as presented in Figure 67. A shear load of 600 MPa is applied to each edge, which is selected in order to get the answer in the middle of the range. A laminate layup with $[\pm 45^o, 90^o, 0^o]_s$ order. The expected answer is having only $\pm 45^o$ layers. For this applied load the expected answer is [7, 0, 0]. The part is meshed and submitted for analysis.

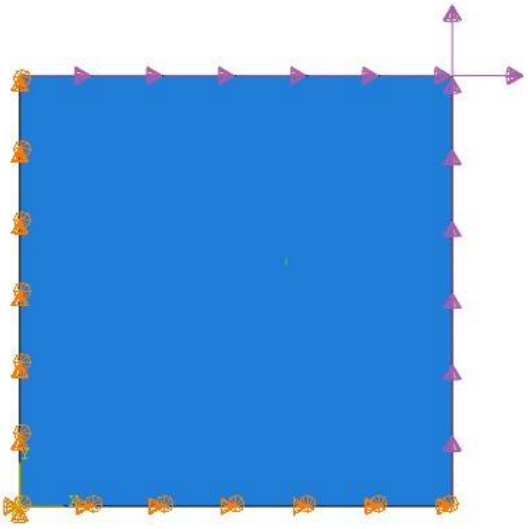

Figure 67: Case 2 - Geometry boundary conditions and loads.

Case 3: Four-point bending

The following model is generated in Abaqus to simulate a four-point bending test to a plate. The plate is generated using shell elements. Figure 68 presents the applied boundary cases as well as the loading, where the applied concentrated load is distributed to two lines beside the load by uniform constraints. The applied concentrated load is 680 MPa. The composite layup of $[0^o, 90^o, \pm 45^o]_s$ is applied to the plate. This layup order was selected as in this bending case the order of the different orientations of the ply angle also contributes to the results. Having 0^o plies on the outside resulted in the lowest number of plies. The expected answer for the following test case is all 0^o plies, [7, 0, 0]. The mesh is generated and submitted for analysis.

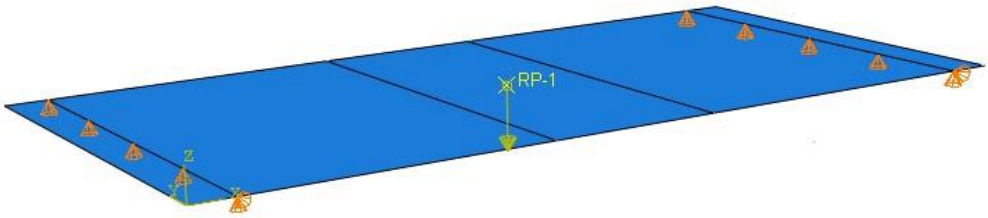

Figure 68: Case 3 - Geometry boundary conditions and loads.

Case 4: Cylinder with internal pressure

The following Figure 69 shows the model created to simulate a cylinder with applied internal pressure. The cylinder as well as the frames are modelled with shell elements. A pressure value of 7 MPa is used. The expected answer is only 90^o plies. 0^o are defined in the z-direction. A cylindrical coordinated system is used for this model. A similar layup order of $[\pm 45^o, 90^o, 0^o]_s$ is used for the layup. Hence, the response is expected to be [0, 7, 0]. A mesh is generated and submitted for analysis.

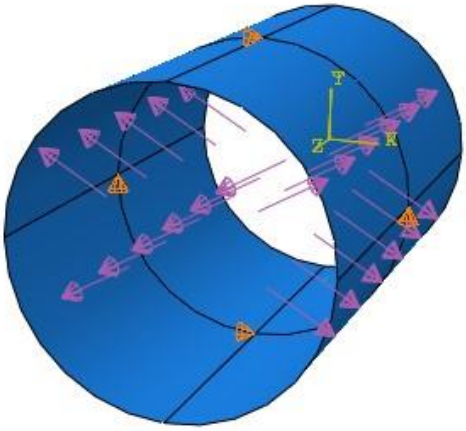

Figure 69: Case 4 - Geometry boundary conditions and loads.

6.2 Sensitivity analysis

To determine how many simulations should be conducted in Abaqus in order to generate the training points for regression, a sensitivity analysis has to be carried out. The combinations simulated in Abaqus are obtained from DoE with the Latin Hypercubic method. Six regression methods are tested in order to find the most precise and efficient considering the required computational time. Considered regression methods are: Linear regression, Linear regression with polynomial features, Gaussian regression, Ridge model, Lasso model and Elastic Net.

These test cases have 3 variables. The average mean square error of these 3 variables and the computational time for each set of samples are plotted with the number of samples for sensitivity analysis and efficiency.

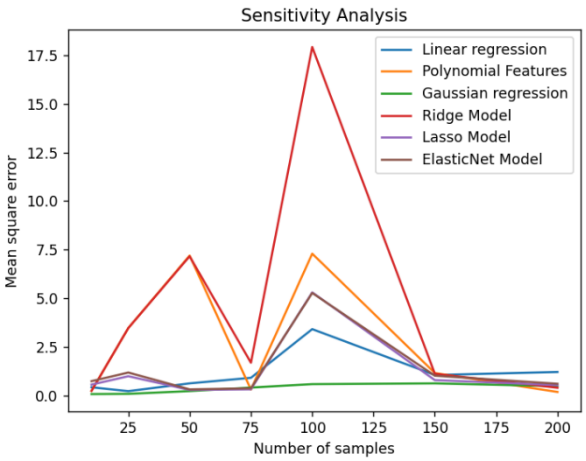

Figure 70: Sensitivity analysis - Case 1 - Tensile plate

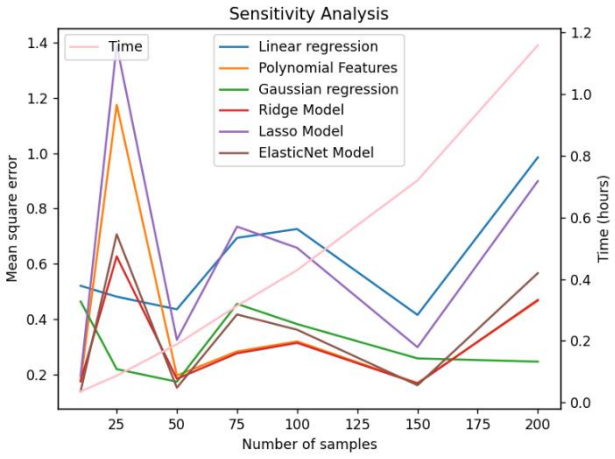

Figure 71: Sensitivity analysis - Case 2 - Pure shear

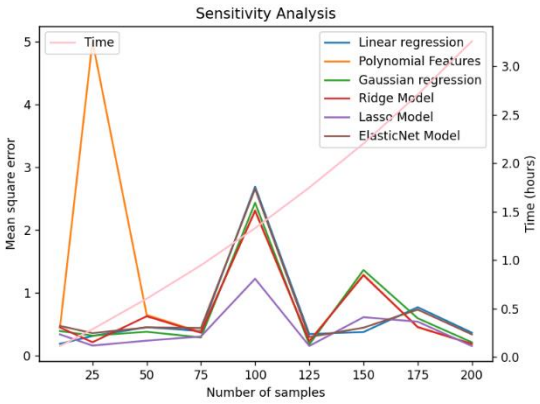

Figure 72: Sensitivity analysis - Case 3 – Four-point bending

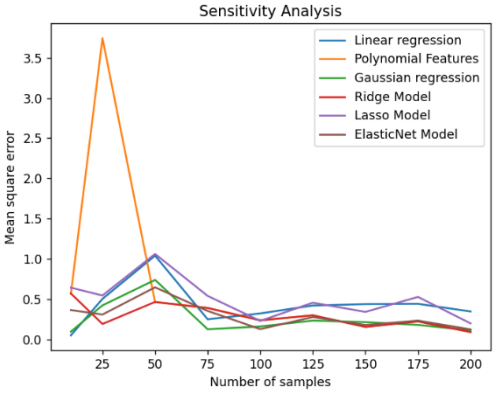

Figure 73: Sensitivity analysis - Case 4 - Cylinder

Analyzing the results, it can be seen that the number of samples, regression method and the applied load case greatly affect the precision of the results. In all cases except the case of Four Point Bending (Case 3) in Figure 72, the Gaussian regression method converges the fastest with the least variation along the number of samples when compared to other methods. Furthermore from Figure 71 and Figure 72, it can be seen that the precision comes at the expense of the computational time. However, it should be noted that most of the used regression methods have parameters that should be adjusted according to the number of samples and applications to obtain more precise results. In the above plots, the parameters are adjusted with the loads but not with the number of samples. Hence, better results might be able to obtain than plotted.

6.3 Surrogate model

Six regression methods are tested in each case to analyze the most suitable method for this application. From the sample data, 80% of data is used as training data while the other 20% is testing data. Which will be used to get the mean square error.

In order to create the surrogate model a certain number of samples are chosen for each load case and samples between 0 to 15 are generated according to the Latin Hypercube sampling method. The generated samples are simulated in Abaqus to obtain the failure index for each ply (3 variables). Using the analysis regression methods, the equations that represent the surrogate model are obtained. 200 samples are used in each case to obtain the surrogate model.

Case 1 – Plate with tensile load

The simulated 200 samples are plotted in Figure 74 with the maximum TSAIH value in the layup.

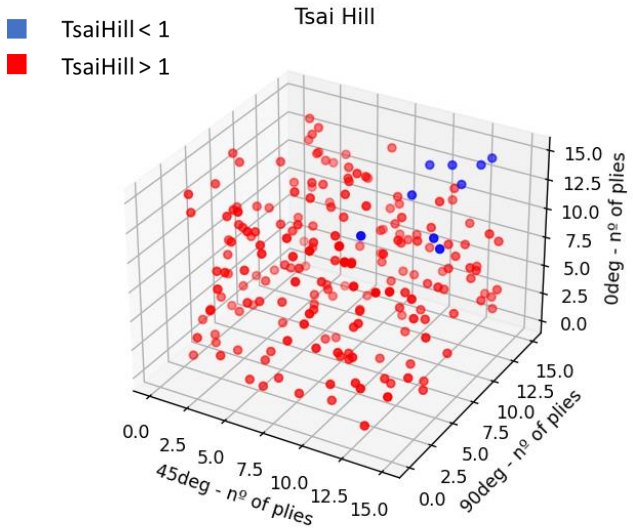

Figure 74: Case 1 - Simulated points in Abaqus, maximum TSAIH

Surrogate models are generated with all six analyzed regression models. The prediction of each surrogate model is presented in Figure 75 with the Abaqus results for the TSAIH value in each ply. Analyzing the plots, it can be seen that the polynomial and Gaussian surrogate models predict the simulated values closer.

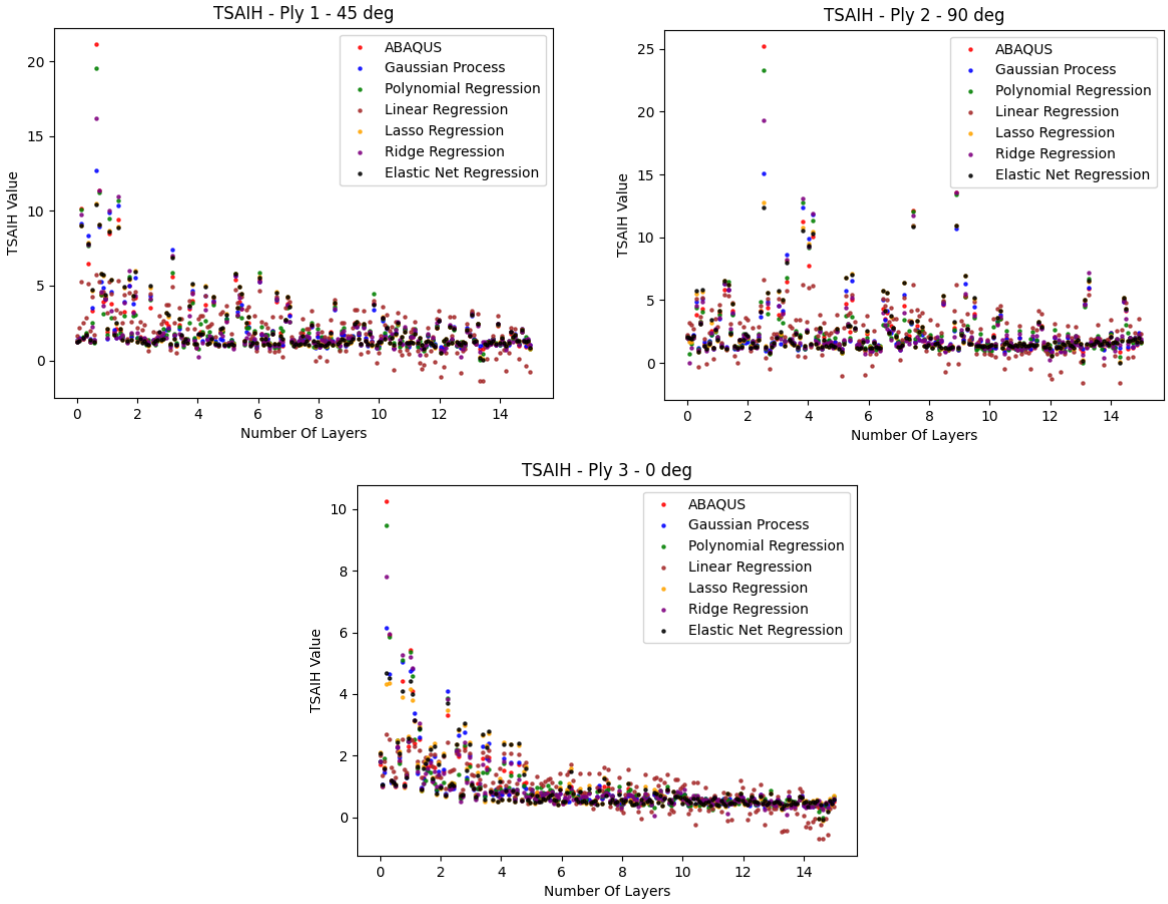

Figure 75: Case1 - Predicted TSAIH for testing samples.

Case 2 - Plate with pure shear

A training set of 200 samples are simulated in Abaqus software and the maximum TSAIH in each ply was extracted. The training set is plotted in Figure 76. Observing the plot, it is obvious the effect of the ±45º ply on the final Tsai Hill value of the ply.

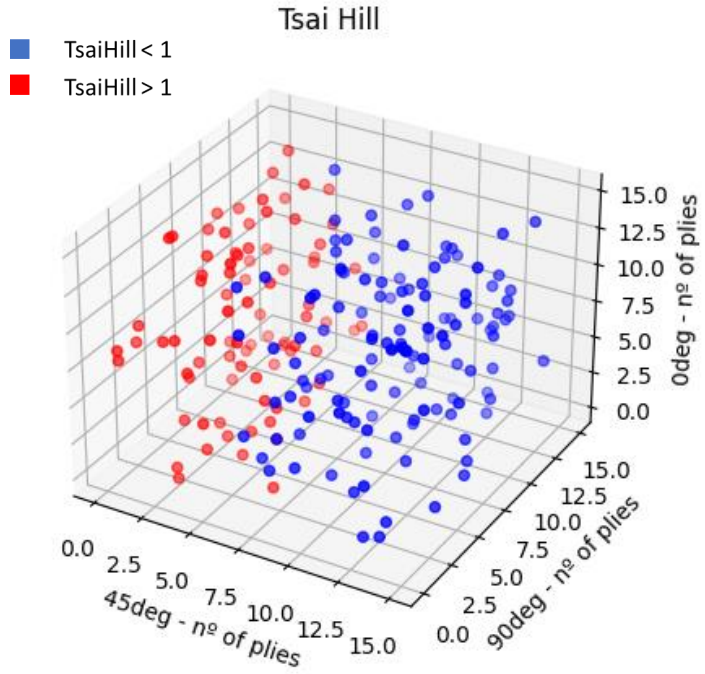

Figure 76: Case 2 - Simulated points in Abaqus, maximum TSAIH

The above plotted training samples are used to generate surrogate models. The predicted values for the testing sample set are plotted in Figure 77. It can be seen that the Gaussian model predicts the simulated values more closely.

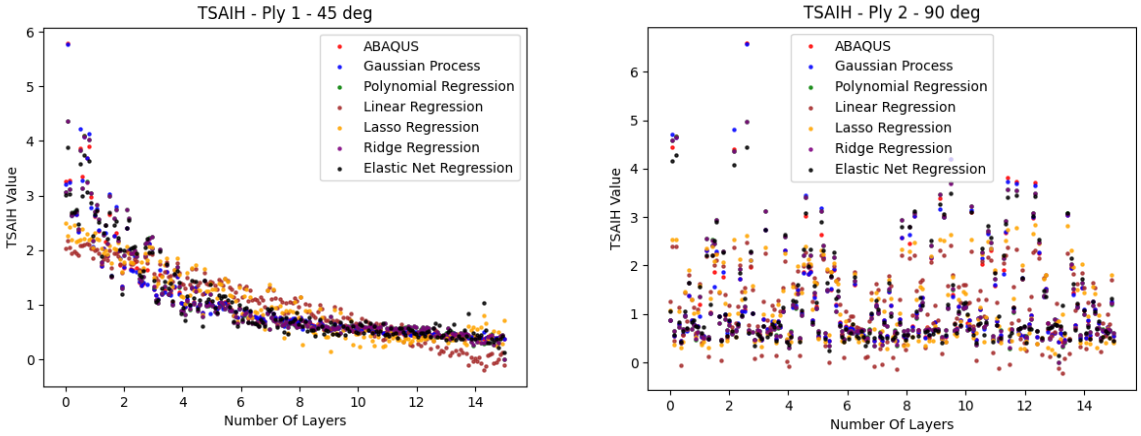

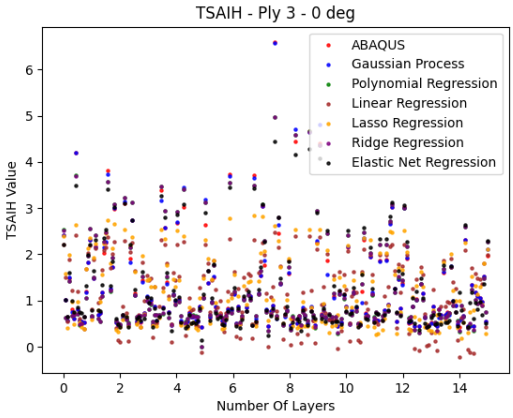

Figure 77: Case 2 - Predicted TSAIH for testing samples.

Case 3 – Four-point bending

A training set of 330 samples are simulated in Abaqus. The samples are plotted in Figure 78. It can be noticed the importance of the 0° ply to the maximum Tsai Hill value when observing the plot.

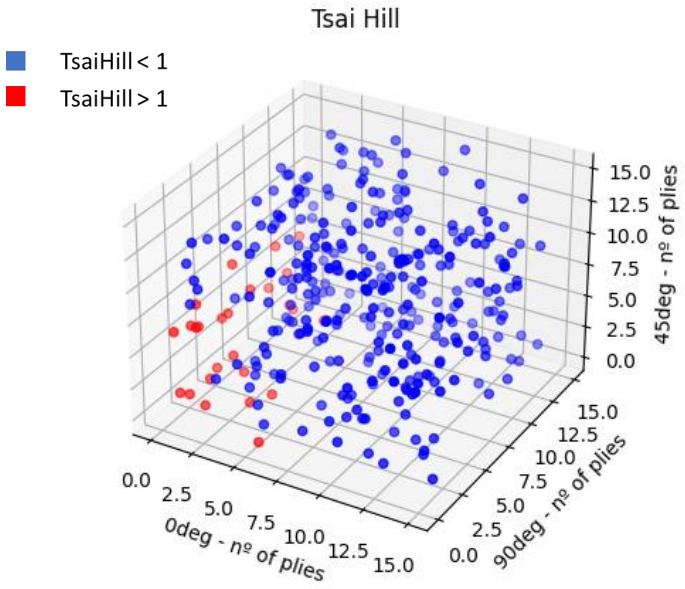

Figure 78: Case 3 - Simulated points in Abaqus, maximum TSAIH

Figure 79 present the predicted values of the surrogate models for the testing set with the simulated results. The Gaussian regression method can be identified as the close fitted surrogate model.

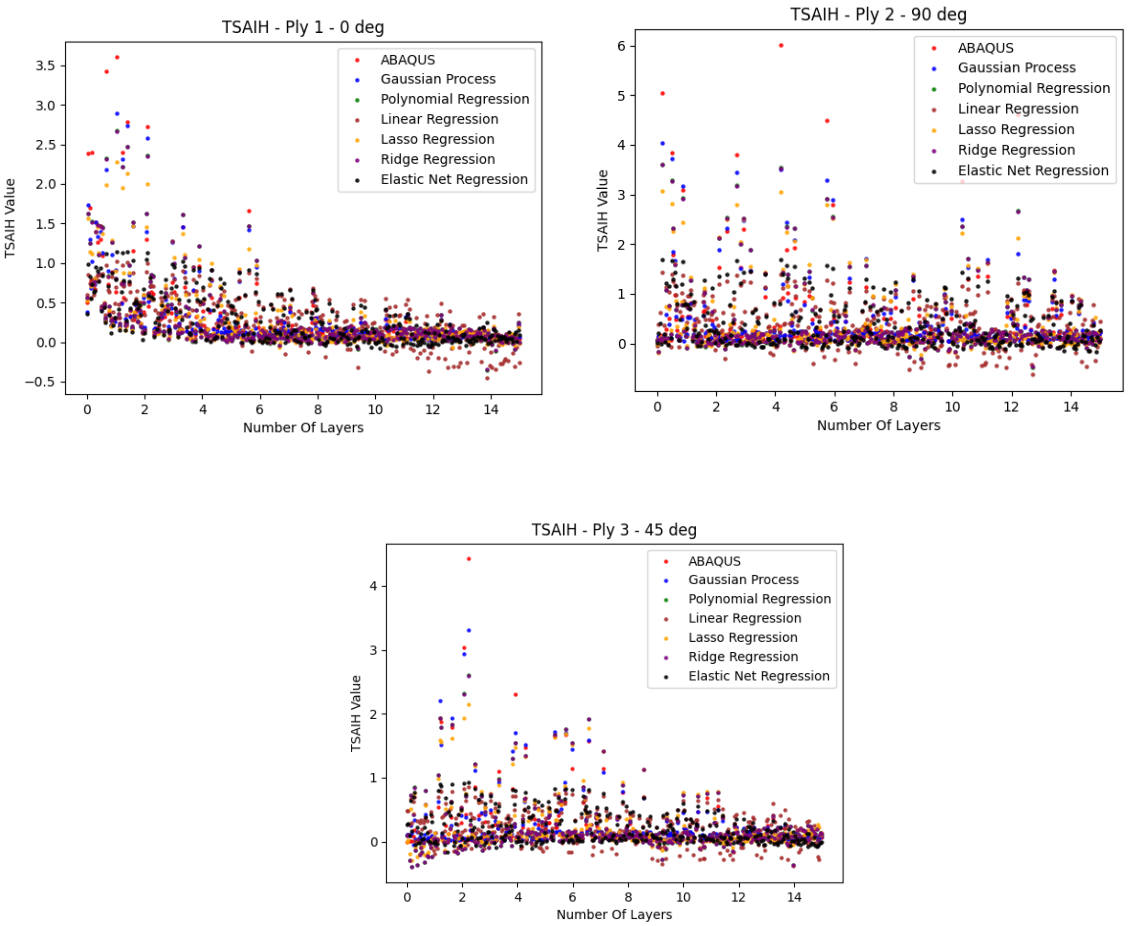

Figure 79: Case 3 - Predicted TSAIH for testing samples.

Case 4 – Cylinder with internal pressure

A set of 200 samples are simulated in Abaqus as the training data and the resultant failure indices are plotted in Figure 80.

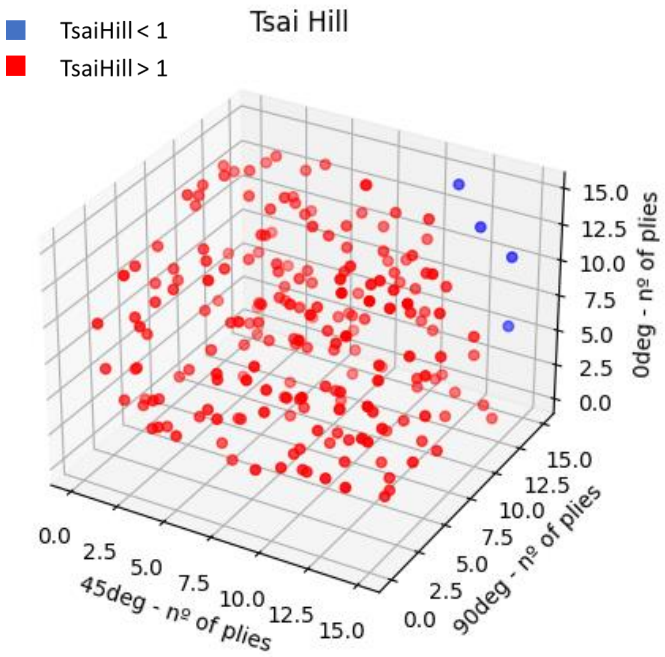

Figure 80: Case 4 - Simulated points in Abaqus, maximum TSAIH

The generated surrogate models for the simulated values are tested with the testing data set. The predicted values are plotted in Figure 81. The Gaussian and the ElsticNet can be observed to be the models closely representing simulated values.

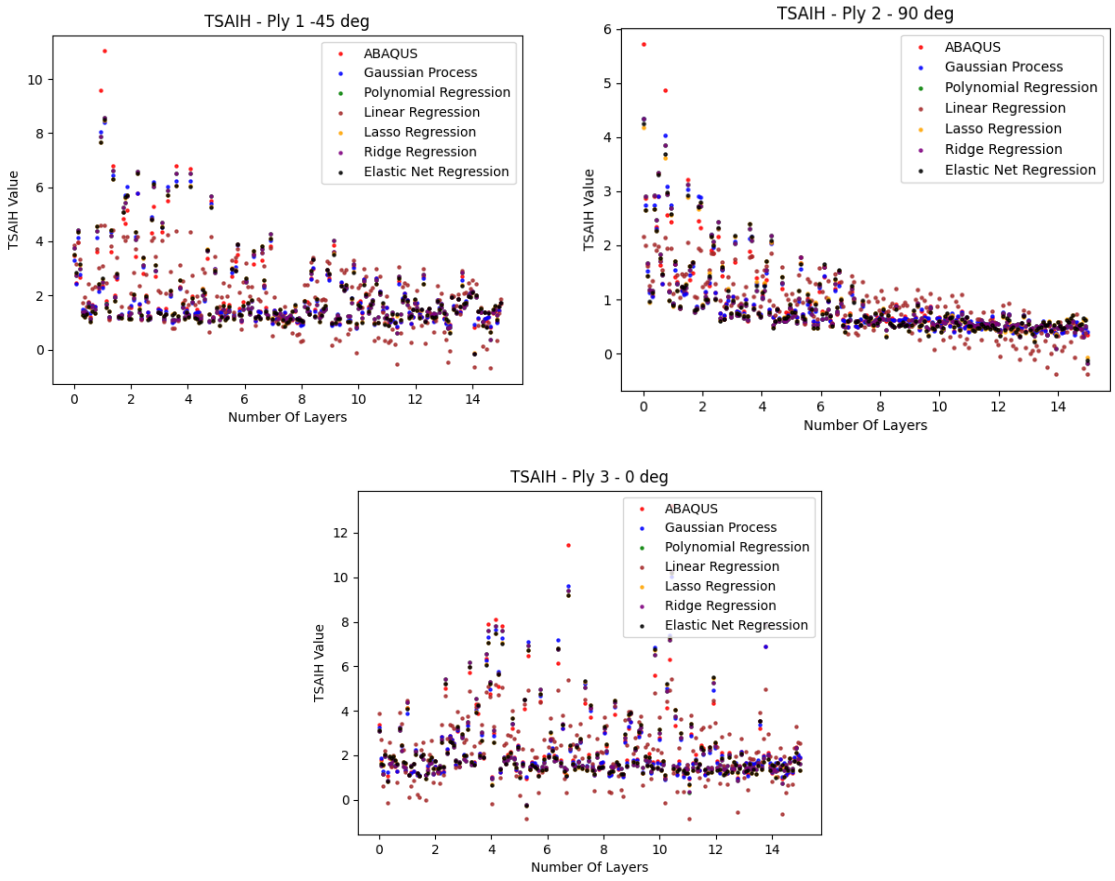

Figure 81: Case4 - Predicted TSAIH for testing samples.

6.4 Genetic Algorithm

This section presents the optimization of the four load cases using the genetic algorithm. All 6 generated surrogate models are used to obtain the most optimized answer.

With a population size of 1000 and maximum iterations of 1000 runs are conducted in the genetic algorithm to obtain the most optimize number of layers and the orientation for the tensile plate. Upper and lower boundaries are set to 0 to 15 layers. The expected answer verifying with the Abaqus software, and the obtained answers are presented in Table 15. The answers in red fonts indicate the failures in the Abaqus model. By analyzing the obtained results, it can be seen that despite the difference in precision, all models are optimizing with the expected orientation.

Table 15: Obtained answers in Abaqus simulation and surrogate models.

	Case 1 – Tensile plate	Case 2 – Pure shear	Case 3 – Four-point bending	Case 4 – Cylinder
Orientation	[±45º, 90º, 0º]	[±45º, 90º, 0º]	[0º, 90º, ±45º]	[±45º, 90º, 0º]
Expected answer	**[0, 0, 7]**	**[7, 0, 0]**	**[7, 0, 0]**	**[0, 7, 0]**
Linear regression	[0, 0, 13]	[9, 0, 0]	[4, 0, 0]	[0, 12, 0]
Polynomial features	[0, 0, 10]	[6, 0, 0]	[8, 0, 0]	[0, 8, 0]

Gaussian regression	[0, 0, 9]	[7, 0, 0]	[7, 0, 0]	[0, 9, 0]
Ridge model	[0, 0, 7]	[6, 0, 0]	[9, 0, 0]	[0, 8, 0]
Lasso model	[0, 0, 11]	[9, 0, 0]	[7, 0, 0]	[0, 8, 0]
Elastic model	[0, 0, 11]	[6, 0, 0]	[5, 0, 0]	[0, 8, 0]

Following this section, it is concluded to use the Gaussian regression for generating the surrogate model.

6.5 Multiple section test

The internal cylinder example presented in section 5.3 is continued here as the multiple section test. This test is used to assess the precision of the genetic algorithm and the surrogate model with multiple sections under nonsymmetric loadings. For simplicity, 200 samples were chosen to simulate Abaqus and the combinations are generated using DoE with Latin Hyper Cubic method.

Abaqus model

The model for a cylinder with two frames is generated in Abaqus using shell elements. The cylinder is divided into 5 sections as shown in Figure 57. The material properties used are the same as for the four loading cases in section 6.1 (Table 14, Figure 63, Figure 64 and Figure 65). A cylindrical coordinates system is used for this specific case.

Symmetric layups are created with the fixed orientations ($[\pm 45^o, 90^o, 0^o]_s$) for each section. Fixed boundary conditions (Ux = Uy = Uz = URx = URy = URz = 0) are applied to the end frames of the cylinder (Figure 82). An internal pressure of 0.8 MPa is applied to the cylinder skin. On a selected point of the model, a concentrated force of 1000 N is applied in y and z directions as shown in Figure 83.

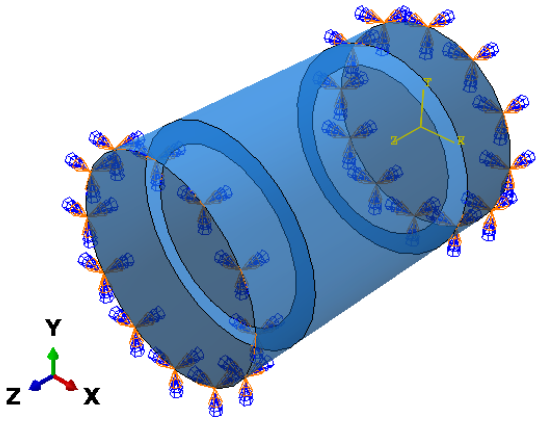

Figure 82: Fixed boundary conditions on the cylinder end

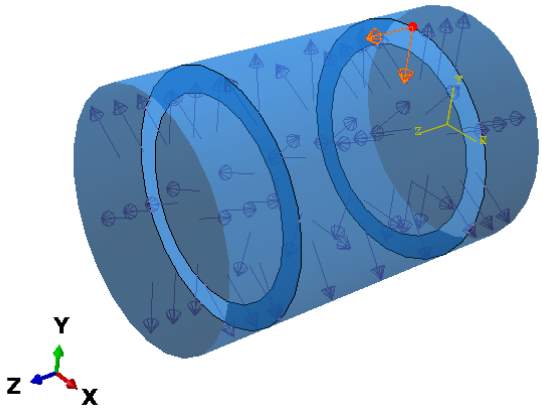

Figure 83: Internal pressure and the unsymmetrical concentrated load.

After a mesh convergence analysis, a mesh of linear quadrilateral elements of type S4R is generated.

Surrogate model

A training set of 200 samples from 0 to 15 is generated according to the Latin Hyper Cubic technique to simulate in Abaqus. Considering that the model is divided into 5 sections, the

surrogate model will be generated with 15 variables. The simulated samples are plotted in Figure 84 with the maximum Tsai hill of each section.

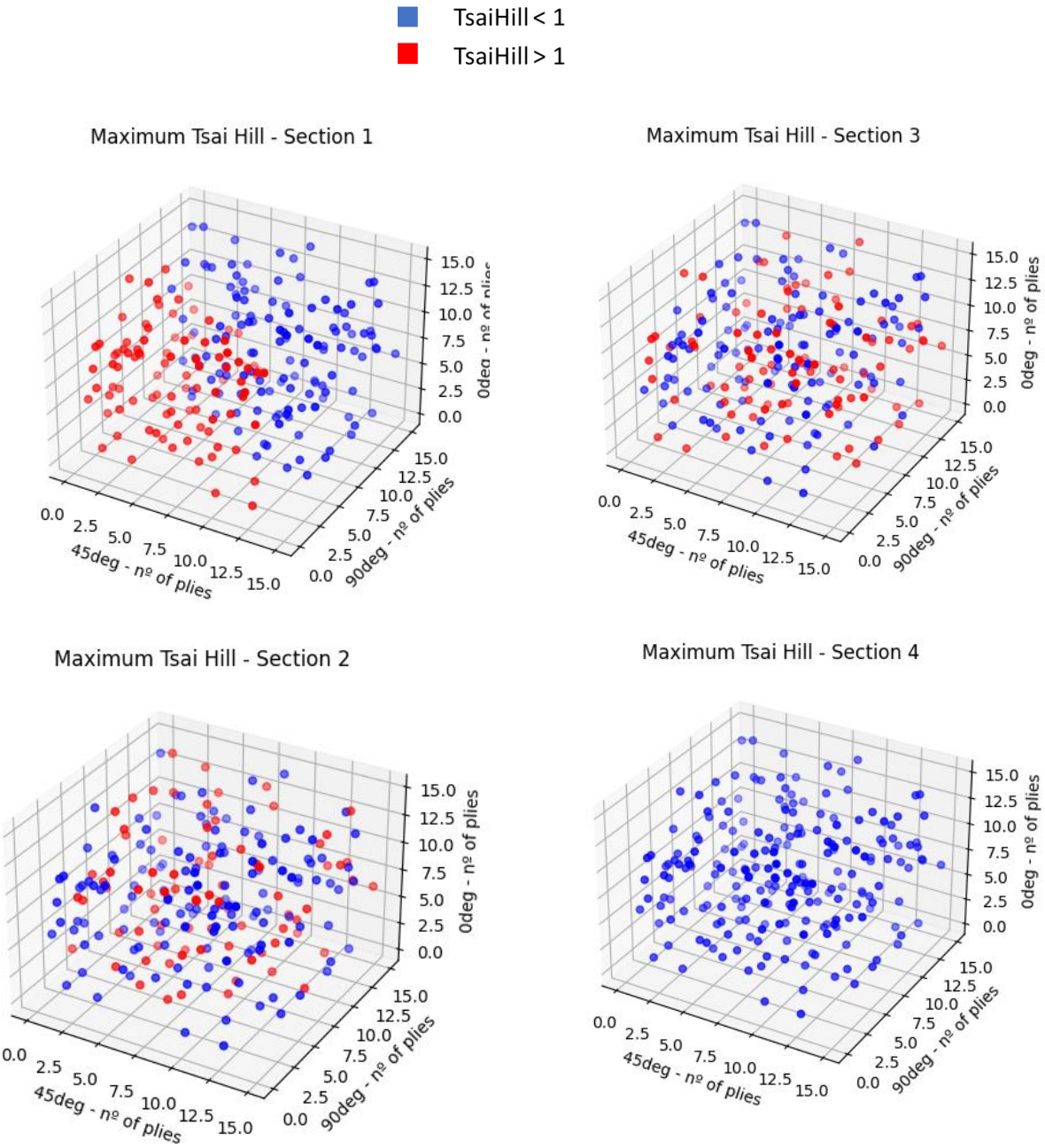

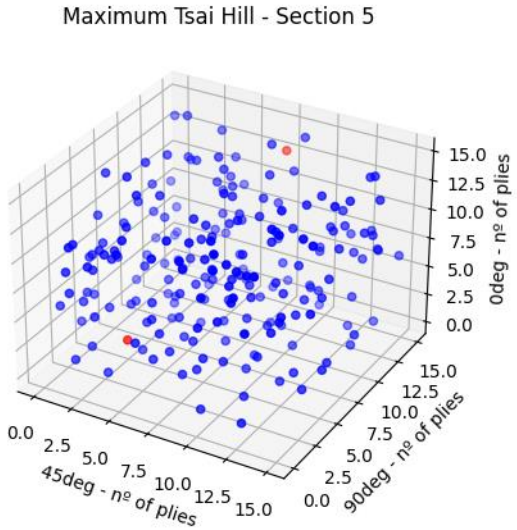

Figure 84: Maximum Tsai Hill of each section plotted with the number of layers.

The surrogate model is generated using the Gaussian regression model. For the generated surrogate model, the prediction for the first section is presented in Figure 85. The R-square values and the mean error of each ply in each region are presented in Table 16.

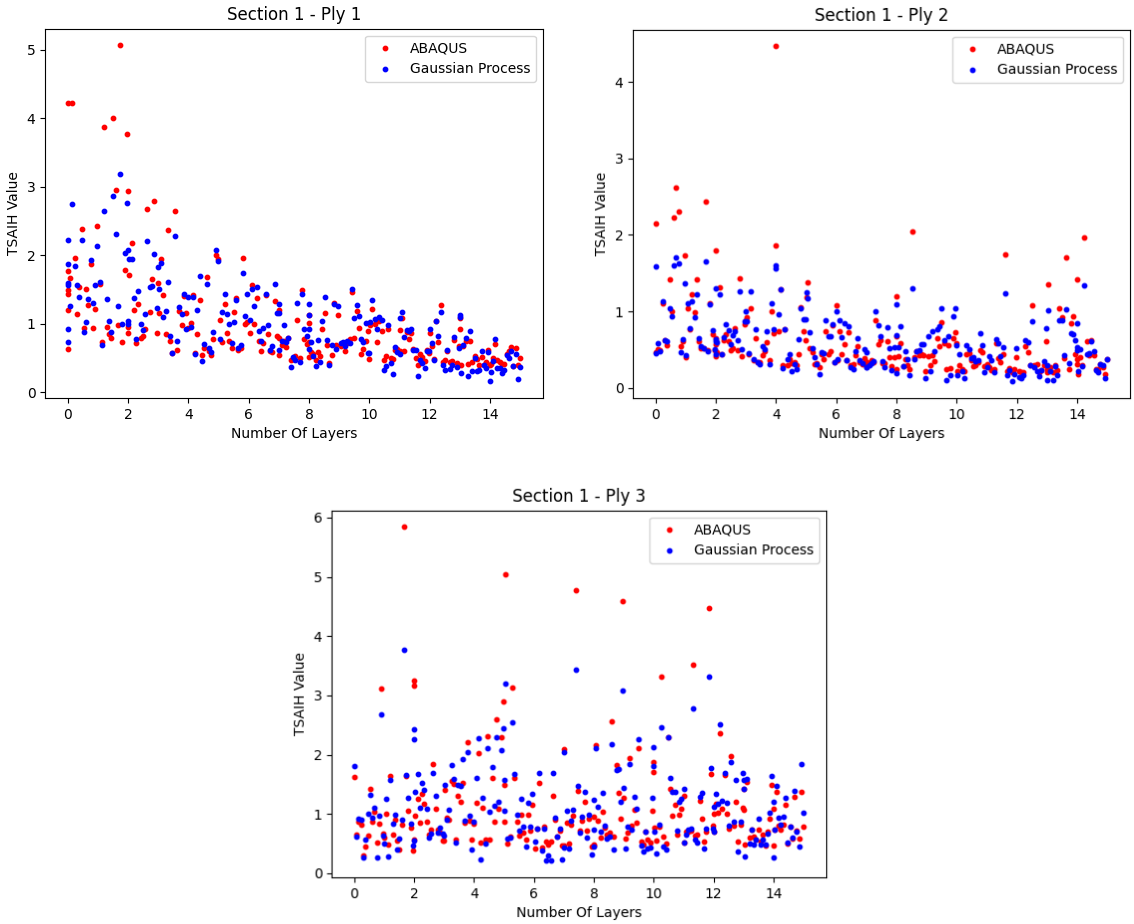

Figure 85: Surrogate model for the 3 plies of the first section.

Table 16: R-squared value and mean error of each ply in each section.

	R-squared value	Mean error
Section 1 - Ply 1	0.675	0.5063
Section 1 - Ply 2	0.466	0.6756
Section 1 - Ply 3	0.823	0.3300
Section 2- Ply 1	0.525	0.4292
Section 2- Ply 2	0.330	0.3125
Section 2- Ply 3	0.644	0.4469
Section 3 - Ply 1	0.663	0.3695
Section 3 - Ply 2	0.286	0.4395
Section 3 - Ply 3	0.842	0.2677
Section 4 - Ply 1	0.802	0.0522
Section 4 - Ply 2	0.776	0.0273
Section 4 - Ply 3	0.792	0.0663
Section 5 - Ply 1	0.852	0.0471
Section 5 - Ply 2	0.870	0.0205
Section 5 - Ply 3	0.871	0.0524

As the surrogate model in some cases doesn't represent the simulated values as expected, the mean error of the testing data set is used to correct the model.

Genetic Algorithm

With an upper and lower bound of 0 to 15 layers of individuals, the optimization algorithm is processed. In order to identify the effect of population size and the maximum iteration size, two sensitivity analyses were carried out. By changing the defined maximum number of iterations, the genetic algorithm was processed to obtain the results. The variation of results is presented in Figure 86. The population size is varied, and the results are noted in Figure 87.

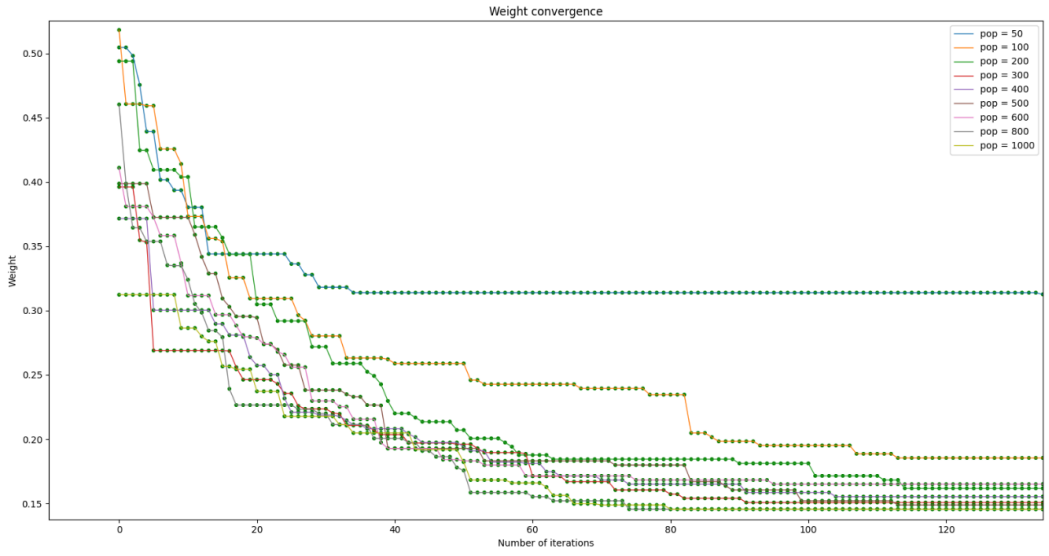

Figure 86: Effect of defined maximum number of iterations on the final answer.

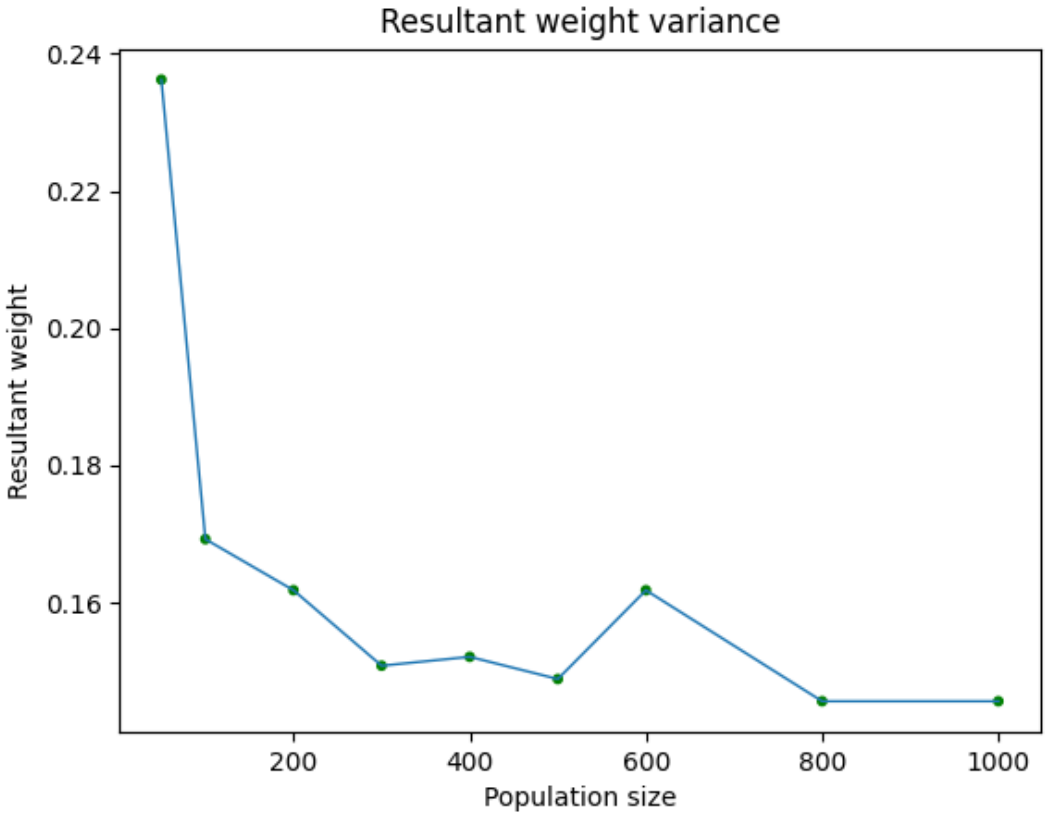

Figure 87: Effect of population size for the final answer.

Considering the above sensitivity analysis, population sizes of 1000 and 1000 maximum iterations are defined in the genetic algorithm. The optimization algorithm is employed to obtain the number of layups and orientations in each ply in each section.

The obtained results are as follows. The weight convergence analysis is presented in Figure 88.

Optimized combination:

Layup	±45º, 90º, 0º
Section 1	**4, 15, 12**
Section 2	**0, 14, 0**
Section 3	**0, 12, 9**
Section 4	**0, 1, 0**
Section 5	**0, 1, 0**

Iterations = 528

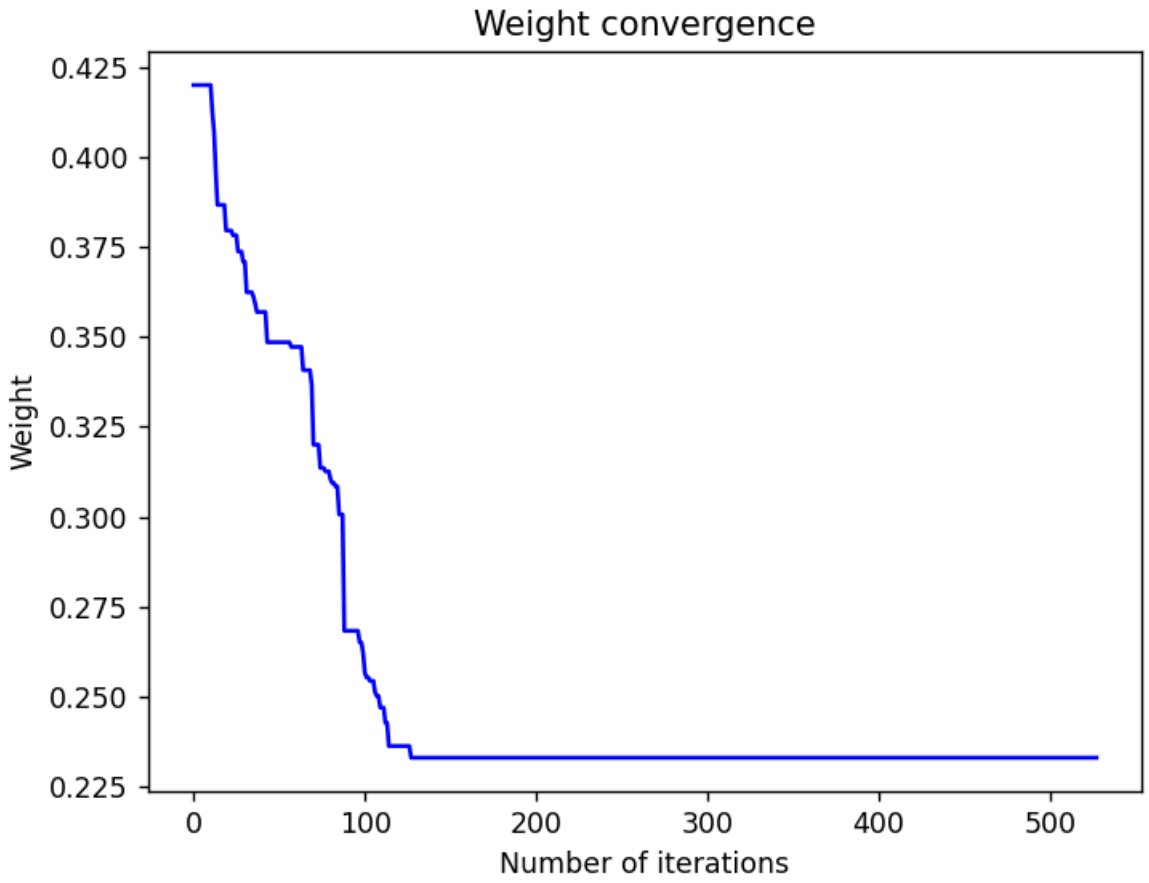

Figure 88: Weight convergence analysis with surrogate model considering the error.

The obtained result is tested in Abaqus. The maximum Tsai Hill value in each section envelope (considering all 3 plies) after neglecting the regions closer to boundary conditions are presented in Figure 89, Figure 90, Figure 91, Figure 92 and Figure 93.

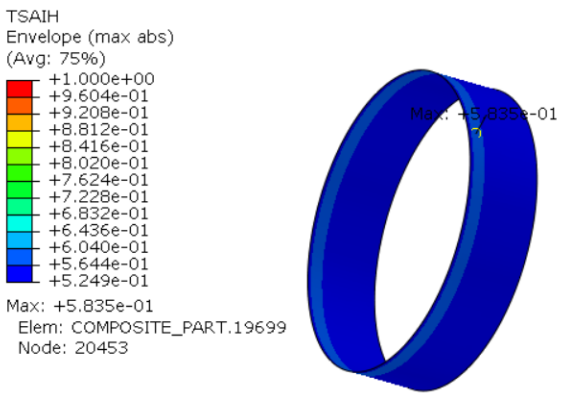

Figure 89: Section 1 - Maximum Tsai Hill of the envelope.

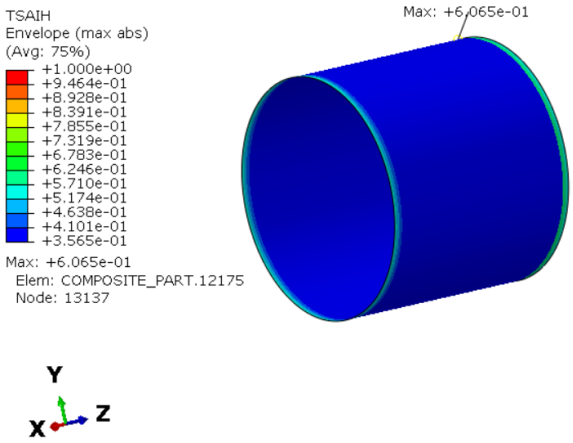

Figure 90: Section 2 - Maximum Tsai Hill of the envelope.

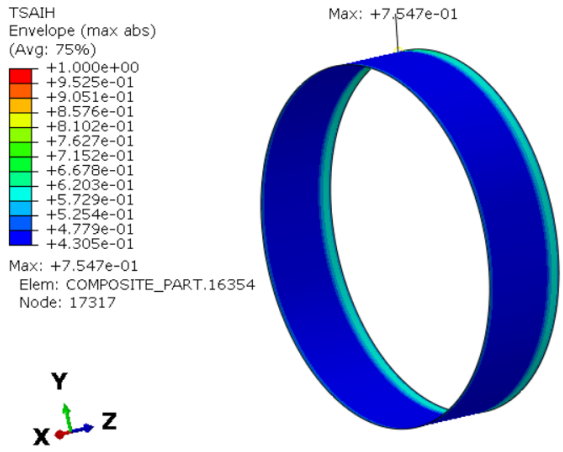

Figure 91: Section 3 - Maximum Tsai Hill of the envelope.

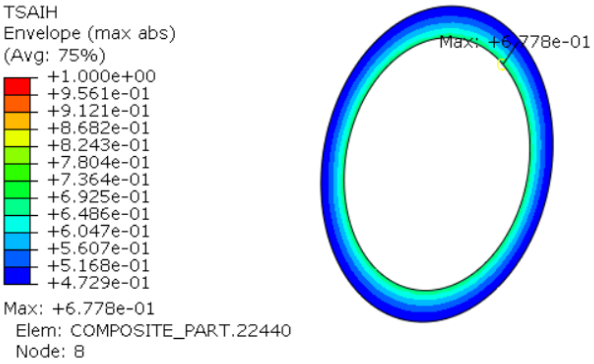

Figure 92: Section 4 - Maximum Tsai Hill of the envelope.

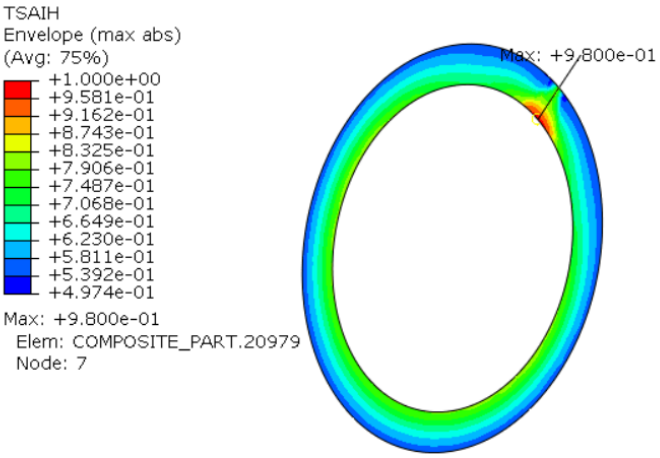

Figure 93: Section 5 - Maximum Tsai Hill of the envelope.

From the obtained results, it can be seen that considering the mean error in the surrogate model to correct the predicted values provides better results. However, with the obtained combination of results and the Tsai Hill values it can be seen that the layup can be further optimized. Considering that the surrogate model is generated by predicting results from 15 variables, the simulated samples are way too less. The best way to improve the precision of the surrogate model is to simulate more samples which will help to predict this complex model more precisely, but due to the computational resources and the time required, this was not pursued.

7 Optimization of the composite fuselage

This section applies the developed optimization tool to optimize the second aircraft fuselage designed in Section 4. Due to the computational time required for this optimization, only the skin of the central part is analyzed in the first iteration with the fixed layup in frames.

7.1 Abaqus model

A Python script is created for automatically generating the Abaqus model with the defined initial parameters.

The same material data indicated in Section 6.1 - Table 14, Figure 63, Figure 64 and Figure 65 are used for this model. The whole model is generated as shell elements except for the wing-fuselage connection rods, which are solid elements. The whole model is created as one part in Abaqus, which is inserted into the assembly.

The part of the wing and the tail boom are modelled for the analysis of the fuselage in order to add boundary conditions away from the analyzed region. The front section of the fuselage is removed from the analysis.

The analyzed sections have meshed with quadrilateral shell elements. Even though ideally the finer meshes should be generated around the opening and stress concentration points, for this first iteration, a continuous mesh is generated following the mesh convergence analysis, Figure 94. The mesh convergence analysis used the maximum TSAIH value in the analyzed section. A model with around 30000 elements was created for simulation, Figure 95.

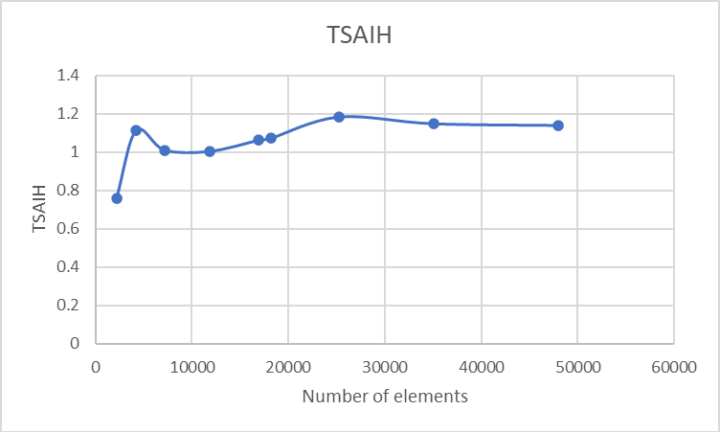

Figure 94: Mesh convergence analysis in the analyzed section of the fuselage.

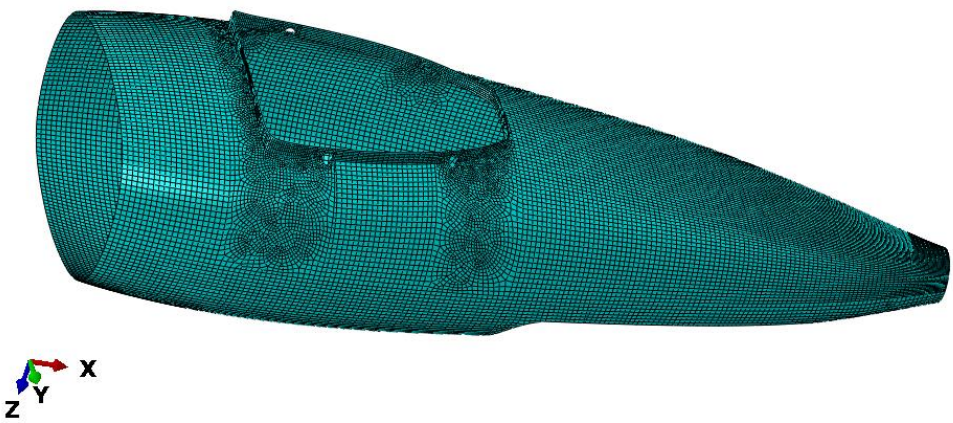

Figure 95: Generated mesh on the analyzed part of the fuselage.

Fixed boundary conditions (Ux = Uy = Uz = URx = URy = URz = 0) are applied in the frontmost section of the fuselage as presented in Figure 96. Loads calculated in Section 4.4 applied to the model. Loads are distributed using constraints to the airframe. The inertial loads are applied to the centre of gravity of the aircraft (reference point 1 RP-1), and the load is constrained to the two side strips of the fuselage (Figure 97).

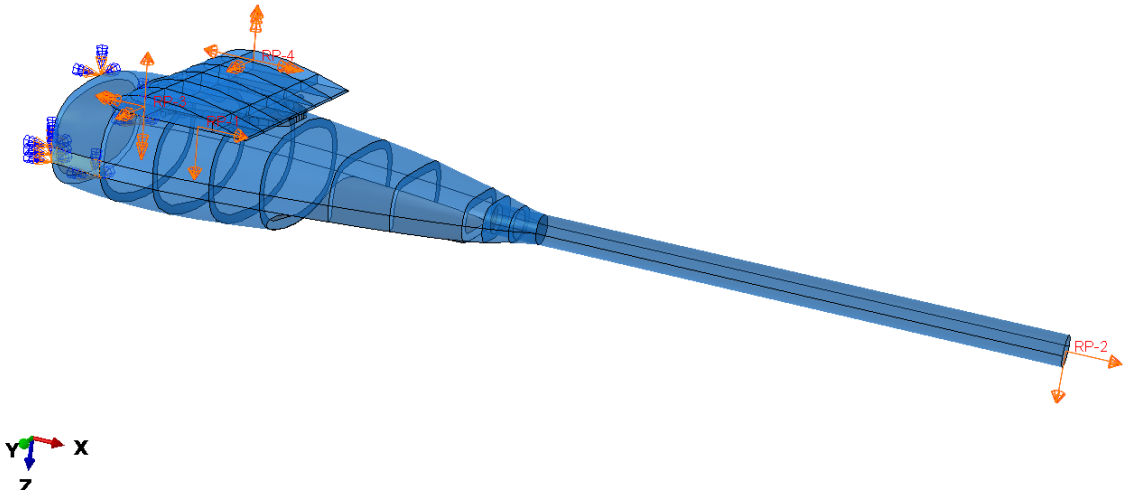

Figure 96: Boundary conditions and applied loads.

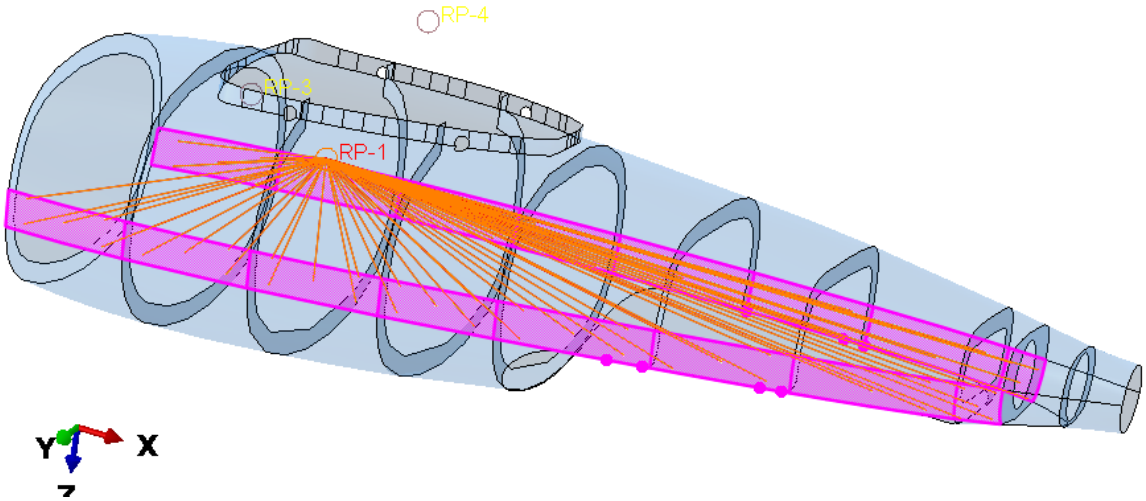

Figure 97: Inertial load distribution.

The equivalent wing loads and moments are calculated and applied to the end main spar of the modelled wing (Figure 98).

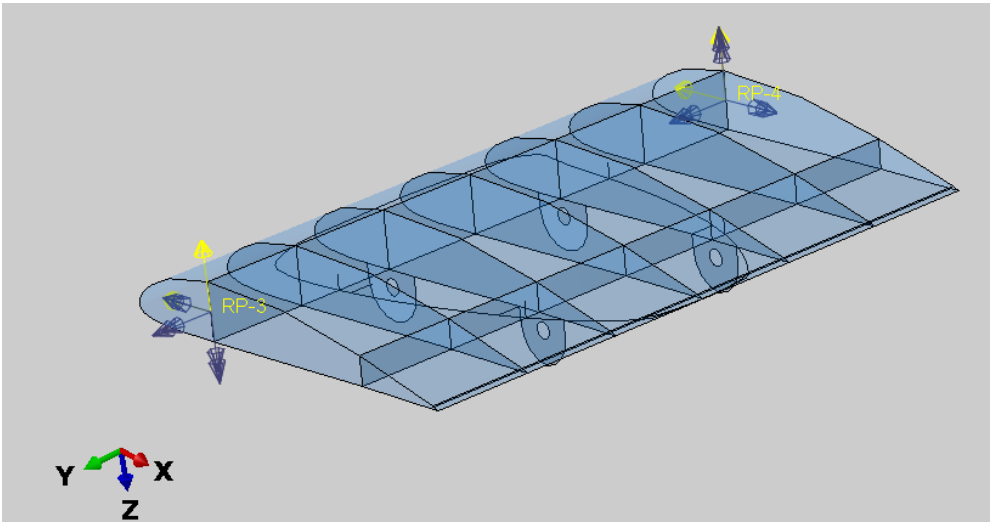

Figure 98: Equivalent wing loads applied to the modelled portion.

The analyzed regions in the fuselage are divided into 7 sections. The sections are presented in Figure 99 with different colours.

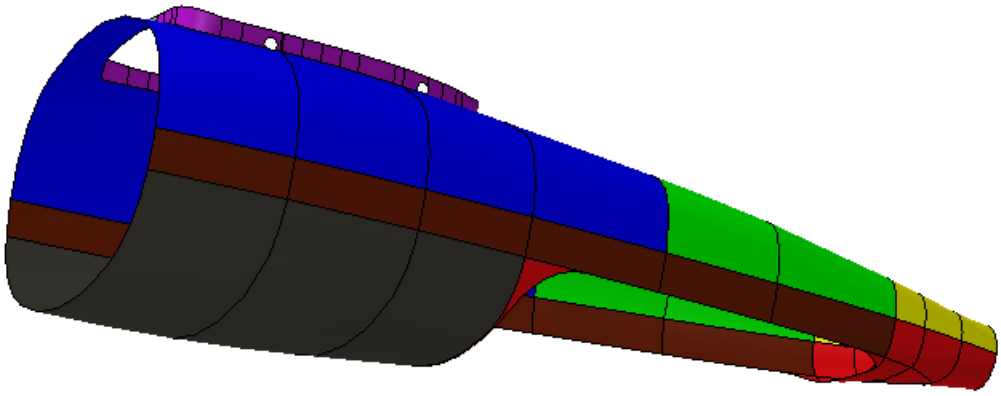

Figure 99: Analyzed fuselage sections in colours.

7.2 Surrogate model

A surrogate model of the Tsai Hill of the above presented FEM is created. Ideally, the number of samples for a training set to simulate should be determined using a sensitivity analysis. However, due to the computational time required and as the first iteration, 600 samples were chosen and simulated in Abaqus software. The maximum TSAIH of each ply in each section is recorded. Another set of samples is simulated as testing samples. DoE with the Latin Hyper Cubic technique is used to form the combination of the training set in the range of 0 to 15. Considering that the fuselage has 7 sections, the surrogate model will have 21 dependent variables.

The obtained training set is used with the Gaussian regression to obtain the numerical surrogate model of the FEM failure index.

A testing set is created to evaluate the generated model. The testing set consists of the general distribution of combinations along the limits as shown in Figure 100. The plots show that the

majority of the points are predicted accurately while some higher TSAIH values are not accurately predicted by the surrogate values. The R-square value and the mean error are presented in Table 17. The rest of the plots are presented in Appendix A.

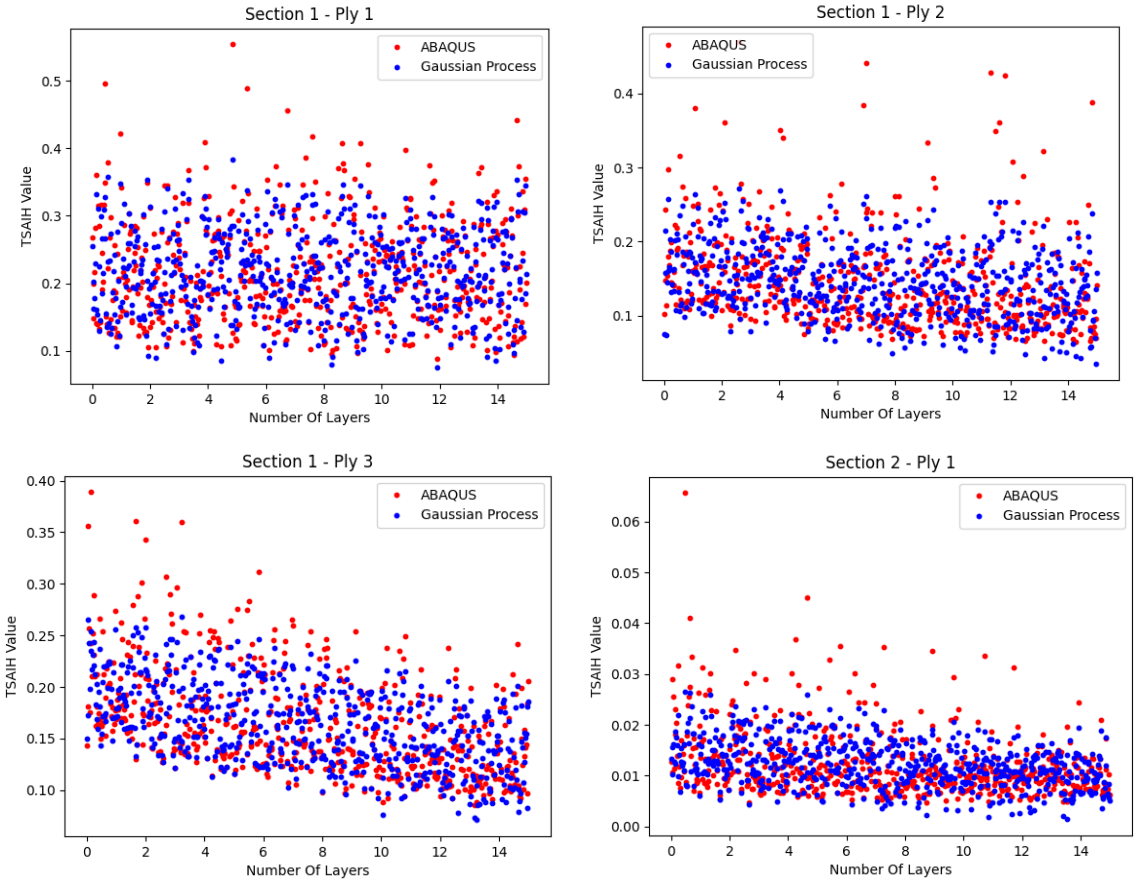

Figure 100: Testing set - Gaussian prediction and FEM simulated values.

Table 17: R-square value and the mean error of the test sets.

	Testing set 1	
	R^2 - Value	Mean error
Section 1 - Ply 1	0.76	0.0484
Section 1 - Ply 2	0.807	0.0355
Section 1 - Ply 3	0.68	0.0429
Section 2- Ply 1	0.664	0.0069
Section 2- Ply 2	0.653	0.0087
Section 2- Ply 3	0.716	0.0065
Section 3 - Ply 1	0.663	0.005
Section 3 - Ply 2	0.513	0.0126
Section 3 - Ply 3	0.536	0.0102
Section 4 - Ply 1	0.624	0.0083
Section 4 - Ply 2	0.702	0.0055

Section 4 - Ply 3	0.589	0.0066
Section 5 - Ply 1	0.614	0.0145
Section 5 - Ply 2	0.565	0.0156
Section 5 - Ply 3	0.6	0.0123
Section 6 - Ply 1	0.823	0.0764
Section 6 - Ply 2	0.896	0.0236
Section 6 - Ply 3	0.753	0.0587
Section 7 - Ply 1	0.752	0.0104
Section 7 - Ply 2	0.776	0.0082
Section 7 - Ply 3	0.664	0.0135

Observing the obtained surrogate model, the high failure indices generated from combinations with a lower number of layers are not properly predicted in the mode. However, this low number of layers plays an important job in genetic algorithms while evaluating the constraints. Hence, a second testing set is generated with combinations between 0 to 3 layers. The first four plots are presented in Figure 101. It can be seen that even though in general the surrogate model predicts values with fewer errors, the combinations with a lower number of layers are predicted vaguely. The rest of the plots are presented in Appendix A.

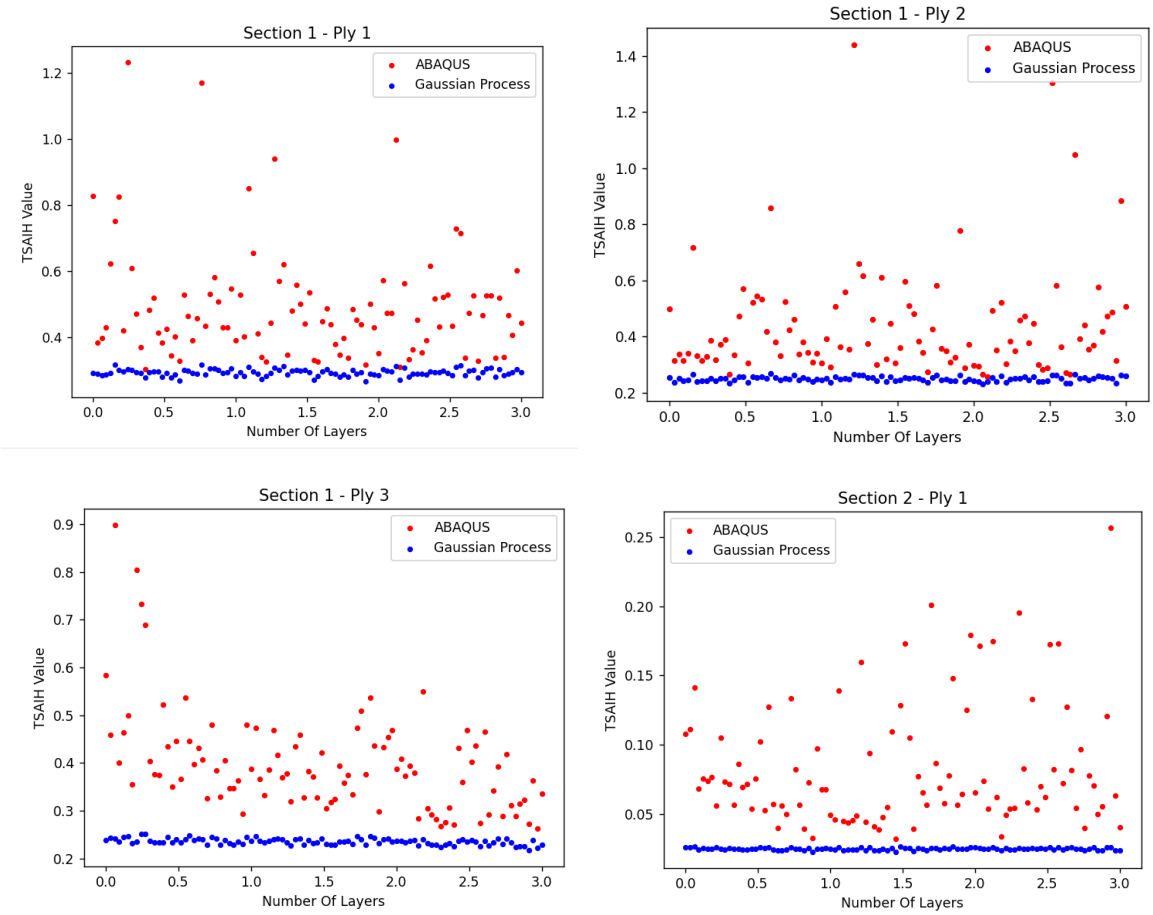

Figure 101: Testing set 2 Gaussian predictions and FEM simulated values.

In some distinct cases, as the surrogate model doesn't represent the FEM model accurately, the mean error is used in the failure index to correct this discrepancy.

7.3 Genetic Algorithm

The order to evaluate the methodology and the algorithm, the surrogate model is used in the genetic algorithm and the following results are obtained.

Weight = 408.82 g

Optimized combination:

Layup	0º, 90º, ±45º
Section 1	**0, 0, 1**
Section 2	**0, 1, 0**
Section 3	**0, 1, 0**
Section 4	**0, 1, 0**
Section 5	**0, 0, 1**
Section 6	**0, 1, 0**
Section 7	**0, 0, 1**

Iterations = 425

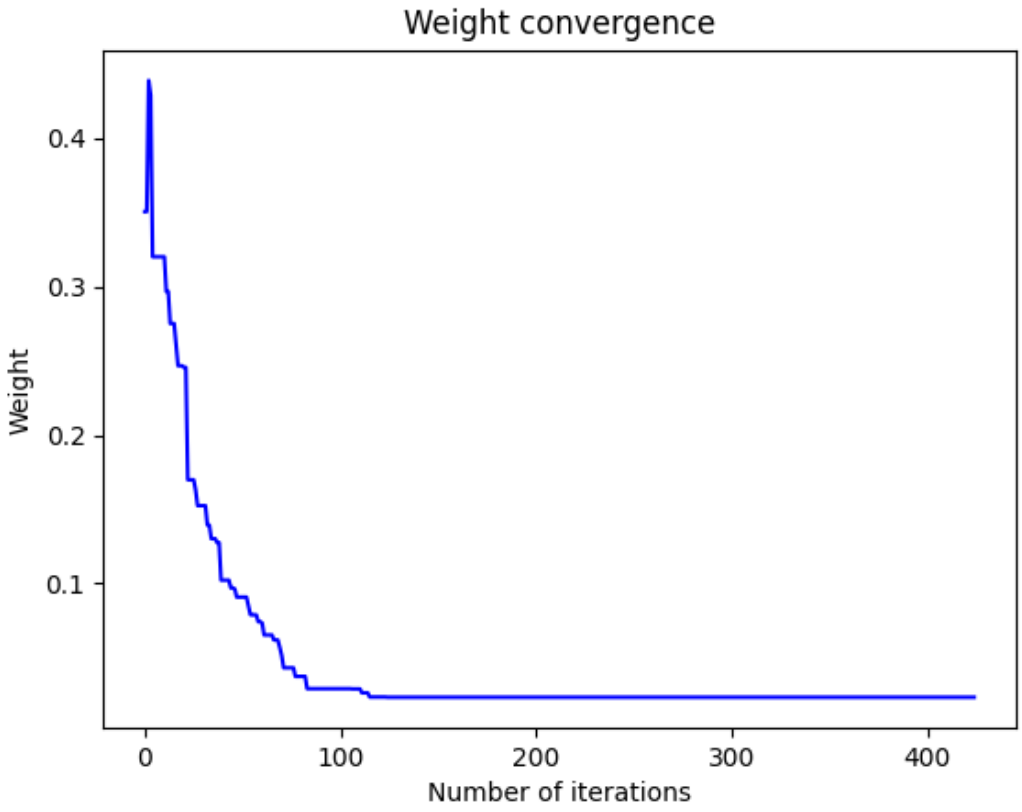

Figure 102: Weight convergence analysis from GA.

Obtained results are simulated in Abaqus in order to verify the results. The ply with the maximum Tsai Hill value for each section are presented in Figure 103, Figure 104, Figure 105, Figure 106, Figure 107, Figure 108 and Figure 109. As observed from the figures some of the

sections are failing with Tsai Hill up to 1.4 values. Considering that this model includes 21 variables and only 600 samples were simulated to obtain the surrogate model, in order to increase the precision of the results, the number of samples should be increased. However due to the required computational resources and the time for this present thesis, the application of the optimization tool is finalised here with these obtained results.

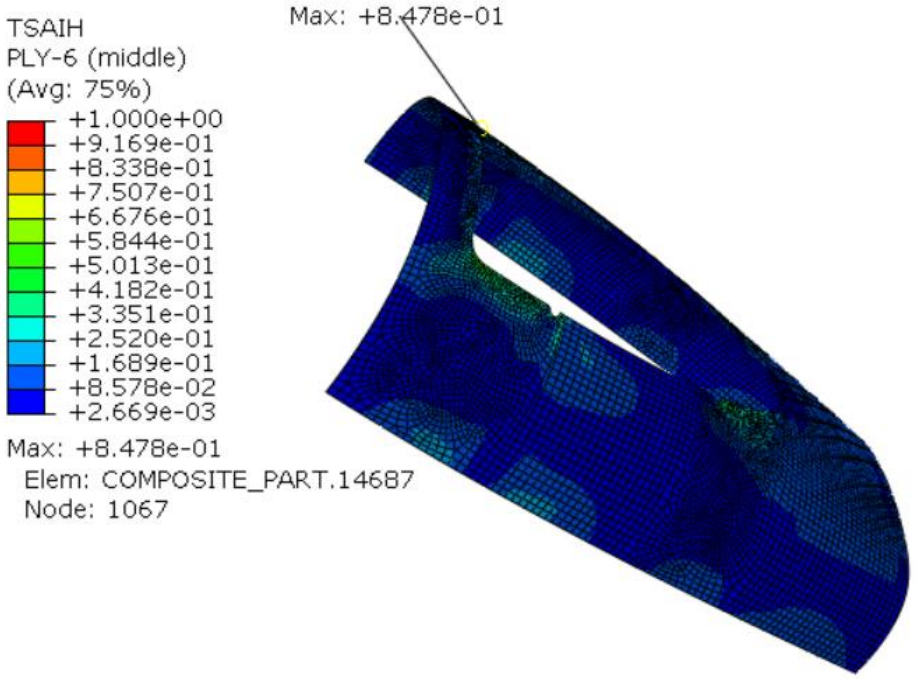

Figure 103: Section 1 - Ply with the maximum Tsai Hill value.

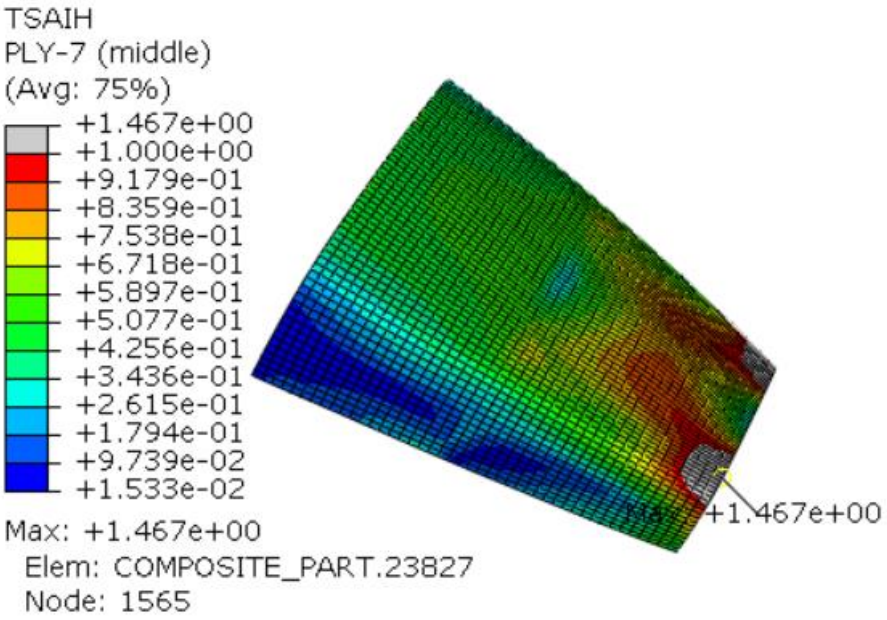

Figure 104: Section 2 - Ply with the maximum Tsai Hill value

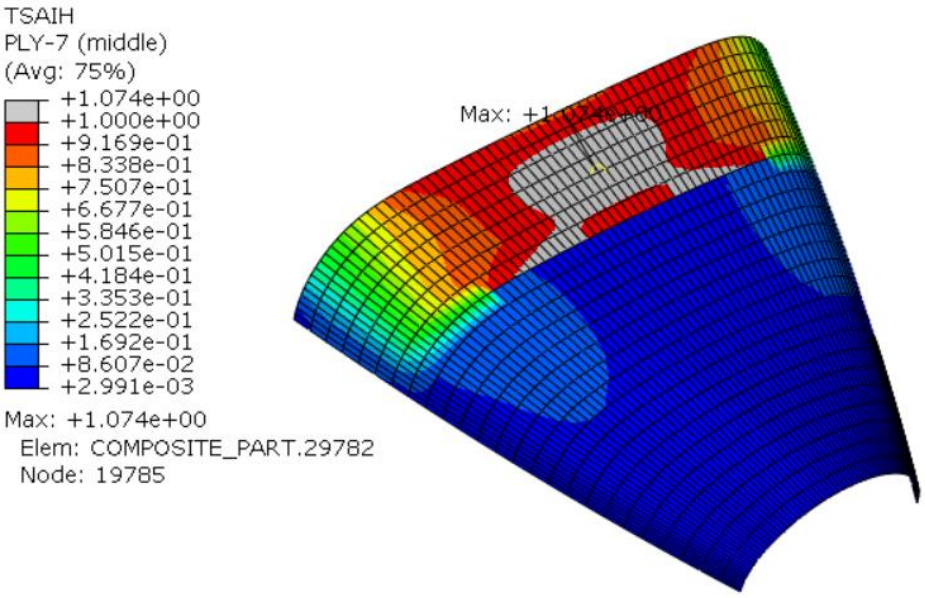

Figure 105: Section 3 - Ply with the maximum Tsai Hill value.

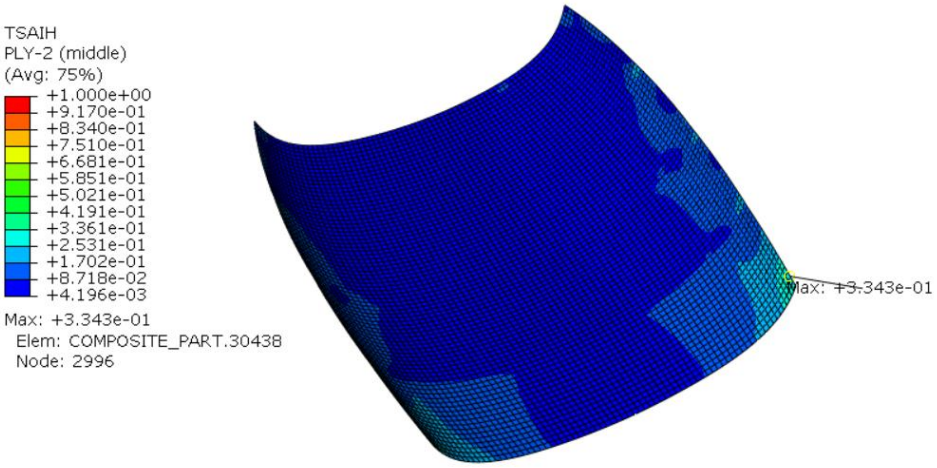

Figure 106: Section 4 - Ply with the maximum Tsai Hill value.

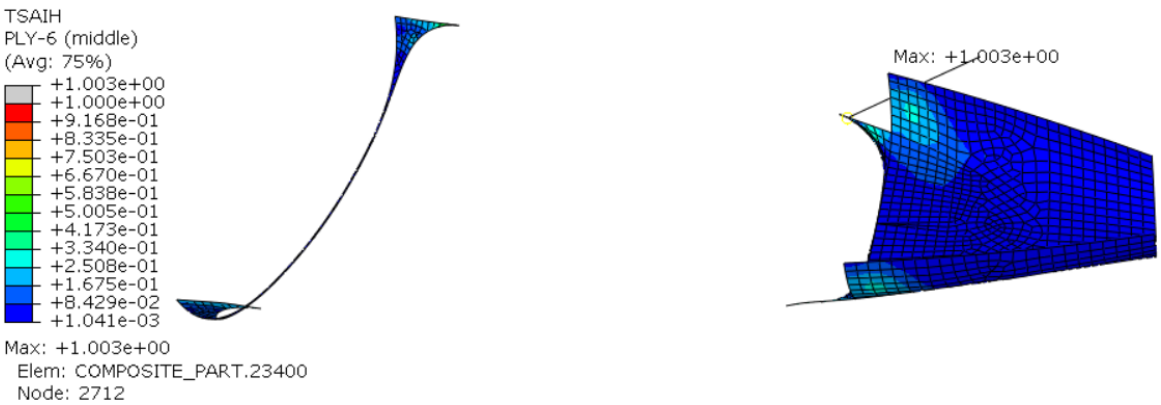

Figure 107: Section 5 - Ply with the maximum Tsai Hill value.

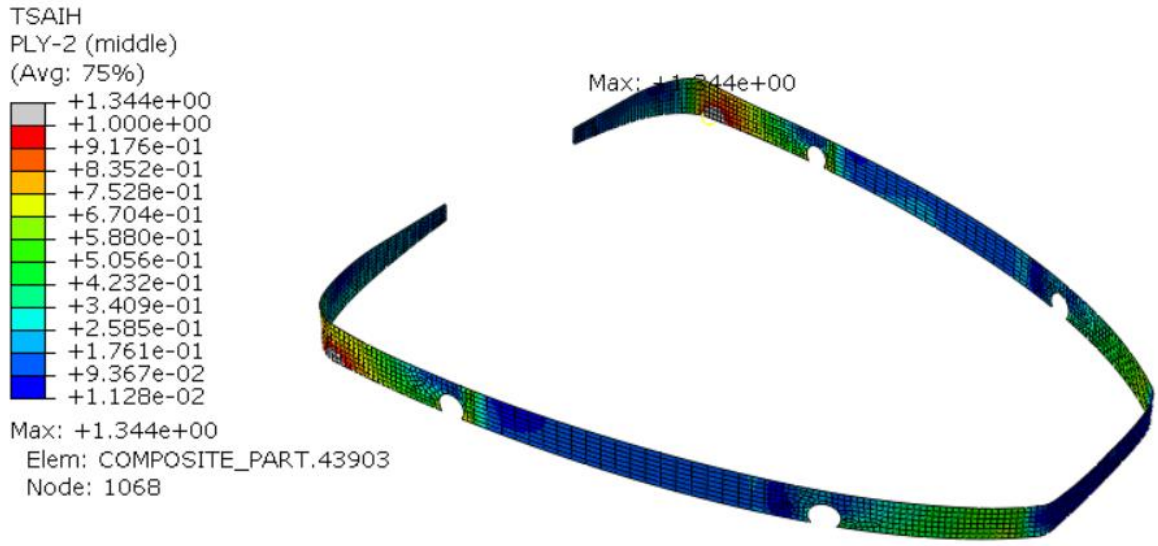

Figure 108: Section 6 - Ply with the maximum Tsai Hill value.

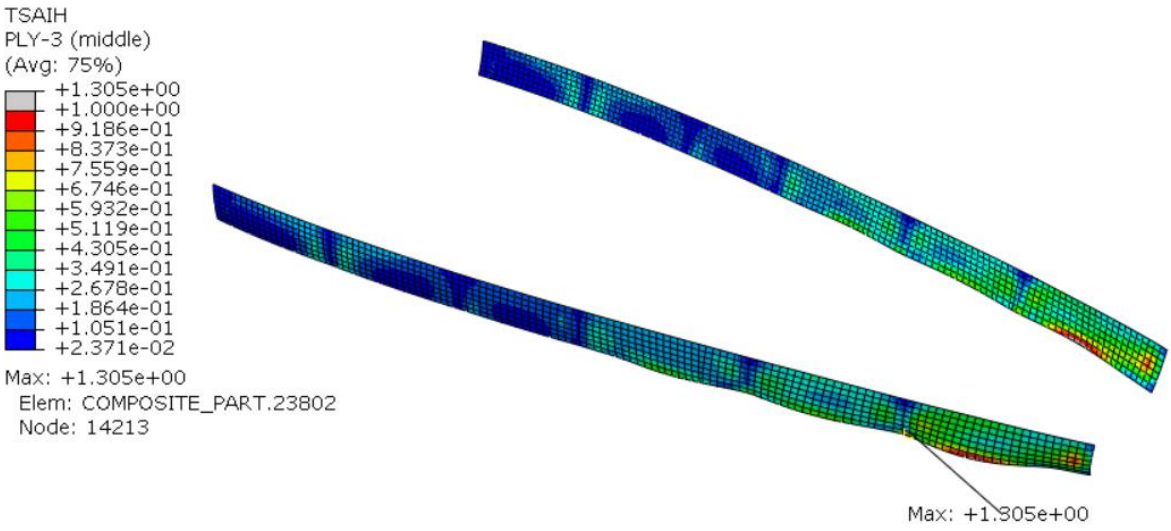

Figure 109: Section 8 - Ply with the maximum Tsai Hill value.

8 Conclusion

This thesis was carried out with the objective of developing fixed wing UAV for medical item delivery and developing a custom computational tool that can be used to optimize composite fuselage with preferred constrains.

The development of the first aircraft was successfully achieved while considering specific requirements. The entire process involved various stages, including sizing, design, aerodynamics, and structural analysis and manufacturing. Successful flight tests were conducted, providing valuable data to validate the methodologies used for sizing and manufacturing. The successful completion of the first aircraft prototype represents a significant milestone in this work.

Building upon the knowledge gained from the first aircraft, the thesis proceeded to develop a second UAV specifically tailored for medical item delivery, through careful consideration of the design requirements and optimization constraints. The second UAV specifically tailored for medical item delivery was successfully created.

Recognizing the importance of optimizing the structure of the medical UAV, a custom computational tool was developed and implemented. This tool utilized the Genetic algorithm and a surrogate model, incorporating Abaqus finite element software to obtain the failure index. The optimization algorithm was designed to optimize both the number of layers and the ply orientation in each section of the structure. To generate the surrogate model, a Design of Experiments (DoE) approach employing the Latin Hyper Cubic method was employed to generate the combinations of sampling the data. These samples were then simulated in Abaqus and maximum Tsai Hill values in each section for each ply is obtained through a post processing script. Amongst the six regression methods compared using test cases, the Gaussian regression method was selected as the most suitable choice for generating the surrogate model for this application. The optimization algorithm was subsequently validated using four simple load cases as well as a multi-section test case. The validation process highlighted the importance of simulating a higher number of samples when a higher number of variables are present to achieve a more precise surrogate model that accurately captures the variables present in the analysis.

Finally, the developed optimization algorithm was implemented in the developed medical UAV fuselage. The obtained results applying the developed optimization tool indicates that 3 sections are failing with failure index value up to 1.4. However, this approximated method generates the ply orientations in adequate directions. It is recognized that for a multi regression problem with 21 variables more samples should be simulated to obtain more precise results.

In conclusion, this thesis successfully developed, manufactured, and tested the first aircraft. The second aircraft is designed with optimized parameters. Finally, it is demonstrated that the possibility of applying the custom developed optimization tool to the analysis of the composite fuselage.

Future works

While this thesis successfully accomplishes the development of a fixed-wing UAV for medical item delivery and the creation of a custom computational tool for optimizing composite fuselage designs, there are several potential avenues for future research and improvement in this field.

Advanced Optimization Techniques: Explore and implement advanced optimization techniques, such as metaheuristic algorithms like Particle Swarm Optimization (PSO), Ant Colony Optimization (ACO), or Simulated Annealing (SA). These algorithms can potentially improve the efficiency and effectiveness of the optimization process, allowing for more precise and faster convergence towards optimal solutions.

Integration of Multi-Objective Optimization: Extend the optimization framework to include multiple objectives, such as minimizing weight, maximizing range, and optimizing aerodynamic performance simultaneously. This can be achieved through the integration of multi-objective optimization algorithms like the Non-dominated Sorting Genetic Algorithm (NSGA-II) or the Strength Pareto Evolutionary Algorithm (SPEA2).

Improved Surrogate Modelling Techniques: Investigate and implement advanced surrogate modelling techniques to enhance the accuracy and efficiency of the optimization tool. Explore techniques like Kriging, Support Vector Regression (SVR), or Radial Basis Functions (RBF) to improve the surrogate model's predictive capabilities and reduce computational costs.

Incorporation of Additional features: Expand the optimization tool to accommodate additional features such as the effect of suddenly varying the thickness of neighbouring section.

Additional post processing parameters: The developed optimization tool can be customized to consider wide range of constraints such as stiffness, displacement and fatigue and damage tolerance aspects.

References

[1] L. P. (Laszlo P. Kollar and G. S. Springer, 'Mechanics of composite structures', p. 480, 2003.

[2] I. M. Daniel, N. York, and H. Oxford, 'ENGINEERING MECHANICS OF COMPOSITE MATERIALS SECOND EDITION Ori lshai', 2006.

[3] M. C. Niu, 'Airframe Stress Analysis and Sizing (2nd Ed 1999)', *Press*, p. 806, 1999.

[4] Christos. Kassapoglou, 'Design and analysis of composite structures : with applications to aerospace structures'.

[5] K. Maalawi, 'Introductory Chapter: An Introduction to the Optimization of Composite Structures', *Optimum Composite Structures*, Jan. 2019, doi: 10.5772/INTECHOPEN.81165.

[6] A. Al-Sammarraie and A. Al-Sammarraie, 'Investigation of corrosion behavior of polymer composites for small aircraft structures. Polymer Composites', *Polym Compos*, 2018.

[7] M. Voge, G. Guenin, and G. Guenin, 'Composite structural design for a two-seat airplane', in *58th AIAA/ASCE/AHS/ASC Structures, Structural Dynamics, and Materials Conference.*, 2017.

[8] J. Zhang, C. Hu, and K. Lee, 'Application of automated fiber placement (AFP) technology in small aircraft manufacturing', *International Journal of Advanced Manufacturing Technology*, 2019.

[9] A. Puri, K. R. Guruprasad, and K. Vasudevan, 'Design and analysis of a small unmanned aerial vehicle (UAV) using composite materials', in *Materials Today*, 2019.

[10] M. Zhou, R. Fleury, and M. Kemp, 'Optimization of composite - Recent advances and application', *13th AIAA/ISSMO Multidisciplinary Analysis and Optimization Conference 2010*, 2010, doi: 10.2514/6.2010-9272.

[11] S. Kilimtzidis, A. Kotzakolios, and V. Kostopoulos, 'Efficient structural optimisation of composite materials aircraft wings', *Compos Struct*, vol. 303, p. 116268, Jan. 2023, doi: 10.1016/J.COMPSTRUCT.2022.116268.

[12] J. C. Martín, 'Composite Optimization Techniques for Aircraft Components Structural Sizing', doi: 10.13009/EUCASS2019-268.

[13] Optistruct, 'Altair Hyperworks17.0 user´s manual.' Altair Engineering Inc, 2022.

[14] S. F. Pitton, S. Ricci, and C. Bisagni, 'Buckling optimization of variable stiffness cylindrical shells through artificial intelligence techniques', *Compos Struct*, vol. 230, p. 111513, Dec. 2019, doi: 10.1016/J.COMPSTRUCT.2019.111513.

[15] T. T. Truong, S. Lee, and J. Lee, 'An artificial neural network-differential evolution approach for optimization of bidirectional functionally graded beams', *Compos Struct*, vol. 233, p. 111517, Feb. 2020, doi: 10.1016/J.COMPSTRUCT.2019.111517.

[16] M. Elmshaikhi and A. Abdallah, 'Rear Fuselage Structural Optimization Using Genetic Algorithm', *Journal of Karary University for Engineering and Science*, Dec. 2021, doi: 10.54388/JKUES.V1I2.61.

[17] 'Ansys optiSLang', *Ansys Documentation*.

[18] 'Dassault Systèmes'. https://www.3ds.com/

[19] C. T. Sun, B. J. Quinn, and J. Tao, 'COMPARATIVE EVALUATION OF FAILURE ANALYSIS METHODS FOR COMPOSITE LAMINATES', *Federal Aviation*

Administration, 1996, Accessed: Jun. 11, 2023. [Online]. Available: www.tc.faa.gov/its/act141/reportpage.html

[20] I. Daniel and O. Ishai, *Engineering Mechanics of Composite Materials*. Oxford University Press, 2006. Accessed: Jun. 11, 2023. [Online]. Available: https://global.oup.com/academic/product/engineering-mechanics-of-composite-materials-9780195150971

[21] A. R. Melro, P. Camanho, A. Arteiro, G. Catalanotti, and M. Vogler, 'Numerical modelling of failure in advanced composite materials', *Numerical Modelling of Failure in Advanced Composite Materials*, pp. 1–541, Aug. 2015, doi: 10.1016/C2014-0-02677-9.

[22] M. Em005 *et al.*, 'Optimization of mechanical systems - optimal design applications', 2021, Accessed: Jun. 12, 2023. [Online]. Available: https://repositorio-aberto.up.pt/handle/10216/139656

[23] D. E. Goldberg and J. H. Holland, 'Genetic Algorithms in Search, Optimization, and Machine Learning David E. Goldberg The University of Alabama T', *Mach Learn*, vol. 3, no. 2, pp. 95–99, 1979.

[24] C. Yan, Z. Yin, X. Shen, D. Mi, F. Guo, and D. Long, 'Surrogate-based optimization with improved support vector regression for non-circular vent hole on aero-engine turbine disk', *Aerosp Sci Technol*, vol. 96, p. 105332, Jan. 2020, doi: 10.1016/J.AST.2019.105332.

[25] P. R. Berthelson *et al.*, 'A finite element–guided mathematical surrogate modeling approach for assessing occupant injury trends across variations in simplified vehicular impact conditions', *Med Biol Eng Comput*, vol. 59, no. 5, pp. 1065–1079, May 2021, doi: 10.1007/S11517-021-02349-3/FIGURES/7.

[26] J. Kudela and R. Matousek, 'Recent advances and applications of surrogate models for finite element method computations: a review', *Soft Computing 2022 26:24*, vol. 26, no. 24, pp. 13709–13733, Jul. 2022, doi: 10.1007/S00500-022-07362-8.

[27] M. D. McKay, R. J. Beckman, and W. J. Conover, 'A Comparison of Three Methods for Selecting Values of Input Variables in the Analysis of Output from a Computer Code', *Technometrics*, vol. 21, no. 2, p. 239, May 1979, doi: 10.2307/1268522.

[28] A. Bhosekar and M. Ierapetritou, 'Advances in surrogate based modeling, feasibility analysis, and optimization: A review', *Comput Chem Eng*, vol. 108, pp. 250–267, Jan. 2018, doi: 10.1016/J.COMPCHEMENG.2017.09.017.

[29] F. Pedregosa and G. Varoquaux, 'Scikit-learn: Machine Learning in Python', *Journal of Machine Learning Research*, vol. 12, 2011.

[30] 'Technology | Zipline Instant Delivery & Logistics'. https://www.flyzipline.com/technology (accessed Jun. 12, 2023).

[31] 'How medical drones help save lives in Tanzania | Delivered | Global'. https://www.dhl.com/global-en/delivered/insights/medical-drones-save-lives-tanzania.html (accessed Jun. 12, 2023).

[32] 'Rapid response from the air: medicines successfully delivered using a parcel drone in East Africa - giz.de'. https://www.giz.de/en/press/70080.html (accessed Jun. 12, 2023).

[33] 'Parcelcopter Drone Project Delivers In Rough Terrain | Hackaday'. https://hackaday.com/2018/10/29/parcelcopter-drone-project-delivers-in-rough-terrain/ (accessed Jun. 12, 2023).

[34] 'UPS expands its medical drone service to University of California San Diego Health - UPS Healthcare™ - Croatia'. https://www.ups.com/hr/en/healthcare/news/press-releases/ups-expands-medical-drone-service-to-university-of-california-san-diego-health.page (accessed Jun. 12, 2023).

[35] 'Swiss Post drone takes off again for healthcare services - Post Medien'. https://post-medien.ch/en/swiss-post-drone-lost-over-lake-zurich/ (accessed Jun. 12, 2023).

[36] 'NHS launches UK's first COVID test drone delivery service in Scotland', *Skyports Drone Services*. https://skyportsdroneservices.com/nhs-launches-uks-first-covid-test-drone-delivery-service-in-scotland/ (accessed Jun. 12, 2023).

[37] 'NHS using drones to deliver coronavirus kit between hospitals | Drones (non-military) | The Guardian'. https://www.theguardian.com/technology/2020/oct/17/nhs-drones-deliver-coronavirus-kit-between-hospitals-essex (accessed Jun. 12, 2023).

[38] D. Raymer, 'Aircraft Design: A Conceptual Approach, Sixth Edition', *Aircraft Design: A Conceptual Approach, Sixth Edition*, Sep. 2018, doi: 10.2514/4.104909.

[39] J. D. Anderson, 'Introduction to flight', p. 814, 2005, Accessed: Jun. 12, 2023. [Online]. Available: https://books.google.com/books/about/Introduction_to_Flight.html?hl=pt-PT&id=pW8U-UddgDMC

[40] I. (Ian) Moir and A. G. (Allan G.) Seabridge, 'Aircraft systems : mechanical, electrical, and avionics subsystems integration', p. 504, 2008, Accessed: Jun. 12, 2023. [Online]. Available: https://books.google.com/books/about/Aircraft_Systems.html?hl=pt-PT&id=2O9kPgAACAAJ

[41] M. H. Sadraey, 'Aircraft design : a systems engineering approach', Accessed: Jun. 12, 2023. [Online]. Available: https://books.google.com/books/about/Aircraft_Design.html?hl=pt-PT&id=VT-Tc3Tx5aEC

[42] R. K. Barnhart, D. M. Marshall, and E. Shappee, 'Introduction to unmanned aircraft systems', Accessed: Jun. 12, 2023. [Online]. Available: https://books.google.com/books/about/Introduction_to_Unmanned_Aircraft_System.html?hl=pt-PT&id=xQDAzQEACAAJ

[43] S. Gudmundsson, 'Performance – Introduction', *General Aviation Aircraft Design*, pp. 761–789, Jan. 2014, doi: 10.1016/B978-0-12-397308-5.00016-7.

[44] A. Majka, 'Flight loads of mini UAV', *Solid State Phenomena*, vol. 198, pp. 194–199, 2013, doi: 10.4028/WWW.SCIENTIFIC.NET/SSP.198.194.

[45] Easa - European Union Aviation Safety Agency, 'Easy Access Rules for Very Light Aeroplanes (CS-VLA) (Amendment 1)', 2018. https://www.easa.europa.eu/en/document-library/easy-access-rules/easy-access-rules-very-light-aeroplanes-cs-vla (accessed Jun. 06, 2023).

ADDENDIX A: Aircraft sizing equations - tail and longitudinal stability

$$\alpha_t = \alpha + i_t - \varepsilon \quad (60)$$

$$\varepsilon = \frac{2 * CL_{wing}}{\pi * AR_{wing}} \quad (61)$$

$$\varepsilon_0 = \frac{2 * CL_{0_{wing}}}{\pi * AR_{wing}} \quad (62)$$

$$\frac{d\varepsilon}{d\alpha} = \frac{2 * CL_{a_{wing}}}{\pi * AR_{wing}} \quad (63)$$

$$\alpha_{tail} = \frac{Cm_{wing}}{n_{tail} * VH * CL_{a_{tail}}} \quad (64)$$

$$i_t = a_{tail_0} + \varepsilon_0 \quad (65)$$

$$S_H = V_H * S * \frac{c}{l_t} \quad (66)$$

$$Lift_{tail} = 0.5 * ro * Vc^2 * S_H * CL_t \quad (67)$$

$$S_V = V_V * c * \frac{S}{lt} \quad (68)$$

$$S_{tail} = \frac{S_V + \frac{S_H}{2}}{0.9} \quad (69)$$

$$\theta_t = acos(\frac{S_H}{2S_{tail}}) \quad (70)$$

$$c_{tail} = \sqrt{\frac{S_{tail}}{2 * AR_{tail}}} \quad (71)$$

$$b_{tail} = c_{tail} * AR_{tail} \quad (72)$$

$$S_{tail} = \frac{S_H}{\left(cos(\theta_t)\right)^2} \quad (73)$$

$$X_{np} = X_{ac_w} + V_H * \frac{CL_{a_{tail}}}{CL_{a_{wing}}} * \left(1 - \frac{d\varepsilon}{d\alpha}\right) \quad (74)$$

$$SM = -\frac{dCm_{cg}}{d\alpha}\frac{1}{CL_{a_{wing}}} \quad (75)$$

$$Cm_{cg} = Cm_{ac_w} + CL_w * \left(X_{cg} - X_{ac_w}\right) - V_H CL_t \quad (76)$$

$$Cm_{cg} = Cm_{ac_w} + CL_{a_{wing}}(\alpha + i_w - \alpha_{w,0l}) * \left(X_{cg} - X_{ac_w}\right) - V_H CL_t \quad (77)$$

where

$\varepsilon - Downwash\ angle$

$\varepsilon_0 - Downwash\ angle\ at\ zero\ angle\ of\ attack$

$\frac{d\varepsilon}{d\alpha} - Change\ in\ downwash\ angle\ with\ angle\ of\ attack$

$CL_{wing} - Lift\ coeficient\ of\ the\ wing$

$CL_{0_{wing}} - Lift\ coeficient\ of\ the\ wing\ at\ zero\ angle\ of\ attack$

$CL_{a_{wing}} - Lift\ curve\ slope\ of\ the\ wing$

$CL_{tail} - Lift\ coeficient\ of\ the\ tail$

$CL_{0_{tail}} - Lift\ coeficient\ of\ the\ tail\ at\ zero\ angle\ of\ attack$

$CL_{a_{tail}} - Lift\ curve\ slope\ of\ the\ tail$

$Cm_{wing} - Moment\ coeficient\ of\ the\ wing$

$Cm_{0_{wing}} - Moment\ coeficient\ of\ the\ wing\ at\ zero\ angle\ of\ attack$

$\alpha\ - Angle\ of\ attck\ of\ the\ fuselage$

$\alpha_{tail}\ - Angle\ of\ attck\ of\ the\ tail$

$a_{tail_0}\ - Angle\ of\ attck\ of\ the\ tail\ for\ zero\ angle\ of\ attack\ in\ the\ fuselage$

$\alpha_{w,0l} - angle\ attack\ of\ the\ wing\ at\ zero\ lift$

$i_w - Wing\ incidence\ angle$

$i_t - tail\ incidence\ angle$

$S_H - Horizontal\ tail\ area$

$S_V - Vertical\ tail\ area$

$V_H - Horizontal\ volume\ ratio$

$V_V - Vertical\ volume\ ratio$

$c - Chord\ of\ the\ wing$

$S\ - Area\ of\ the\ wing$

$S_{tail}\ - Area\ of\ the\ tail\ (per\ tail)$

$l_t = x_{ac_{tail}} - x_{cg}$

$x_{ac_{tail}}$
$- distance\ from\ the\ leading\ edge\ of\ the\ wing\ to\ aerodynmic\ centre\ of\ the\ tail$

$x_{cg} - distance\ from\ the\ leading\ edge\ of\ the\ wing\ to\ centre\ gravity\ of\ the\ tail$

$x_{np} - distance\ from\ the\ leading\ edge\ of\ the\ wing\ to\ neutral\ point\ of\ the\ tail$

$\theta_t - dihedral\ angle\ of\ the\ tail$

$c_{tail} - chord\ of\ the\ V\ tail$

$b_{tail} - span\ of\ the\ V\ tail\ (root\ \ to\ tip)$

$X_{cg} = \frac{x_{cg}}{c}$

$X_{np} = \frac{x_{np}}{c}$

$SM - static\ margin$

Static stability criteria

$$Cm_{cg} = Cm_{ac_w} + CL_w * \left(X_{cg} - X_{ac_w}\right) - V_H CL_t > 0 \quad (78)$$

$$\frac{dCm_{cg}}{d\alpha} = CL_{a_{wing}} * \left(X_{cg} - X_{ac_w}\right) - V_H * CL_{a_{tail}} * \left(1 - \frac{d\varepsilon}{d\alpha}\right) < 0 \quad (79)$$

ADDENDIX B: Rest of the plots from the second aircraft surrogate model

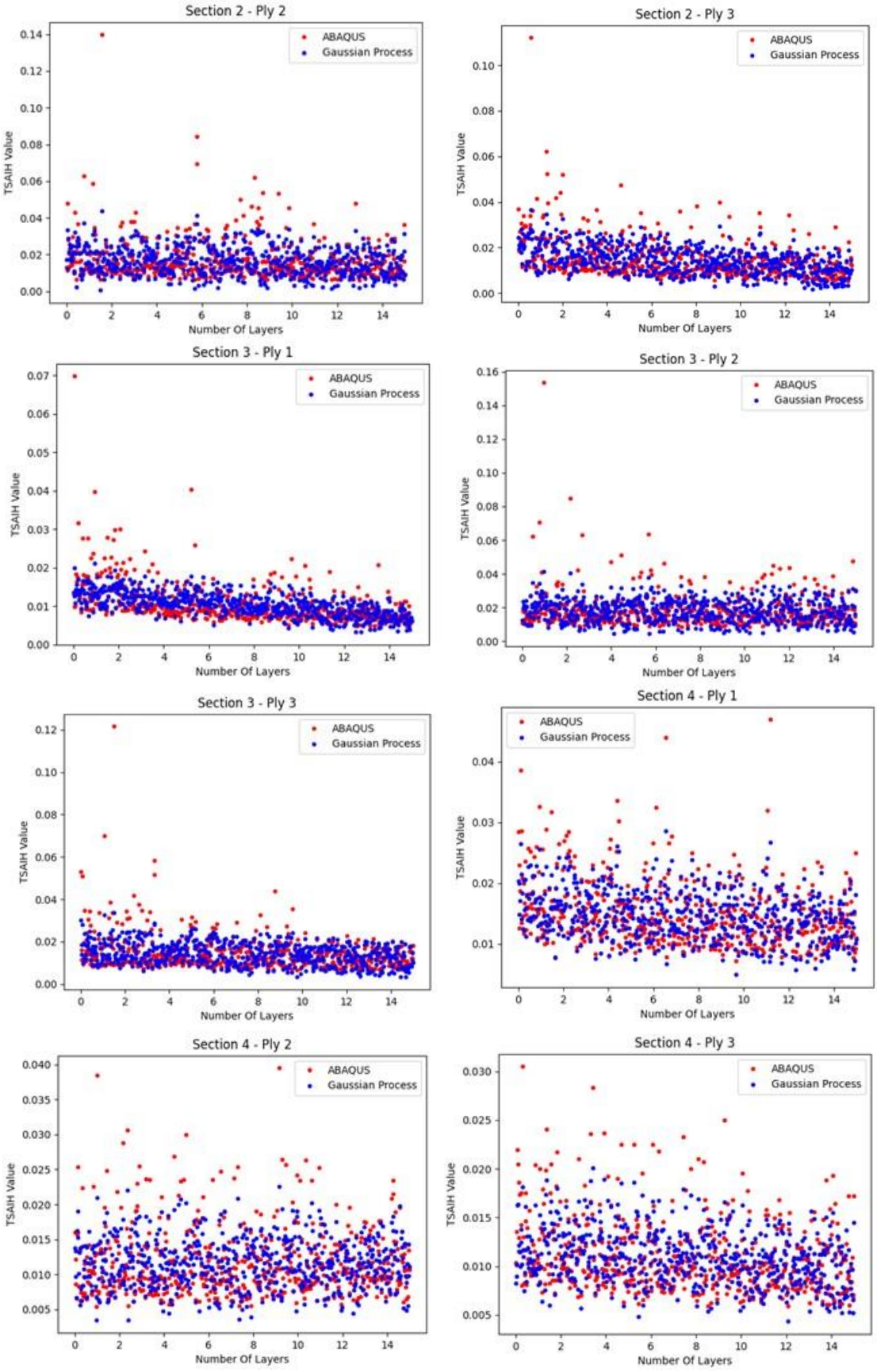

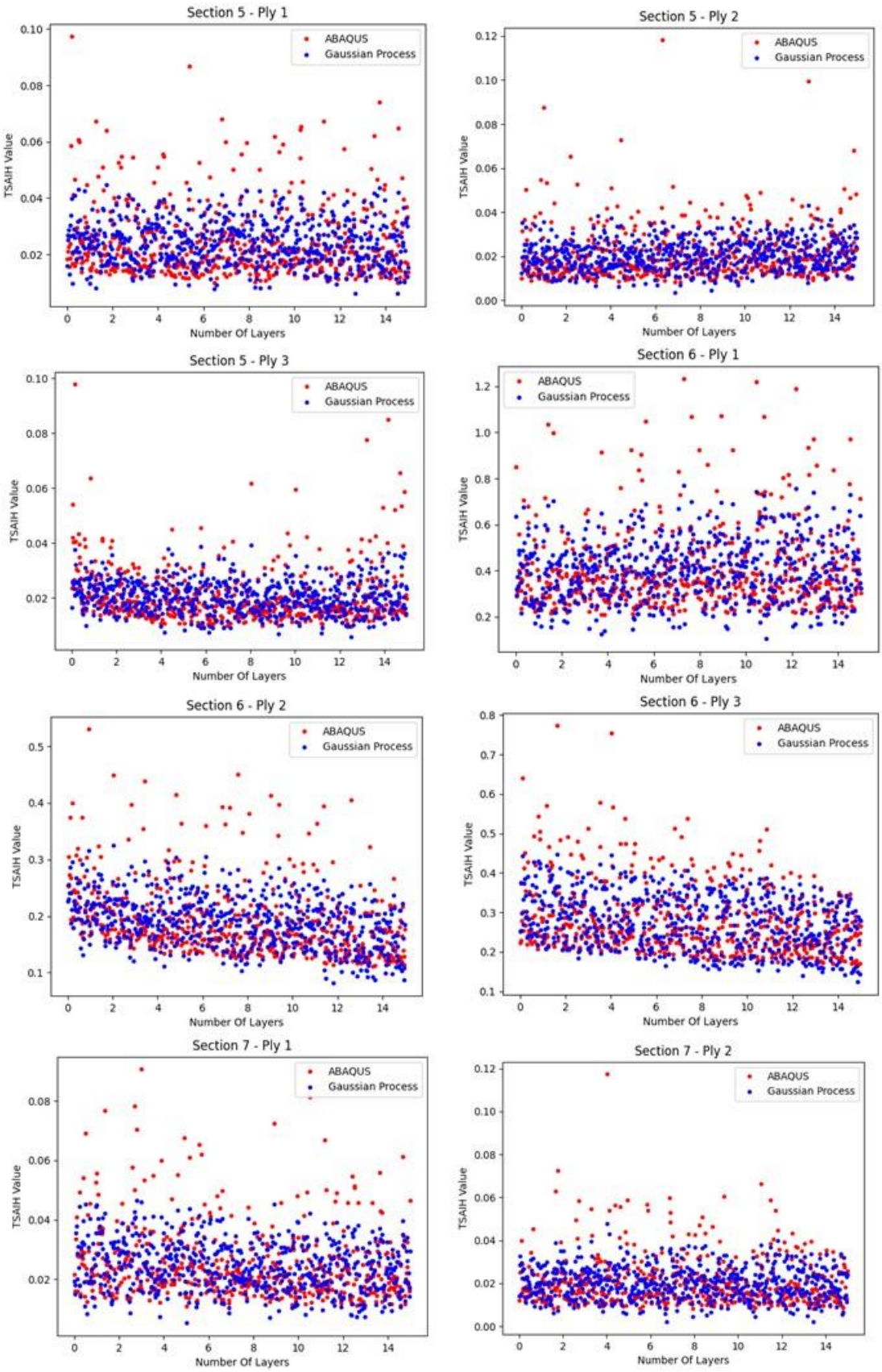
Section 5 - Ply 1
Section 5 - Ply 2
Section 5 - Ply 3
Section 6 - Ply 1
Section 6 - Ply 2
Section 6 - Ply 3
Section 7 - Ply 1
Section 7 - Ply 2
ABAQUS
Gaussian Process
TSAIH Value
Number Of Layers

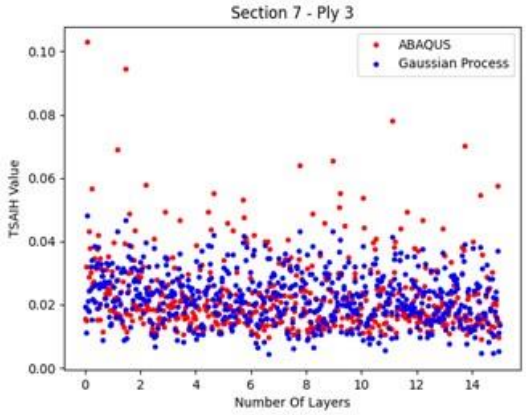
Section 7 - Ply 3
ABAQUS
Gaussian Process
TSAIH Value
Number Of Layers

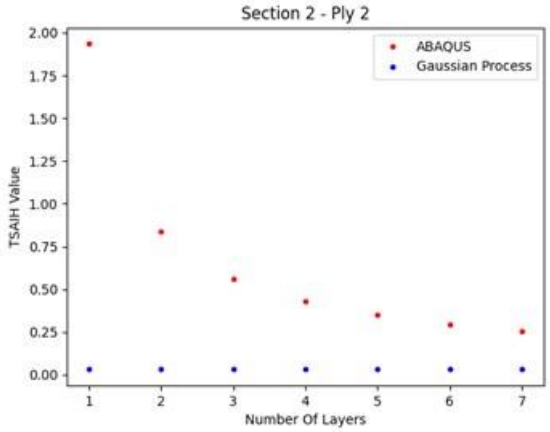
Section 2 - Ply 2
ABAQUS
Gaussian Process
TSAIH Value
Number Of Layers

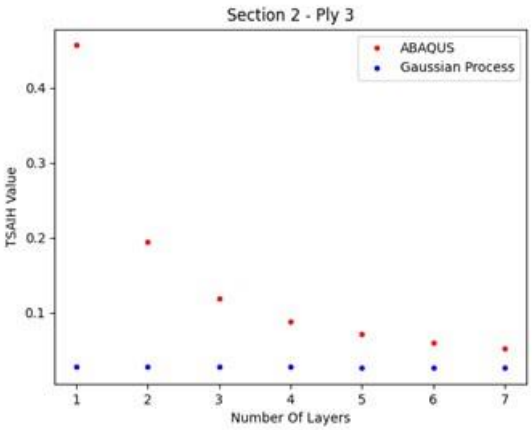
Section 2 - Ply 3
ABAQUS
Gaussian Process
TSAIH Value
Number Of Layers

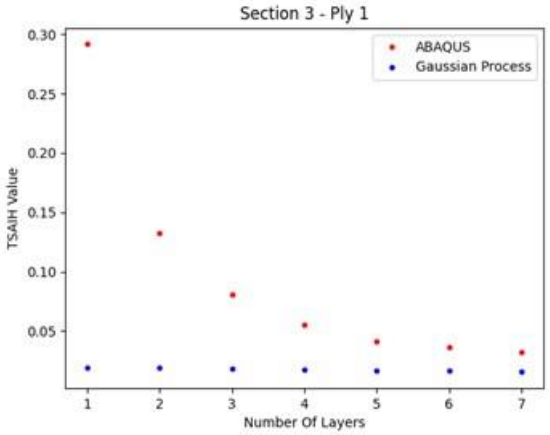
Section 3 - Ply 1
ABAQUS
Gaussian Process
TSAIH Value
Number Of Layers

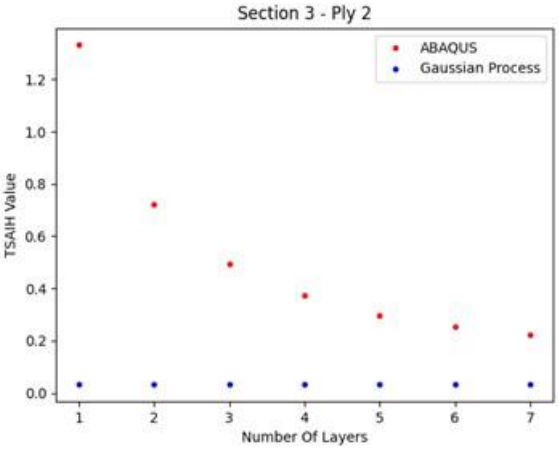
Section 3 - Ply 2
ABAQUS
Gaussian Process
TSAIH Value
Number Of Layers

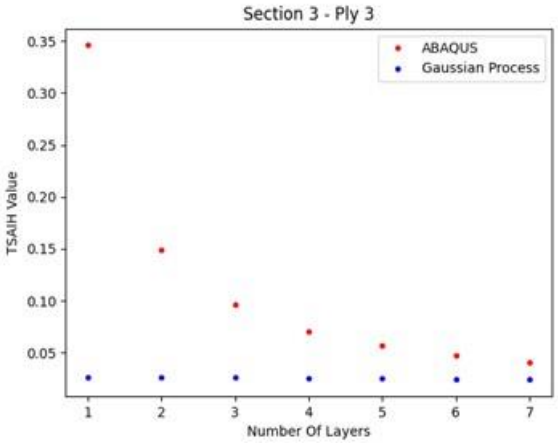
Section 3 - Ply 3
ABAQUS
Gaussian Process
TSAIH Value
Number Of Layers

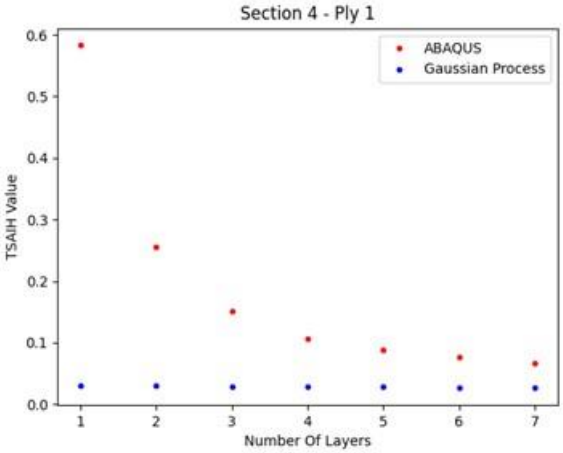
Section 4 - Ply 1
ABAQUS
Gaussian Process
TSAIH Value
Number Of Layers

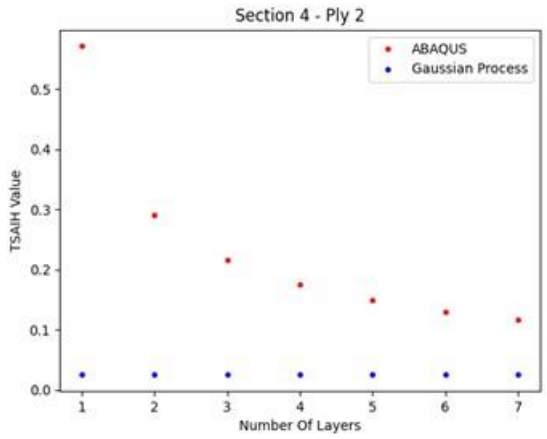
Section 4 - Ply 2
ABAQUS
Gaussian Process
TSAIH Value
Number Of Layers

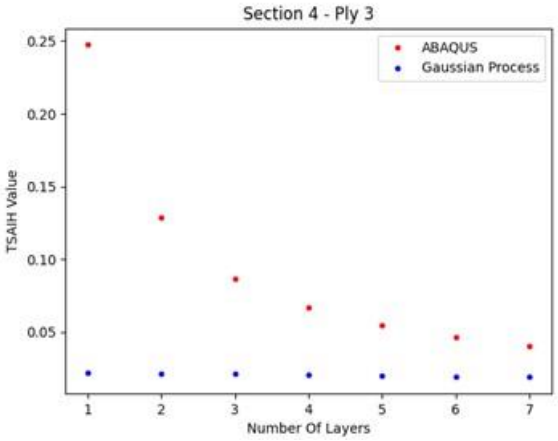
Section 4 - Ply 3
ABAQUS
Gaussian Process
TSAIH Value
Number Of Layers

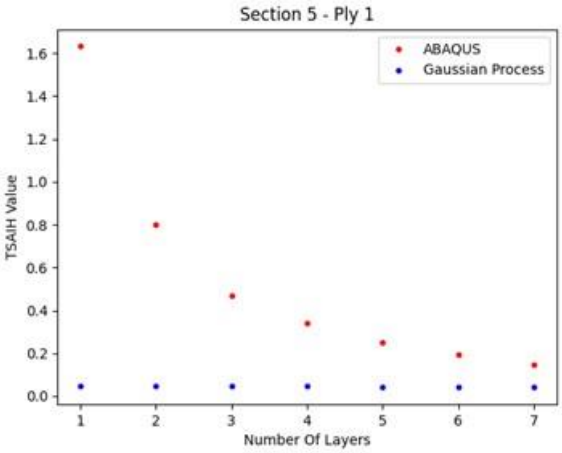
Section 5 - Ply 1
ABAQUS
Gaussian Process
TSAIH Value
Number Of Layers

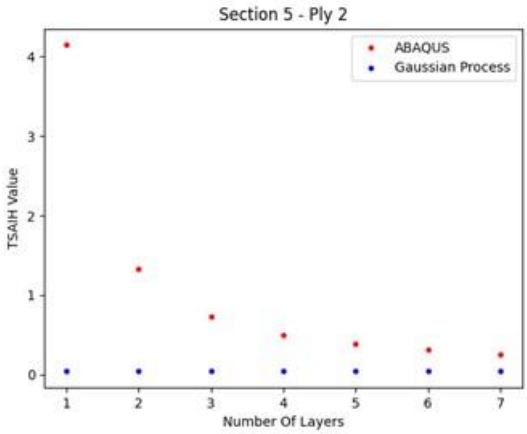
Section 5 - Ply 2
ABAQUS
Gaussian Process
TSAIH Value
Number Of Layers

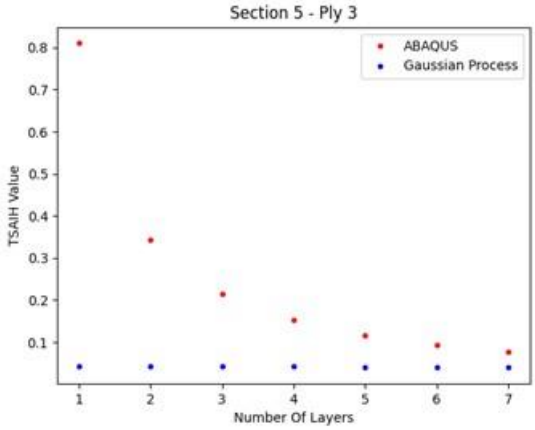
Section 5 - Ply 3
ABAQUS
Gaussian Process
TSAIH Value
Number Of Layers

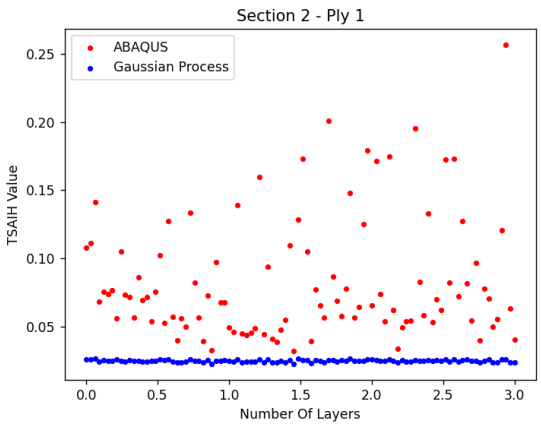
Section 2 - Ply 1
ABAQUS
Gaussian Process
TSAIH Value
Number Of Layers

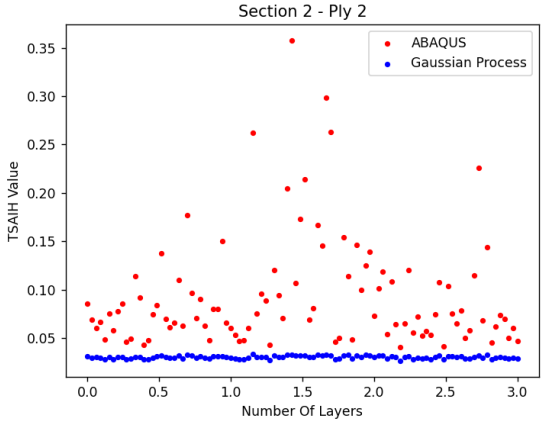
Section 2 - Ply 2
ABAQUS
Gaussian Process
TSAIH Value
Number Of Layers

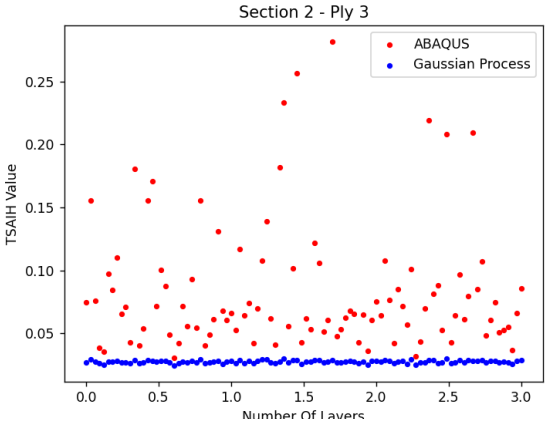
Section 2 - Ply 3
ABAQUS
Gaussian Process
TSAIH Value
Number Of Layers

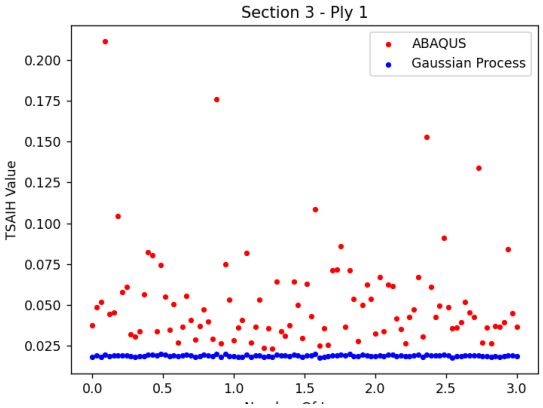
Section 3 - Ply 1
ABAQUS
Gaussian Process
TSAIH Value

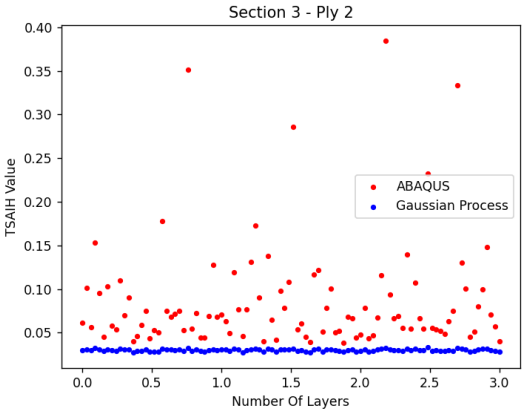
Section 3 - Ply 2
ABAQUS
Gaussian Process
TSAIH Value
Number Of Layers

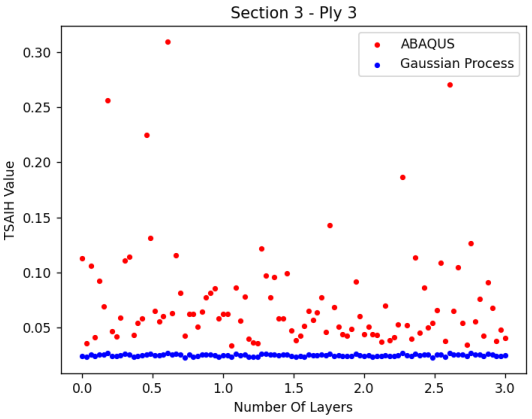
Section 3 - Ply 3
ABAQUS
Gaussian Process
TSAIH Value
Number Of Layers

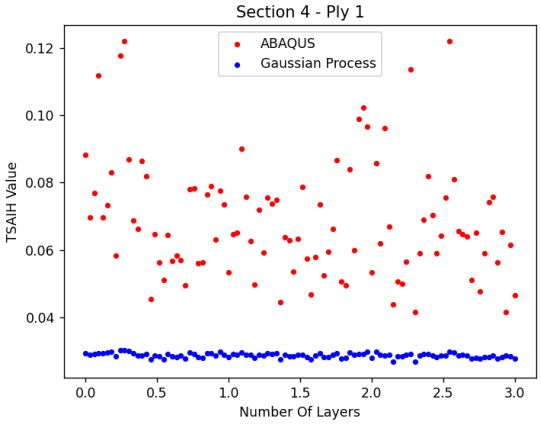
Section 4 - Ply 1
ABAQUS
Gaussian Process
TSAIH Value
Number Of Layers

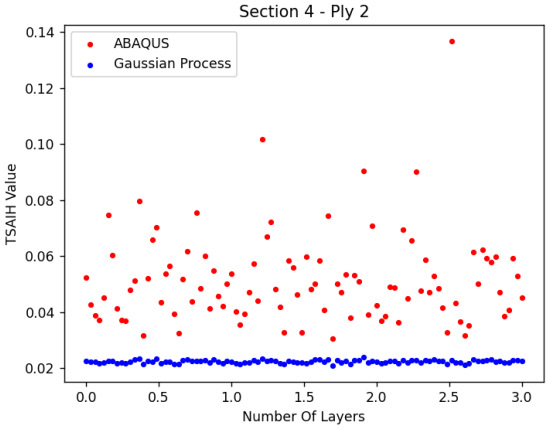
Section 4 - Ply 2
ABAQUS
Gaussian Process
TSAIH Value
Number Of Layers

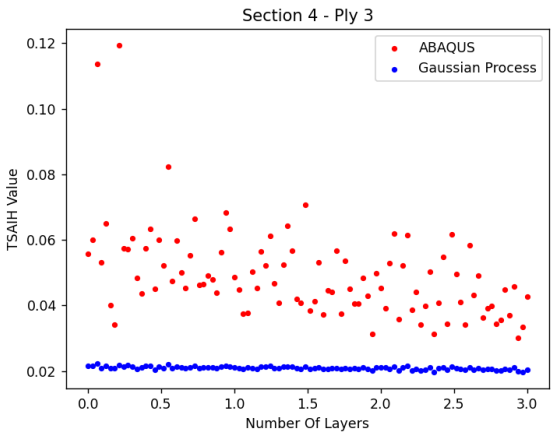
Section 4 - Ply 3
ABAQUS
Gaussian Process
TSAIH Value
Number Of Layers

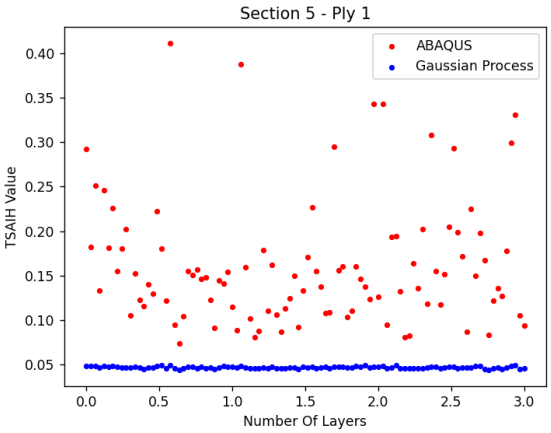
Section 5 - Ply 1
ABAQUS
Gaussian Process
TSAIH Value
Number Of Layers

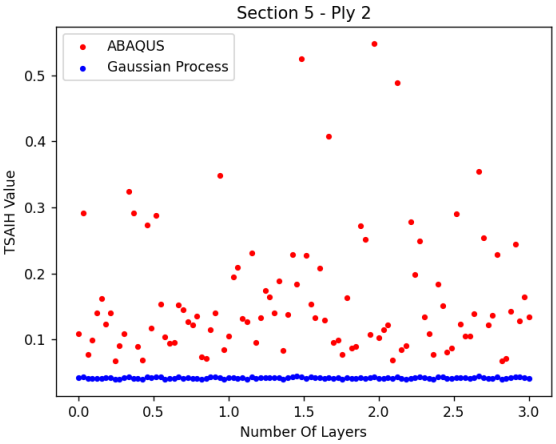
Section 5 - Ply 2
ABAQUS
Gaussian Process
TSAIH Value
Number Of Layers

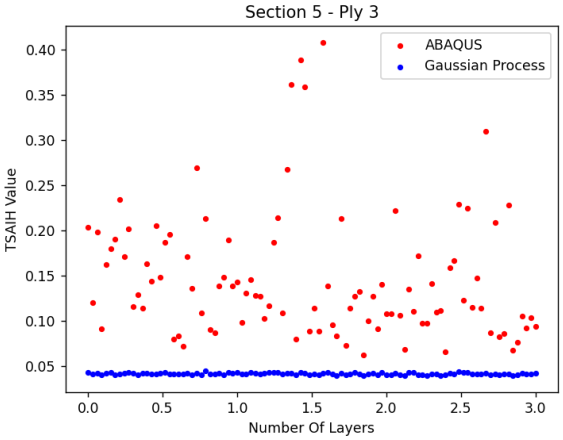
Section 5 - Ply 3
ABAQUS
Gaussian Process
TSAIH Value
Number Of Layers

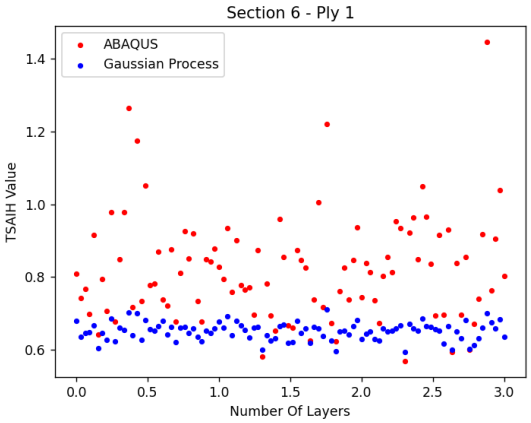
Section 6 - Ply 1
ABAQUS
Gaussian Process
TSAIH Value
Number Of Layers

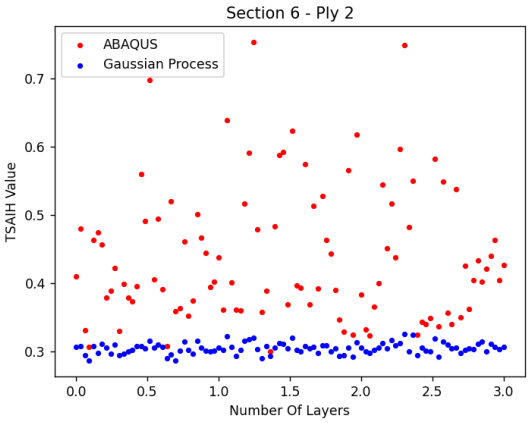
Section 6 - Ply 2
ABAQUS
Gaussian Process
TSAIH Value
Number Of Layers

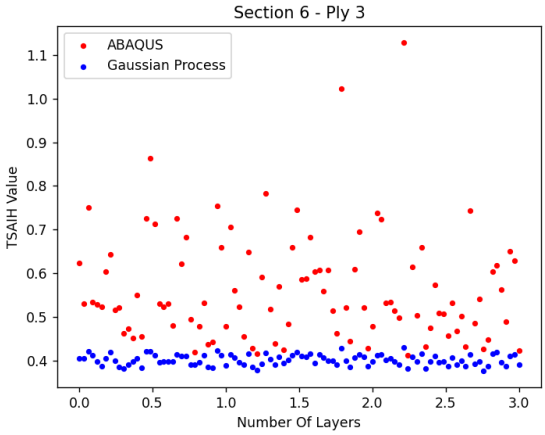
Section 6 - Ply 3
ABAQUS
Gaussian Process
TSAIH Value
Number Of Layers

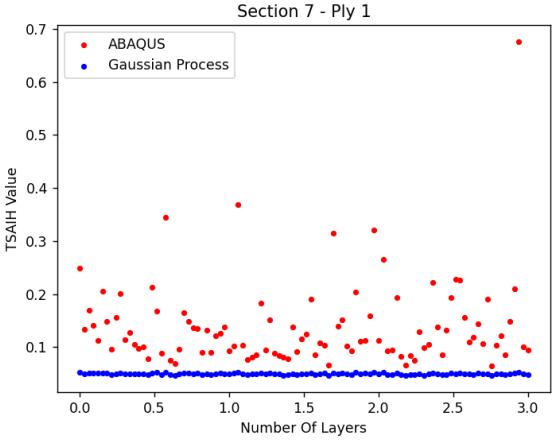
Section 7 - Ply 1
ABAQUS
Gaussian Process
TSAIH Value
Number Of Layers

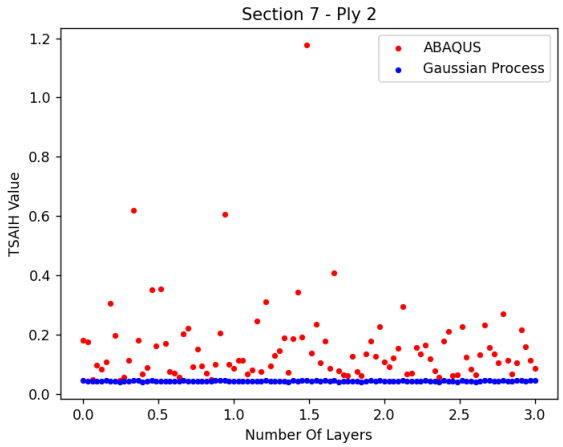
Section 7 - Ply 2
ABAQUS
Gaussian Process
TSAIH Value
Number Of Layers

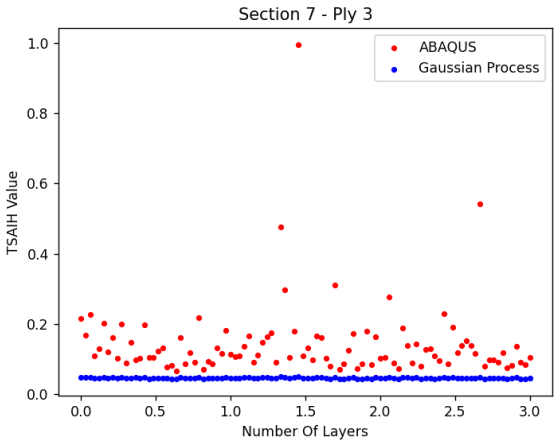
Section 7 - Ply 3
ABAQUS
Gaussian Process
TSAIH Value
Number Of Layers